Characterizations of RC Beams Intervened by ICCP-SS System with Externally Bonded Carbon-FRCM Composites

炭素 FRCM 複合材の外部接着により ICCP-SS 工法を施した RC はりの特性評価

By

WEI Liangliang

A thesis submitted in partial fulfillment of the requirements for the degree of Doctor of Philosophy in Engineering

(Supervisor)
Associate Professor Koji MATSUMOTO
(Co-supervisor)
Professor Tamon UEDA
Professor Ji-Hua ZHU
Professor Takashi MATSUMOTO
Professor Hiroshi YOKOTA

English Engineering Program (e3)
Laboratory of Engineering for Maintenance System
Division of Engineering and Policy for Sustainable Environment
Graduate School of Engineering
Hokkaido University
Sapporo, Japan
June 2020

ACKNOWLEDGEMENTS

First and foremost, I would like to express my deepest gratitude to my supervisors, one with Prof. Tamon UEDA who has accepted me to be his student and encouraged me throughout my studies, who has my respect, admiration and infinite gratitude for his guidance, patience and continuous support and one with Prof. Ji-Hua ZHU who has provided me with valuable instructions in my doctoral study and supported me in Japan for Ph.D. study, who also has my respect, admiration and infinite gratitude for his guidance, patience and for always lifting my spirit. Without their kindhearted supervision and empathetic attitude, this research would be unable to be completed.

I am also extremely and sincerely thankful for the valuable guidance and comments provided by my doctoral committee members, Koji MATSUMOTO sensei, Prof. Takashi MATSUMOTO, and Prof. Hiroshi YOKOTA. Your contribution is much appreciated.

My sincere thanks also extend to Dr. Werawan Manakul, who always gives me encouragement and support, and to Dr. Meini SU for her kind support to my research progress. I also wish to extend my thanks to Guangdong Province Key Laboratory of Durability for Marine Civil Engineering at Shenzhen University, and it has supported me to fulfill such an extensive experimental work.

I especially thank my research group mates Zhao WANG and Miaochang ZHU for their valuable companionship and encouragement during my study and my dear friends at Hokkaido University who helped me a lot during my Ph.D. study in Japan, as well as dear friends at Shenzhen University who always supported and encouraged me. The friendship between us is a wonderful memory in my life, which I will always cherish.

Funding from the National Natural Science Foundation of China (51538007, 51778370), Natural Science Foundation of Guangdong (2017B030311004), and Shenzhen science and technology project (JCYJ20170818094820689) are gratefully acknowledged.

Finally, I would like to express my deepest love and gratitude to my parents and my beloved wife. The encouragement, patience, support, and unconditional love by all of you made me through the hard time.

ABSTRACT

The development of alternative techniques for structural rehabilitation is of critical importance to the safety and sustainability of concrete structures suffered from corrosion of steel. The structural strengthening (SS) and impressed current cathodic protection (ICCP) are conventional methods to improve the safety and sustainability of corroded concrete structures at different perspectives. The SS can recover the load-carrying capacity of deteriorated concrete structures, while the ICCP can retard the corrosion of steel in concrete. Currently, a new strategy to integrate ICCP with SS has been proposed that is termed as ICCP-SS intervention system. Fabric reinforced cementitious matrix (FRCM) composites have emerged as an alternative reinforcement material to fiber reinforced polymer (FRP) composites for structural strengthening and rehabilitation. The carbon-FRCM composite can be adopted as the dual-functional material in the ICCP-SS system in which carbon-FRCM plays the role of reinforcement material in the SS system and of anode material in the ICCP system. To this end, an experimental program was undertaken to propel the application and optimization of the ICCP-SS intervention system.

This study aims to clarify the characterization of RC beams with externally bonded carbon-FRCM under static and cyclic loading. Two carbon-FRCM composites were considered for this research, one with multilayer carbon-FRCM (M/C-FRCM) intended for understanding the effectiveness of carbon-FRCM in strengthening beams and one with anodically polarized carbon-FRCM (AP/C-FRCM) for evaluating the mechanical degradation caused by anodic polarization in the ICCP on the strengthening characterization of RC beams. From the material perspective, the mechanical properties of both M/C-FRCM and AP/C-FRCM composites were also studied.

The first study investigates the static performance of RC beams with externally bonded M/C-FRCM. The static tensile tests of M/C-FRCM were conducted, followed by the four-point bending tests of beams with externally bonded M/C-FRCM under static loading. Nine M/C-FRCM specimens were prepared for tensile tests, and four beams were prepared for bending tests. The prediction model of apparent strain of carbon fabric (CF) mesh in the M/C-FRCM was proposed based on the global strain of carbon-FRCM in tension. The load-carrying capacity of beams with externally bonded M/C-FRCM improved that was largely dependent on the amount of CF mesh. An analytical study on the prediction formulas in flexure for RC beams with externally bonded carbon-FRCM was performed by using the model of apparent strain of CF mesh. Prediction results agreed well with the experimental results.

The second study explores the fatigue performance of RC beams with externally bonded M/C-FRCM. The cyclic tensile tests of M/C-FRCM were performed and followed by the four-point bending tests of beams with externally bonded M/C-FRCM under cyclic loading. Nine M/C-FRCM specimens were prepared for cyclic tensile tests, and twelve beams were prepared for cyclic bending tests. The fatigue life model and the fatigue strength model of M/C-FRCM composites were proposed. The fatigue life performance of carbon-FRCM was compared with steels and CFRP composite materials. Besides, the fatigue stress limit of M/C-FRCM was recommended to be 35% of the ultimate tensile strength. Carbon-FRCM composites significantly improved the fatigue performance of RC beams comparing with un-strengthened beams. The S-N curve for beams with externally bonded M/C-FRCM was proposed.

The third study examines the influence of anodic polarization on the static performance of RC

beams with externally bonded AP/C-FRCM. An accelerated electrochemical (AC-EC) test was performed to introduce the anodic polarization to the carbon-FRCM making the AP/C-FRCM. Then, the static tensile tests of AP/C-FRCM were conducted and followed by the four-point bending tests of beams with externally bonded AP/C-FRCM under static loading. The tensile strength of carbon-FRCM reduced after suffering from anodic polarization. Effectiveness of carbon-FRCM suffering from anodic polarization in strengthening did not change before the yielding of steel and weaken slightly as increasing the intensity of anodic polarization.

The last study detects the influence of anodic polarization on the fatigue performance of RC beams with externally bonded AP/C-FRCM. The identical AP/C-FRCM composites were adopted in this study. The cyclic tensile tests of AP/C-FRCM were performed and followed by the four-point bending tests of beams with externally bonded AP/C-FRCM under cyclic loading. The combined damage effect of the anodic polarization and cyclic loading caused an acceleration of reduction of stiffness and decrease of fatigue life of carbon-FRCM. Based on the total experimental data, the S-N curve for beams with externally bonded fabric reinforcement by inorganic matrix was proposed.

Overall, the constitutive behavior of both M/C-FRCM and AP/C-FRCM were assessed by static tensile tests, and the fatigue degradation characterizations of both carbon-FRCM were evaluated through cyclic tensile tests. The fatigue life prediction models of M/C-FRCM and AP/C-FRCM were proposed based on the experimental data. The strengthening behaviors of RC beams with externally bonded M/C-FRCM and AP/C-FRCM were investigated under static and cyclic loading. The prediction formulas in flexure for RC beams with externally bonded carbon-FRCM was proposed. Besides, the fatigue life of strengthened beams was predicted well based on the proposed S-N curve. However, in future studies, the further optimization design of carbon-FRCM is necessary to improve the mechanical behavior of itself and bond behavior with concrete substrate. Moreover, the fatigue performance of the bond between carbon-FRCM and concrete needs to be investigated to improve the fatigue life prediction of RC beams with externally bonded carbon-FRCM composites.

Keywords: FRCM, ICCP, beam, static, fatigue, anodic polarization, S-N

TABLE OF CONTENTS

CHAPTER 1

INTRODUCTION

1.1 Background

Nowadays, deterioration of reinforced concrete (RC) structures is the widespread durability issue. The corrosion of steel reinforcements in concrete is recognized as the most severe factor leading to the deterioration of RC, followed by the frost damage in the cold region and physical-chemical impact in the corrosive environment (Mehta, 1991). The corrosion of steel reinforcements results in the decrease of load-carrying capacity and reduction of the service life of RC structures. To improve the durability of RC structures suffered from the corrosion of steels, the following two kinds of intervention methods are commonly adopted.

Starting to solve the problem of corrosion of steels in concrete, impressed current cathodic protection (ICCP) has been proven to be an efficient method to control the rate of corrosion of steels (Weyers et al., 1993). Fig. 1.1 shows a typically schematic ICCP installation in concrete. The auxiliary anode material is bonded to the surface of RC structures, and then the anode material is connected to the positive terminal of an external power supply source; meanwhile, the corroded steels in concrete are connected to the negative terminal of that. A specific protection current from the power supply is applied to concrete to make the corroded steels towards the immune zone so that the rate of corrosion of steels decreases to a negligible level. ICCP had successfully protected some concrete structures for several years, such as the Sydney Opera House (Tettamanti, 1997) and Yaquina Bay Bridge in Newport, Oregon (Cramer et al., 2002), etc. The standard practices and criteria have been published by NACE International Institute (NACE SP0290, 2007; Barlo, 2001).

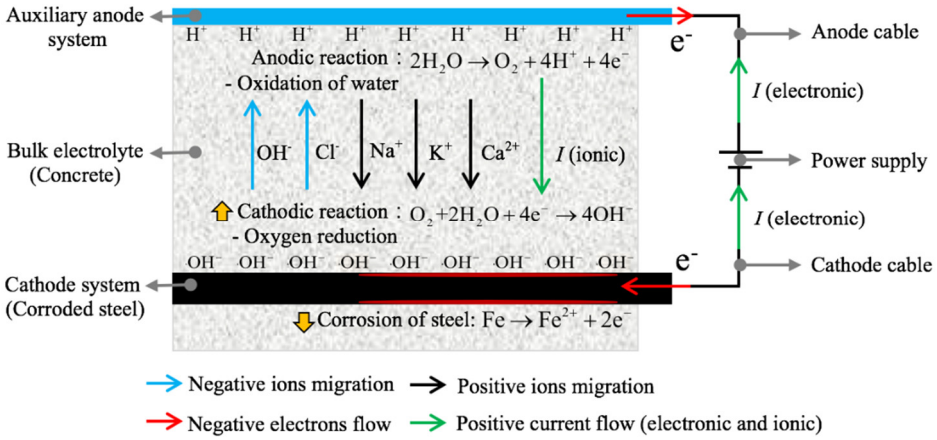

Fig. 1.1 A typically schematic ICCP installation in concrete.

The other intervention method is to adopt structural strengthening to increase the load-carrying capacity of deteriorated RC structures caused by the corrosion of steels. Currently, fiber reinforced polymer (FRP) strengthening has been proven to be a successful method to repair deteriorated concrete structures. Fig. 1.2 shows a typical practice of FRP strengthening on a concrete bridge. FRP reinforcement is externally bonded to the surface of the concrete. A great number of researches on the FRP strengthening have been conducted after the Second World War (El-Mihilmy et al.,

2000). The guide for the design and construction of externally bonded FRP systems for strengthening concrete structures has been published in China (GB 50367, 2013), United States (ACI 440.2R, 2008), Japan (JSCE, 2001), European region (CEB-FIP, fib bulletin 14, 2001), etc.

Fig. 1.2 Strengthening of a concrete bridge with CFRP sheet (Sonnenschein et al., 2016).

However, we must notice the insufficient issues on each separate method. The helplessness of ICCP is that the reduction of the load-carrying capacity of structures caused by pre-existing corrosion of steels cannot be improved even though the corrosion of steels stops after applying ICCP. The pre-existing corrosion of steels results in the loss of effective cross-section area of steels and degradation of bond strength between steels and concrete. These problems cannot be solved by using ICCP. It is possible that the deteriorated structures intervened by ICCP still do not satisfy the requirement of structural safety design. Compared with ICCP, the point of structural strengthening is that the inherent corrosion of steels in concrete weakens the strengthened structures continuously even though the load-carrying capacity can be instantly increased after applying structural strengthening.

Therefore, considering both the benefits and insufficiencies of either ICCP or structural strengthening, the idea of a combination of both ICCP and structural strengthening (SS) is proposed by Prof. Zhu at Shenzhen University, China. The same construction technology of ICCP and SS system is to bond anode materials or reinforcement materials on the surface of concrete structures. It is potential to integrate ICCP and SS when a dual-functional material can be used to act as anode material in ICCP and as strengthening reinforcement material in SS. Accordingly, the concept of the ICCP-SS intervention system has been proposed to improve the durability of RC structures suffered from the corrosion of steels. Fig. 1.3 shows a schematic diagram of the RC beam intervened by the ICCP-SS system. The unique reinforcement material is externally bonded to the concrete structure, which is a conventional strengthened RC beam. Simultaneously, the bonded reinforcement material is used as anode material to develop a traditional ICCP system on the strengthened beam by using an external power supply. Therefore, the steel reinforcements in the corroded RC beam can be protected, and the load-carrying capacity can be increased at the same time when the implementation of the ICCP-SS intervention system satisfies the construction and installation requirements of both ICCP and structural strengthening. Moreover, the ICCP-SS system should also be hopeful to promote the development of seawater sea sand concrete whose purpose is not only to save the freshwater resource but also to solve the urgent resource shortage of river sand in construction engineering.

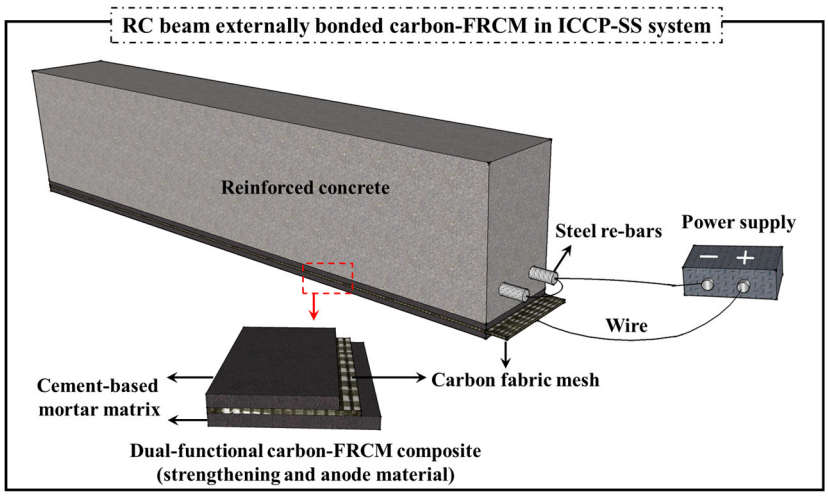

Fig. 1.3 A schematic diagram of the RC beam intervened by the ICCP-SS system.

Due to the proposal of ICCP-SS is a new concept, for a preliminary understanding, the following sections present some researches of the ICCP-SS system from the material structure level to the structural members level.

Evaluation of CFRP as the dual-functional material

The effectiveness of ICCP greatly depends on the selection of the anode that needs to consider the electrical conductivity for the electrochemical process and the rate of consumption due to several environmental and operational factors. The anode system is required to deliver sufficient current to provide adequate protection for corroded steels in concrete. Therefore, selecting the right anode material and applying an appropriate value of protection current contribute significantly to the avoidance or minimization of damage to the anode, such as either excessive consumption or loss of bond with the concrete.

In comparison to the pricy coated titanium mesh or ribbon anode system, the carbon fiber reinforced polymer (CFRP) is found to be a promising anode material due to the electrically conductive property of carbon fiber (Mork et al., 2006; Lee-Orantes et al., 2007; Mahdi, 2010; Gadve et al., 2010, 2011; Van Nguyen et al., 2012; Zhu et al., 2014a, 2014b; Lambert et al., 2015; Zhang et al., 2016, 2019). Besides, CFRP is a common reinforcement material in FRP strengthening. It has the characteristics of high strength-low weight and excellent durability in the long-term period. Research on applications of CFRP in structures has been summarized by international specifications (BS EN 1504-10, 2017). Therefore, in the proposed ICCP-SS system by using the dual-functional CFRP material, the anodic and mechanical behavior of CFRP should be investigated, and the theoretical operating period of CFRP as a dual-functional material should be evaluated.

The accelerated testing method is adopted to investigate the long-term performance of CFRP as an anode and the evaluation of mechanical properties. According to (NACE SP0294, 2016), the accelerated electrochemical (AC-EC) test of anodes for use in concrete should be conducted in an aqueous solution including NaCl solution, NaOH solution, and simulated pore solution. The performance of CFRP anode was investigated in the simulated ICCP system with the electrolyte of 3% NaCl solution (Sun et al., 2016), NaOH solution (Zhu et al., 2016a) and simulated pore solution (Zhu et al., 2016b). On the one hand, the CFRP operated stably in all three solutions, and the electrochemical performance was not significantly compromised during 50 days of polarization

when the applied current density was up to 6.15 A/m^2. On the other hand, the results of tensile tests of CFRP after polarization indicated that the tensile strength of CFRP decreased with the accumulated charge densities increase in the simulated ICCP system. The residual tensile strength of CFRP reduced to 71.1% (in the case of 3% NaCl solution), 40.1% (in the case of NaOH solution), 48.3% (in the case of simulated pore solution) of the referenced CFRP when CFRP was suffering to anodic polarization at the charge density of 3610 A-h/m^2. Theoretically, the amount of accumulated charge density that the CFRP was subjected to is equivalent to 40 years of the operating period if the ICCP system is operated at a current density of 10 mA/m^2 of anode surface area.

Furthermore, it seems that the chloride environment was helpful in developing the dual-functional characteristics of CFRP material via the comparison of the residual tensile strength of CFRP suffered from polarization in different solution environments (Sun et al., 2016; Zhu et al., 2016a, 2016b). Zhu et al. (2017) investigated the mechanical behavior of CFRP in the simulated ocean water containing different concentrations of chloride. Results showed that the tensile strength of CFRP after anodic polarization decreased with increasing charge densities, and, for a given charge density, it increased with increasing concentration of chloride. It was found that oxygen evolution occurring at the lower concentration of chloride primarily damaged the carbon fiber reinforcement, while chlorine evolution occurring at higher concentration mainly damaged the epoxy resin matrix. The mechanical degradation mechanism of CFRP as an anode in the chloride environment was attributed to the breakage of C-N bonds (Sun et al., 2016).

It concludes that the dual-functional CFRP material can not only deliver sufficient current continuously but also maintain an adequate tensile strength after a relative longer operating period. The CFRP material is an excellent option to develop an ICCP-SS intervention system. However, except for the investigation on the mechanical behavior of CFRP, the interfacial behavior of the dual-functional material on the concrete is also a critical issue.

Interfacial behavior of the dual-functional composite material

Generally, the CFRP is bonded by polymeric adhesive for strengthening concrete, in which the epoxy resin is commonly used. However, it fails to pass the protection current through the anode system to corroded steels when the CFRP is bonded to concrete using epoxy resin because the combination of CFRP and epoxy resin is not sufficiently conductive (Van Nguyen et al., 2012). Therefore, the alternatives are considered such as adding carbon powder, particulates or fillers, and chopped carbon fiber to the epoxy to increase electrical conductivity (Lee-Orantes et al., 2007; Gadve et al., 2010, 2011) or using inorganic bonding material like the modified cement-based paste (Zhu et al., 2014a, 2019; Zhang et al., 2018; Su et al., 2019a, 2019b, 2020) or mortar matrix (Wei et al., 2019).

However, although the use of organic epoxy resin-based adhesive is commonly employed by engineers in CFRP strengthening, and the issue of electrical conductivity can be addressed by adding some additives, a great number of studies have identified the disadvantages of epoxy resin such as the poor performance above the glass transition temperature of the polymer resin, the poor fire resistance, inability to apply FRP on wet surfaces or at low temperatures, lack of vapor permeability, which may cause damage to the interface, etc. Van Nguyen et al. (2012) observed the generation of yellow liquid and gaseous deposits at the concrete-fabric interface when the CFRP sheet was bonded to the concrete, and the ICCP was operated. Moreover, the anodic interface in the ICCP system is a

place to allow the electrochemical process that is an exchange and transformation between electrons (i.e., e^-) and chemical ions (i.e., OH^-, Cl^-) as shown in Fig. 1.1. The electrons path is in the anode material, cathode material, and conductive wires, while the path of the ions is in the concrete electrolyte. Therefore, the real anode material is the electrically conductive additives added in the epoxy resin, which is a small amount of thin layer nearby the surface of the concrete. It will fail to pass the protection current through the anode system once the small amount of thin layer conductive additives anode is consumed during ICCP exposure time. It means that the conductive epoxy resin-based CFRP is not very suitable to act as the dual-functional material in the ICCP-SS intervention system considering the concept of ICCP-SS and the drawbacks of organic epoxy resin.

Almost a decade ago, the cementitious matrix was introduced in the field of structural strengthening (Triantafillou et al., 2006) as an alternative to FRP-epoxy resin, addressing cost and durability issues. Since then, the cementitious matrix progressively attracts the interest of the structural engineering community. Comparing with the available epoxy resin in the market, the cementitious matrix has its advantageous characteristics such as good electric conductivity, better durability, ease of installation, better fire resistance, and ease of reversibility (that is, the ability to undo the repair without harming the original structure). Besides, both the cementitious matrix and concrete are inorganic material. It has compatibility with the chemical, physical, and mechanical properties of the concrete substrate. Development of high-performance cementitious matrix has attracted great research interests recently, and the investigations include the new material proposal, property characterization, and application on structural strengthening, etc. (Awani et al. 2017; Escrig et al. 2017). Besides, several international design standards for the use of cementitious matrix are also available (JSCE, 2008; ACI 549.4R, 2013; AC434, 2016; RILEM, 2016). By embedding the carbon fabric mesh inside of the cementitious matrix, a carbon fabric reinforced cementitious matrix (carbon-FRCM) composite material is produced (ACI 549.4R, 2013; D'Ambrisi et al. 2013, 2015).

Su et al. (2019a) investigated the effects of different types and amounts of high molecular weight polymer and short-chopped carbon fibers on the flexural and compressive strength, conductivity, and shear strength of a cement-based paste with concrete substrate. A high-performance cementitious matrix was proposed for the development of strengthening using carbon-FRCM. And then a variety of impressed current densities from 20 to 400 mA/m^2 was adopted in the steel reinforced concrete bulk with externally bonded the carbon-FRCM that was used as the dual-functional composite material. It was found that the ICCP system using carbon-FRCM could provide effective cathodic protection to steels in concrete. Based on the single shear test results, the shear strength degraded with increasing charge densities due to anodic polarization. In the case of severe polarization, the occurrence of anodic acidification led to the change of failure mode in the carbon-FRCM/concrete interface from debonding within the concrete to the debonding at the interface between carbon fabric and cementitious matrix. The shear strength decreased by around 12%. It concluded that it was feasible to use carbon-FRCM composite material as a dual-functional material for the development of the ICCP-SS intervention system.

However, the applied current density should be chosen carefully according to the cathodic protection codes, as overlarge current density possibly results in deterioration of interfacial behavior between carbon fabric mesh and cementitious matrix. Zhang et al. (2018) focused on the changes at the paste-carbon fiber anode interface by applying current. It was found that a white zone was formed around the anode, which was due to the calcium dissolution caused by electrochemical

reaction at the carbon fiber anode. This kind of degradation of the interfacial behavior of the dual-functional composite material increased resistivity of the ICCP system that might eventually make the ICCP-SS intervention system fail because of insufficient current densities and weakness of bond behavior.

The further degradation mechanism of the dual-functional carbon-FRCM composite material suffered from the anodic polarization in ICCP is ongoing research. Besides, the optimal application of the ICCP-SS intervention system by using carbon-FRCM needs to be more investigation considering the efficiency of passing the current and sufficiency of the bond strength for strengthening. Furthermore, it is necessary to verify the effectiveness of the ICCP-SS intervention system on the concrete members.

Structural behavior of concrete members intervened by ICCP-SS system

The unique advantage of the ICCP-SS intervention system is using a dual-functional composite material for protecting the corroded steels in concrete and strengthening deteriorated concrete structures, no other external anodes and reinforcement materials are necessary that contributes to the reduction of the cost of rehabilitation and maintenance. Gadve et al. (2010) compared the performance of three beams suffered from the corrosion in which one was a control beam, one was a beam strengthened with CFRP (beam CPP), and the other was a CFRP-strengthened beam with ICCP treatment using CFRP as an anode (beam CAP). The results of the detection of steels in concrete indicated that the mass loss of steels reduced from 7.5% in the control beam to 6.1% in beam CPP, and dropped to 1.1% in beam CAP. The corrosion of steels in beam CAP decreased significantly due to the ICCP intervention using CFRP. The flexural test results showed that the ultimate load of beam CPP and CAP increased by 78% and 88% to the control beam. They concluded that the active and passive protection for the corroded beams had been successfully achieved using electrically conductive CFRP as an anode and strengthening reinforcement. A similar investigation was also conducted by Lambert et al. (2015). However, as discussed before, the conductive epoxy resin-based CFRP anode is not very suitable to act as the dual-functional material in the ICCP-SS intervention system.

Zhu et al. (2018) investigated the compressive behavior of corroded RC columns intervened by the ICCP-SS system using the dual-functional carbon-FRCM composite material. The corroded steels in RC columns were protected successfully. Compared with the referenced corroded RC column, the ultimate compressive load of columns strengthened alone with carbon-FRCM increased by 28.9%. In comparison, the ultimate load of columns intervened by the ICCP-SS system increased between 22.6% and 50.4% that depended on the value of applied current densities in ICCP. Besides the compressive concrete columns, the RC beams were also tested in flexure. Su et al. (2019b) bonded the carbon-FRCM to the soffit of the simply support beams. The ultimate load of beams only protected by ICCP and beams only strengthened with carbon-FRCM composite increased by 7.5% and 15.8% to the referenced corroded RC beams, respectively. While the ultimate load of ICCP-SS intervened beams increased by from 19.2% to 41.8% since different protection current densities were applied in ICCP. It concluded that the ICCP-SS intervention system was superior compared to the conventional ICCP and SS by oneself, which could not only prevent the further corrosion of steels but also improve the load-carrying capacity of degraded beams. A similar investigation was also conducted by Zhu et al. (2019) and Su et al. (2020), which investigated the flexural behavior of the continuous beams.

However, all the above-mentioned researches are conducted under static loading; the mechanical behavior of RC beams intervened by the ICCP-SS system using the dual-functional carbon-FRCM composite material under cyclic loading is also necessary. Moreover, they all documented that the appropriateness of the design codes for predicting the long-term performance of the ICCP-SS system on the RC beams need further investigation. Besides, during the service life of infrastructures such as bridges, vehicular traffic imposes cycles of loading and unloading on the structures that probably lead to fatigue failure. The ICCP-SS intervention system is a promising measure to improve the fatigue behavior of RC beam suffered from corrosion of steels. The relevant studies on the fatigue behavior of RC beams intervened by the ICCP-SS system have still yet carried out. Thus, the characterizations of RC beams with externally bonded carbon-FRCM are essential for further understanding.

1.2 Literature review

1.2.1 Characterizations of FRCM composites

Fabric reinforced cementitious matrix (FRCM) composite is composed of fibers generally in the form of fabric mesh and an inorganic matrix that has been investigated for strengthening masonry and/or reinforced concrete (RC) structures (Awani et al., 2017; Raoof et al., 2017; D'Ambrisi et al., 2011; Schladitz et al. 2012; Hegger et al., 2008). Textile reinforced mortar (TRM) and textile reinforced concrete (TRC) are in the same composite family as FRCM. This kind of composite is a promising material to replace fiber reinforced polymer (FRP) composite in the structural strengthening system. Unlike FRP, the fabric mesh in an FRCM is typically made of fibers that are individually coated but are not bonded together by a polymeric resin; i.e., FRCM uses "dry fibers" (ACI 549.4R, 2013). Compared to an FRP using an organic polymeric resin, an inorganic matrix has better inherent heat resistance, superior compatibility with the substrate, and greater long-term durability.

Regarding the mechanical behavior of FRCM composites, qualification test procedures have been investigated to understand the tensile behavior of FRCM composites and to provide a standardized method of testing FRCM composites as well. To this end, ICC-ES AC434 (2016) and RILEM TC 232-TDT (2016) have published considerable test procedures to promote the qualification of FRCM composites. Still, the observed mechanical behavior and test results in these two procedures are vastly different. The primary reason is that the two methods use different tensile test setups; however, rectangular prism FRCM specimens are adopted in both methods. The clamping grip method is recommended by RILEM TC 232-TDT (2016), in which the specimen is clamped by a sufficiently stiff steel plate with a rubber sheet placed in between the steel plate and the specimen. AC434 (2016) recommends a clevis grip method, wherein metallic plates (e.g., steel, aluminum) are bonded to the specimen ends (two at each end, one on each face) and connected to the test machine through a transverse pin. The tensile behavior of FRCM using the clamping grip method was investigated by (De Santis et al. 2017; Cevallos et al., 2015), and the clevis grip method was adopted by (Donnini et al., 2016; 2017). Arboleda et al. (2016) compared the tensile behaviors of PBO-FRCM, carbon-FRCM, and glass-FRCM using both clamping grip and clevis grip methods. Results showed that the typical failure mode of FRCM with clamping grip method was by damage to the fabric fiber close to the main crack, while the typical failure mode obtained with the clevis

gripping method was the slippage of the fabric mesh which was a combination of the pullout and tensile failure of the fibers. The stress-strain behavior was trilinear when using the clamping grip method, whereas the stress-strain behavior was bilinear when using the clevis grip method. It concluded that the choice of the gripping methods depends on the final objective of the experimental investigation, where the clamping grip method can provide a complete evaluation of the mechanical properties, and the clevis grip method is preferred when the objective is the investigation of the maximum load capacity of FRCM for the strengthening application. De Santis et al. (2018) also compared the test results of clamping grip tensile tests and clevis grip tensile tests on FRCM. It also concluded that the clevis grip method provides the FRCM tensile strain and modulus of elasticity, which consider possible slippage of the fabric within the matrix and can be used for the design of externally bonded reinforcements whose ultimate capacity relies upon the fabric–matrix bond.

Besides, the bond length of the metallic tabs in clevis grip method (Donnini et al., 2017), the classification and treatment of fabric mesh (Mercedes et al., 2018; Cevallos et al., 2015) and modification of matrix composition (Barhum et al., 2012) are also important on the tensile behavior of FRCM composite materials. However, few investigations were performed on the effect of the fabric reinforcement ratio on the tensile behavior of FRCM. The fabric reinforcement ratio is generally characterized by the number of layers of fabric mesh in the mortar matrix. Donnini et al. (2016) investigated the tensile behavior of single-layer and two-layer carbon-FRCM in which the carbon fabric was coated with epoxy resin and quartz sand, and the lime-based mortar was used as matrix. The bi-linear behavior was observed consistent with each other. Donnini et al. (2017) performed the tensile tests on FRCM specimens with one, two, and three layers of coated carbon fabric. The general tensile behavior of these FRCM specimens remained the same. However, the single-layer carbon-FRCM failed by fabric breakage due to a strong bond developed at the fiber-mortar interface, while the failure mode of multilayer carbon-FRCM shifted from fibers failure to fabric slippage within mortar because the presence of multiple layers of fabric reinforcement did not allow the crack to propagate through the entire thickness of the specimen (as in the case of single-layer) causing some delamination at the interface between the fabric and the mortar. However, the mechanical behavior of carbon-FRCM reinforced with multilayer dry carbon fabric is an issue that hasn't been thoroughly investigated yet.

1.2.2 Effectiveness of FRCM in strengthening reinforced concrete beams

In the application of FRCM composites, many experimental studies have been performed to verify the efficiency of the FRCM system in strengthening. It has been successful for strengthening or confining RC columns by using FRCM composites involving the carbon (Triantafillou et al., 2006; Zhu et al., 2018), polyparaphenylene benzobisoxazole (PBO) (Colajanni et al., 2014; Ombres et al., 2015), alkali resistant (AR) glass (Ortlepp et al., 2017) and basalt (Di Ludovico et al., 2010) fabric mesh reinforcement. Significant research contributions have also been made on the FRCM-strengthened RC beams in flexure (Babaeidarabad et al. 2014; Escrig et al., 2017; Su et al., 2019b). Ebead et al. (2017) investigated the flexural performance of RC beams having two different steel reinforcement ratios strengthened with carbon- and PBO-FRCM composites. It was confirmed that both carbon- and PBO-FRCM systems performed effectively in the improvement of the load-carrying capacity of the strengthened beams, which was influenced by the equivalent axial stiffness of the fabric reinforcement in the FRCM to the steel reinforcement ratio.

However, the strengthening effectiveness varies significantly, which strongly depends on the controlling failure modes. Koutas et al. (2019) summarized several failure modes based on the existing literature. Like the FRP system, the failure of debonding at the concrete interface, debonding from the concrete accompanied by the peeling-off of the concrete cover and rupture of fibers were observed in the FRCM system as well. Besides, concrete crushing and shear failure were also observed in both FRP and FRCM systems in the case of excessive flexural strengthening. Nevertheless, the debonding at the fabric-matrix interface and the fabric slippage within the matrix were unique in the FRCM system. The debonding at the fabric-matrix interface indicates the bond at the concrete-matrix interface is stronger than the shear bond at the fabric-matrix interface (Koutas et al., 2019). The fabric slippage is related to the low penetration of the fibers with the cementitious matrix and the poor bond characteristic at the fiber-matrix interface (Koutas et al., 2019). Consequently, some analytical studies have been performed to predict the flexural load-carrying capacity of FRCM-strengthened RC beams accounting for different failure modes.

The prediction approaches for FRCM-strengthened RC elements are still under investigation due to the complexity of strengthening behavior of FRCM composite materials. The "design by testing" approach is adopted in the ACI 549.4R (2013) in which a definition of an "effective strain" of the FRCM material is introduced that represents a strain limit globally accounting for the loss of strengthening. Modification of various bond strength models of FRP system is a feasible approach considering the identical debonding failure modes in both FRP and FRCM systems (Jung et al., 2015). Also, thanks to the large experimental database of FRCM system, some critical regression analysis was performed to obtain the predictive formulas of the load-carrying capacity of FRCM-strengthened RC elements (Ceroni et al., 2018; Bencardino et al., 2018). A more detailed introduction and discussion are presented in section 2.2 of chapter 2.

1.2.3 Fatigue of RC beams with externally bonded FRCM

A simplistic description of the fatigue phenomenon is that under cyclic loading, the load-carrying capacity of the material falls with time, and this results in failures at stress levels, which are often well below the static strength (Harris, 2003). Compared with metal material and FRP composite material, FRCM is a new and developing composite in structural engineering. It is necessary to understand the mechanisms of degradation of FRCM in service and to predict the fatigue life of FRCM. Most studies have been carried on RC beams with externally bonded FRCM subjected to static loading. Yet, few studies are dedicated to investigating the structural behavior of FRCM-strengthened RC beams under cyclic loading. Aljazaeri et al. (2017) evaluated the fatigue resistance of RC beams strengthened with PBO-FRCM under cyclic loads and post-fatigue flexural strength to failure. Pino et al. (2017) also experimentally investigated the flexural fatigue performance of PBO-FRCM-strengthened RC beams. All observed fatigue failure mechanisms for FRCM-strengthened specimens were the result of steel fracture followed by FRCM failure. FRCM improves the fatigue performance of RC structures, but the level of improvement is largely dependent on the amount of FRCM provided. Akbari et al. (2018) examined the fatigue performance of carbon-FRCM-strengthened RC beams. Analysis of applied stress range versus the number of cycles to failure suggested that FRCM systems enhanced fatigue life by controlling crack propagation in concrete.

However, the fatigue response of FRCM composites hasn't been reported yet. It is possible to

characterize the fatigue behavior of FRCM under axial tension force in a cyclic way. On the other hand, it is also necessary to evaluate the flexural fatigue behavior of RC beams with externally bonded carbon-FRCM composites considering the effect of fabric reinforcement ratios and anodic polarization in the application of the ICCP-SS intervention system.

1.3 Objectives

From these points of view, the objectives of this study are:

1) To understand the constitutive behavior of multilayer carbon-FRCM and assess the mechanical degradation of carbon-FRCM suffered from anodic polarization in the electrochemical process.

2) To understand the fatigue degradation characterizations and to propose the fatigue life prediction for both multilayer carbon-FRCM and anodically polarized carbon-FRCM.

3) To evaluate the strengthening behavior of RC beams with externally bonded multilayer carbon-FRCM under static and cyclic loading.

4) To investigate the effect of anodically polarized carbon-FRCM in the ICCP-SS system on the strengthening characterizations of RC beams under static and cyclic loading.

1.4 Outline of the dissertation

The experimental program in this dissertation is presented in Fig. 1.4. The tensile tests of carbon-FRCM and four-point bending tests of RC beams with externally bonded carbon-FRCM were carried out in which the static and cyclic loading were involved. In addition, the parameters related to the carbon-FRCM included the number of layers of carbon fabric mesh and different anodic polarization in the process of accelerated electrochemical (AC-EC) tests that was a testing scenario instead of the application of ICCP-SS system.

The dissertation includes six chapters as:

Chapter 1 describes the background of the study on the proposal of the ICCP-SS intervention system as well as the application of dual-functional carbon-FRCM composites. The literature review on the characterization of FRCM composites and previous studies on the FRCM-strengthened beams under static and fatigue loading are introduced. The objectives of the present research and organization of this dissertation are also described.

Chapter 2 presents an investigation of RC beams with externally bonded multilayer carbon-FRCM (M/C-FRCM) under static loading. The influence of the number of layers of carbon fabric (CF) mesh embedded into the mortar matrix was considered. The static tensile tests of M/C-FRCM composites were carried out, followed by the four-point bending tests of RC beams with externally bonded M/C-FRCM under static loading. The constitutive behavior of M/C-FRCM composites was clarified, and the effectiveness of M/C-FRCM in strengthening RC beams was also verified. Finally, the prediction formulas in flexure for RC beams with externally bonded FRCM were proposed.

Chapter 3 shows an investigation of RC beams with externally bonded M/C-FRCM under cyclic loading. The tensile tests of M/C-FRCM and four-point bending tests of RC beams with

externally bonded M/C-FRCM were conducted under cyclic loading. The layers of carbon fabric mesh and applied load levels were considered. The fatigue degradation characterizations of M/C-FRCM and RC beams with externally bonded M/C-FRCM were analyzed. Based on the test results, the fatigue life model and the fatigue strength model of M/C-FRCM were proposed. Finally, a method for predicting the fatigue life of beams with externally bonded FRCM composites was also presented.

Chapter 4 describes an investigation of RC beams with externally bonded anodically polarized carbon-FRCM (AP/C-FRCM) under static loading. The accelerated electrochemical (AC-EC) tests of carbon-FRCM were performed before the tensile tests of AP/C-FRCM and four-point bending tests of beams with externally bonded AP/C-FRCM. The mechanical degradation of carbon-FRCM caused by the anodic polarization in the process of AC-EC tests was discussed. The influence of anodic polarization on the effectiveness of carbon-FRCM in strengthening beams was described and compared between experimental and analytical results.

Chapter 5 presents an investigation of RC beams with externally bonded AP/C-FRCM under cyclic loading. By considering different quantities of anodic polarization, the tensile tests of AP/C-FRCM and four-point bending tests of RC beams with externally bonded AP/C-FRCM were carried out under cyclic loading at different applied load levels. The fatigue life model and the fatigue strength model of AP/C-FRCM considering the degradation of anodic polarization were developed based on the test results. A new S-N curve was proposed for predicting the fatigue life of beams with externally bonded fabric reinforcement by inorganic matrix.

Chapter 6 shows the conclusions and significant findings in this study. Some suggestions for future studies are also presented.

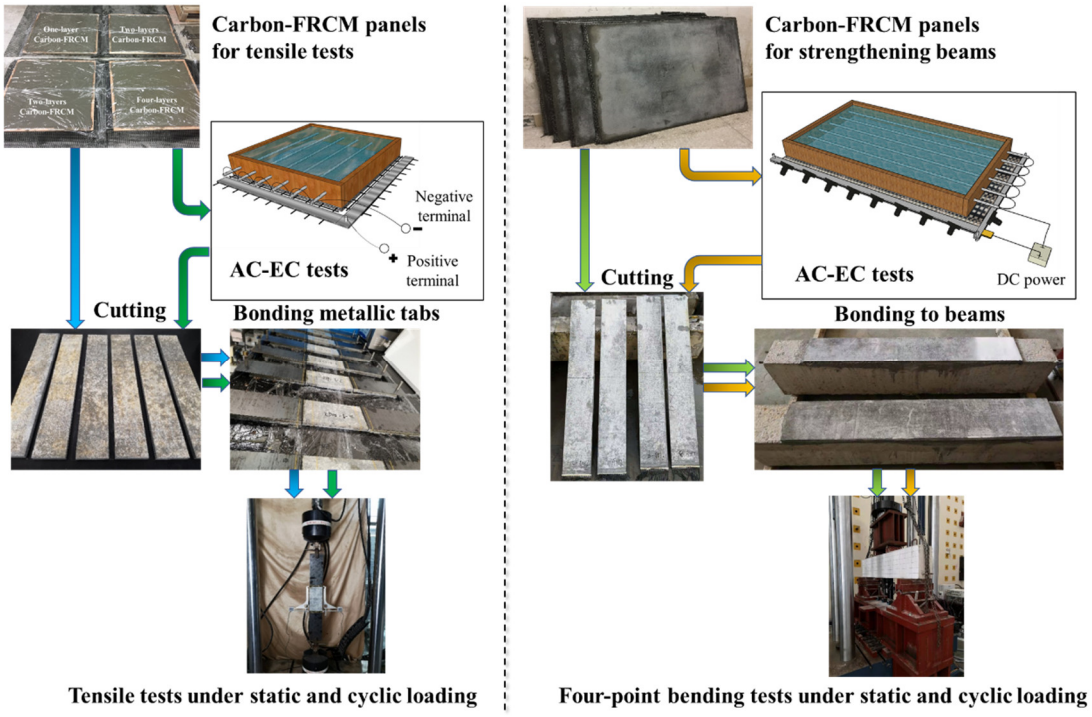

Fig. 1.4 Experimental tests involved in the dissertation.

List of Figures

References

AC434, 2016. Acceptance Criteria for Masonry and Concrete Strengthening Using Fabric-reinforced Cementitious Matrix (FRCM) and Steel Reinforced Grout (SRG) Composite Systems. ICC Evaluation Service.

ACI 440.2R, 2008. Guide for the Design and Construction of Externally Bonded FRP Systems for Strengthening Concrete Structures. American Concrete Institute, U.S.A.

ACI 549.4R, 2013. Guide to design and construction of externally bonded fabric-reinforced cementitious matrix (FRCM) systems for repair and strengthening concrete and masonry structures. American Concrete Institute, U.S.A.

Akbari Hadad, H., Nanni, A., Ebead, U. A.and El Refai, A., 2018. Static and fatigue performance of FRCM-strengthened concrete beams. Journal of Composites for Construction, 22(5), 04018033.

Aljazaeri, Z.R. and Myers, J.J., 2017. Fatigue and flexural behavior of reinforced-concrete beams strengthened with fiber-reinforced cementitious matrix. Journal of Composites for Construction, 21(1), 04016075.

Arboleda, D., Carozzi, F. G., Nanni, A. and Poggi, C., 2016. Testing procedures for the uniaxial tensile characterization of fabric-reinforced cementitious matrix composites. Journal of Composites for Construction, 20(3), 04015063.

Awani, O., El-Maaddawy, T. and Ismail, N., 2017. Fabric-reinforced cementitious matrix: A promising strengthening technique for concrete structures. Construction and Building Materials, 132, 94-111.

Babaeidarabad, S., Loreto, G. and Nanni, A., 2014. Flexural strengthening of RC beams with an externally bonded fabric-reinforced cementitious matrix. Journal of Composites for Construction, 18(5), 04014009.

Barhum R. and Mechtcherine V., 2012. Effect of short, dispersed glass and carbon fibres on the behaviour of textile-reinforced concrete under tensile loading. Engineering Fracture Mechanics, 92:56-71.

Barlo T.J., 2001. Origin and validation of the 100-mV polarization criterion. CORROSION 2001. NACE International.

Bencardino, F., Carloni, C., Condello, A., Focacci, F., Napoli, A. and Realfonzo, R., 2018. Flexural behaviour of RC members strengthened with FRCM: State-of-the-art and predictive formulas. Composites Part B: Engineering, 148, 132-148.

BS EN 1504-10, 2017. Products and Systems for the Protection and Repair of Concrete Structures-Definitions, Requirements, Quality Control and Evaluation of Conformity. British Standards Institution.

CEB-FIP, fib bulletin 14, 2001. Externally bonded FRP reinforcement for RC structures.

International Federation for Structural Concrete, Switzerland.
Ceroni, F. and Salzano, P., 2018. Design provisions for FRCM systems bonded to concrete and masonry elements. Composites Part B: Engineering, 143, 230-242.
Cevallos, O.A. and Olivito, R.S., 2015. Effects of fabric parameters on the tensile behaviour of sustainable cementitious composites. Composites Part B: Engineering, 69:256-66.
Colajanni, P., De Domenico, F., Recupero, A. and Spinella, N., 2014. Concrete columns confined with fibre reinforced cementitious mortars: experimentation and modelling. Construction and Building Materials, 52, 375-384.
Cramer, S.D., Bullard, S.J., Covino, B.S., Holcomb, G.R., Russell, J.H., Cryer, C.B. and Laylor, H.M., 2002. Carbon Paint Anode for Reinforced Concrete Bridges in Coastal Environments. CORROSION 2002. NACE International.
D'Ambrisi, A. and Focacci, F., 2011. Flexural strengthening of RC beams with cement-based composites. Journal of Composites for Construction, 15(5):707-20.
D'Ambrisi, A., Feo, L. and Focacci, F., 2013. Experimental and analytical investigation on bond between Carbon-FRCM materials and masonry. Composites Part B: Engineering, 46:15-20.
D'Ambrisi, A., Focacci, F., Luciano, R., Alecci, V. and De Stefano, M., 2015. Carbon-FRCM materials for structural upgrade of masonry arch road bridges. Composites Part B: Engineering, 75:355-66.
De Santis, S., Carozzi, F. G., de Felice, G. and Poggi, C., 2017. Test methods for textile reinforced mortar systems. Composites Part B: Engineering, 127, 121-132.
De Santis, S., Hadad, H. A., De Caso y Basalo, F., De Felice, G. and Nanni, A., 2018. Acceptance criteria for tensile characterization of fabric-reinforced cementitious matrix systems for concrete and masonry repair. Journal of Composites for Construction, 22(6), 04018048.
Di Ludovico, M., Prota, A. and Manfredi, G., 2010. Structural upgrade using basalt fibers for concrete confinement. Journal of Composites for Construction, 14(5), 541-552.
Donnini, J., Corinaldesi, V. and Nanni, A., 2016. Mechanical properties of FRCM using carbon fabrics with different coating treatments. Composites Part B: Engineering, 88, 220-228.
Donnini, J. and Corinaldesi, V., 2017. Mechanical characterization of different FRCM systems for structural reinforcement. Construction and Building Materials, 145, 565-575.
Ebead, U., Shrestha, K.C., Afzal, M.S., El Refai, A. and Nanni, A., 2017. Effectiveness of fabric-reinforced cementitious matrix in strengthening reinforced concrete beams. Journal of Composites for Construction, 21(2), 04016084.
El-Mihilmy, M.T. and Tedesco, J.W., 2000. Analysis of reinforced concrete beams strengthened with FRP laminates. Journal of Structural Engineering, 126(6):684-91.
Escrig, C., Gil, L. and Bernat-Maso, E., 2017. Experimental comparison of reinforced concrete beams strengthened against bending with different types of cementitious-matrix composite materials. Construction and Building Materials, 137:317-29.
Gadve, S., Mukherjee, A. and Malhotra, S.N., 2010. Corrosion Protection of Fiber-Reinforced Polymer-Wrapped Reinforced Concrete. ACI Materials Journal, 107(4):349-56.
Gadve, S., Mukherjee, A. and Malhotra, S.N., 2011. Active protection of fiber-reinforced polymer-wrapped reinforced concrete structures against corrosion. Corrosion, 67(2):025002-1.
GB 50367, 2013. Code for design of strengthening concrete structure. Ministry of Housing and Urban-Rural Development of the People's Republic of China, China. (In Chinese)
Harris, B., 2003. Fatigue in composites: science and technology of the fatigue response of fibre-

reinforced plastics. Woodhead Publishing.
Hegger, J. and Voss, S., 2008. Investigations on the bearing behaviour and application potential of textile reinforced concrete. Engineering Structures, 30(7):2050-6.
JSCE, 2001. Recommendations for upgrading of concrete structures with use of continuous fiber sheets. Japan Society of Civil Engineers, Japan.
JSCE, 2008. Recommendations for Design and Construction of High-Performance Fiber Reinforced Cement Composites with Multiple Fine Cracks (HPFRCC). Concrete Engineering Series 82. Japan Society of Civil Engineers, Japan.
Jung, K., Hong, K., Han, S., Park, J. and Kim, J., 2015. Prediction of flexural capacity of RC beams strengthened in flexure with FRP fabric and cementitious matrix. International Journal of Polymer Science, 2015.
Koutas, L.N., Tetta, Z., Bournas, D.A. and Triantafillou, T., 2019. Strengthening of Concrete Structures with Textile Reinforced Mortars: State-of-the-Art Review. Journal of Composites for Construction, 23(1), 03118001.
Lambert, P., Van Nguyen, C., Mangat, P. S., O'Flaherty, F. J. and Jones, G., 2015. Dual function carbon fibre fabric strengthening and impressed current cathodic protection (ICCP) anode for reinforced concrete structures. Materials and Structures, 48(7), 2157-2167.
Lee-Orantes, F., Torres-Acosta, A. A., Martínez-Madrid, M. and López-Cajún, C., 2007. Cathodic protection in reinforced concrete elements, using carbon fibers base composites. ECS Transactions, 3(13), 93-98.
Mahdi, C., 2010. Pan-based carbon fiber as anode material in cathodic protection systems for concrete structures. Doctoral degree. Norwegian University of Science and Technology.
Mehta, P.K., 1991. Concrete durability-fifty years progress. Proceedings of the 2nd International Conference on Concrete Durability, Montreal, QC, Canada.
Mercedes, L., Gil, L. and Bernat-Maso, E., 2018. Mechanical performance of vegetal fabric reinforced cementitious matrix (FRCM) composites. Construction and Building Materials, 175:161-73.
Mork, J.H., Mayer, S., Rosenbom, K., Tuveson-Carlstrom, L., Sederholm, B. and Sandberg, B., 2006. Cathodic protection of concrete structures with a carbon fibre mesh anode. EUROCORR 2006.
NACE SP0290, 2007. Impressed current cathodic protection of reinforcing steel in atmospherically exposed concrete structures. NACE International, Houston, TX, USA.
NACE SP0294, 2016. Impressed current cathodic protection of reinforcing steel in atmospherically exposed concrete structures. NACE International, Houston, TX, USA.
Ombres, L. and Verre, S., 2015. Structural behaviour of fabric reinforced cementitious matrix (FRCM) strengthened concrete columns under eccentric loading. Composites Part B: Engineering, 75, 235-249.
Ortlepp, R. and Ortlepp, S., 2017. Textile reinforced concrete for strengthening of RC columns: A contribution to resource conservation through the preservation of structures. Construction and Building Materials, 132, 150-160.
Pino, V., Akbari Hadad, H., De Caso y Basalo, F., Nanni, A., Ali Ebead, U. and El Refai, A., 2017. Performance of FRCM-strengthened RC beams subject to fatigue. Journal of Bridge Engineering, 22(10), 04017079.
RILEM TC 232-TDT, 2016. Test methods and design of textile reinforced concrete. Material and

Structures, 49:4923-27.

Raoof, S.M., Koutas, L.N. and Bournas, D.A., 2017. Textile-reinforced mortar (TRM) versus fibre-reinforced polymers (FRP) in flexural strengthening of RC beams. Construction and Building Materials, 151:279-91.

Schladitz, F., Frenzel, M., Ehlig, D. and Curbach, M., 2012. Bending load capacity of reinforced concrete slabs strengthened with textile reinforced concrete. Engineering structures, 40:317-26.

Sonnenschein, R., Gajdosova, K. and Holly, I., 2016. FRP composites and their using in the construction of bridges. Procedia Engineering, 161:477-82.

Su, M.N., Wei, L.L., Zhu, J.H., Ueda, T., Guo, G.P. and Xing, F., 2019a. Combined Impressed Current Cathodic Protection and FRCM Strengthening for Corrosion-Prone Concrete Structures. Journal of Composites for Construction, 23(4):04019021.

Su, M.N., Wei, L.L., Zeng, Z.W., Ueda, T., Xing, F. and Zhu, J.H., 2019b. A solution for sea-sand reinforced concrete beams. Construction and Building Materials, 204:586-96.

Su, M.N., Zeng, C., Li, W.Q., Zhu, J.H., Lin, W.H., Ueda, T. and Xing, F., 2020. Flexural performance of corroded continuous RC beams rehabilitated by ICCP-SS. Composite Structures, 232:111556.

Sun, H.F., Wei, L.L., Zhu, M.C., Han, N.X., Zhu, J.H. and Xing, F., 2016. Corrosion behavior of carbon fiber reinforced polymer anode in simulated impressed current cathodic protection system with 3% NaCl solution. Construction and Building Materials, 112:538-46.

Tettamanti, M., 1997. Cathodic prevention and protection of concrete elements at the Sydney Opera House. Materials Performance, 36(9):21-5.

Triantafillou, T.C., Papanicolaou, C.G., Zissimopoulos, P. and Laourdekis, T., 2006. Concrete confinement with textile-reinforced mortar jackets. ACI Materials Journal, 103(1):28.

Van Nguyen, C., Lambert, P., Mangat, P., O'Flaherty, F. and Jones, G., 2012. The performance of carbon fibre composites as ICCP anodes for reinforced concrete structures. ISRN Corrosion, 2012.

Wei, L.L., Zhu, J.H., Ueda, T., Su, M.N., Liu, J., Liu, W., Tang, L.P. and Xing, F., 2019. Tensile behaviour of carbon fabric reinforced cementitious matrix composites as both strengthening and anode materials. Composite Structures, 111675.

Weyers, R.E., Prowell, B.D., Sprinkel, M.M. and Vorster, M., 1993. Concrete bridge protection, repair, and rehabilitation relative to reinforcement corrosion: A methods application manual. Contract, 100:103.

Zhang, E.Q., Tang, L. and Zack, T., 2016. Carbon fiber as anode material for cathodic prevention in cementitious materials. 5th International Conference on the Durability of Concrete Structures, Shenzhen University, Shenzhen, Guangdong, P.R.China. 300-08.

Zhang, E.Q., Tang, L., Bernin, D. and Jansson, H., 2018. Effect of the paste–anode interface under impressed current cathodic protection in concrete structures. Materials and Corrosion, 69(8):1104-16.

Zhang, E.Q. and Tang, L., 2019. Application of CFRP as anode in cathodic protection for steel reinforced concrete–a review. MATEC Web of Conferences, 289:03007.

Zhu, J.H., Zhu, M.C., Han, N.X., Xing, F., Liu, W. and Bertolini, L., 2014a. Behavior of CFRP plate in simulated ICCP system of concrete structures. 4th International Conference on the Durability of Concrete Structures, Purdue University, West Lafayette, IN, USA. 363-68.

Zhu, J.H., Zhu, M.C., Han, N.X., Liu, W. and Xing, F., 2014b. Electrical and mechanical performance of carbon fiber-reinforced polymer used as the impressed current anode material. Materials, 7(8):5438-53.

Zhu, J.H., Wei, L.L., Guo, G.P. and Zhu, A., 2016a. Mechanical and Electrochemical Performance of Carbon Fiber Reinforced Polymer in Oxygen Evolution Environment. Polymers, 8(11):393.

Zhu, J.H., Guo, G.P., Wei, L.L., Zhu, M.C. and Chen, X.C., 2016b. Dual function behavior of carbon fiber-reinforced polymer in simulated pore solution. Materials, 9(2):103.

Zhu, J.H., Wei, L.L., Moahmoud, H., Redaelli, E., Xing, F. and Bertolini, L., 2017. Investigation on CFRP as dual-functional material in chloride-contaminated solutions. Construction and Building Materials, 151:127-37.

Zhu, J.H., Su, M.N., Huang, J.Y., Ueda, T. and Xing, F., 2018. The ICCP-SS technique for retrofitting reinforced concrete compressive members subjected to corrosion. Construction and Building Materials, 167, 669-679.

Zhu, J.H, Zeng, C.Q., Su, M.N., Zeng, Z.W. and Zhu, A., 2019. Effectiveness of a dual-functional intervention method on the durability of reinforced concrete beams in marine environment. Construction and Building Materials, 222:633-42.

CHAPTER 2

INVESTIGATION OF RC BEAMS WITH EXTERNALLY BONDED M/C-FRCM UNDER STATIC LOADING

2.1 Introduction

The study in this chapter aims to assess the flexural behavior of RC beams with externally bonded carbon-FRCM having different layers of carbon fabric (CF) mesh and to develop a procedure of prediction formulas in flexure for carbon-FRCM-strengthened beams. For evaluating the contribution of carbon-FRCM to the load-carrying capacity of strengthened beams, the tensile characteristics of multilayer carbon-FRCM (M/C-FRCM) were studied through the uniaxial tensile tests, followed by the four-point bending tests of RC beams with externally bonded M/C-FRCM. The available prediction approaches for FRCM-strengthened RC in flexure were summarized before proposing predictive formulas in this chapter. Finally, the comparison of load-carrying capacity and deflection between experimental and predicted results was performed.

2.2 Available prediction approaches for FRCM-strengthened RC in flexure

2.2.1 Basis of prediction approach

Constitutive models

To achieve the plane sectional analysis of an FRCM-strengthened rectangular reinforced concrete cross-section at different load-carrying limit states, the basic assumption is that the plane section remains plane after loading. Thus, to calculate the load-carrying capacity in flexure, it is necessary to obtain the constitutive properties of each material components, including the concrete, steel bar, and FRCM composite. The conventional stress-strain model of concrete and steel rebar as per the JSCE guideline for concrete (2007) are shown in Fig. 2.1. The concrete is modeled as a nonlinear ascending branch followed by keeping plateau where the strain corresponding to compressive strength and ultimate strain are 0.002 and 0.0035, respectively. The steel rebar is modeled as a bilinear behavior where the tensile strength maintains constant as yielding of steel.

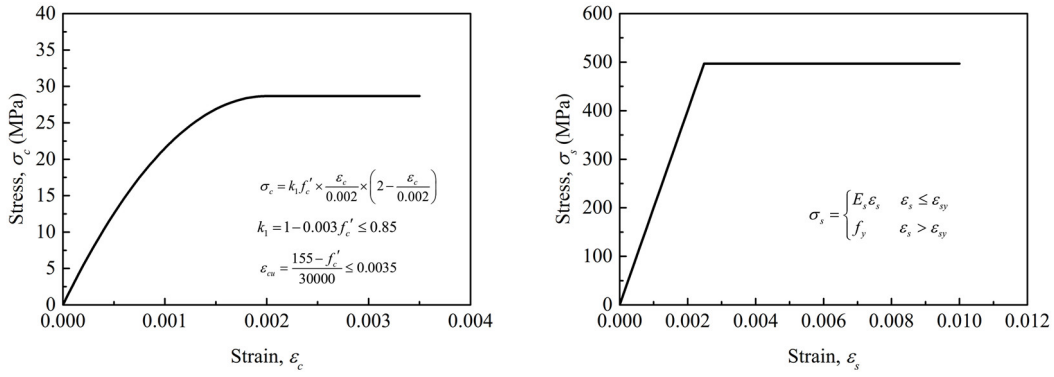

(a) Concrete (b) Steel bar

Fig. 2.1 Constitutive stress-strain model of concrete and steel bar.

The tensile behavior of FRCM composite material is tested as per AC434 (2016) that is an acceptance criterion for the application of FRCM composites, which is developed by ICC Evaluation Service (ICC-ES). Fig. 2.2(a) is an expected tensile stress-strain curve of an FRCM specimen that is a bilinear constitutive behavior. The first part represents the tensile behavior of non-cracked FRCM specimens, while the second part describes the tensile behavior of FRCM after cracking of the mortar matrix. The characterizations of the first part are the high tensile modulus and low tensile strain. The reason is that the tensile strain is calculated in terms of the total cross-sectional area of fabric without considering the cross-sectional area of the matrix. However, the mortar matrix and fabric sustain the tensile load together. The characterizations of the second part are the low tensile modulus and high tensile strain. The fabric is recognized as the dominant load-carrying component after cracking of mortar matrix. Whereas, the poor penetration of the matrix into the fiber bundles results in the limitation of the bond between fibers and matrix. It causes the fabric slippage from the mortar matrix leading to the high strain of FRCM according to the measurement of strain as per the AC434 (2016). Regarding the application of the FRCM model to predict the flexural behavior of FRCM-strengthened concrete members, only the second linear part of the tensile stress-strain curve is used according to the assumption of the ACI 549.4R (2013) as showing in Fig. 2.2(b). The pre-cracking behavior of FRCM seems to be neglected, which leads to the conservation of effective tensile strength at the failure of FRCM-strengthened concrete members.

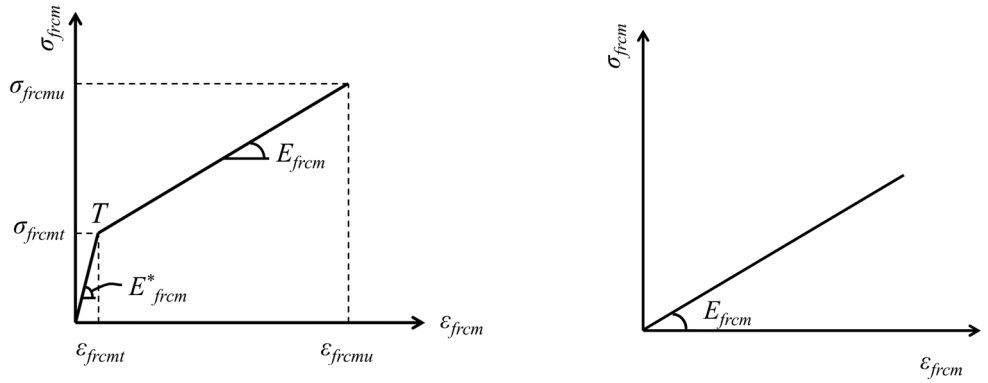

(a) Tensile stress-strain behavior of FRCM as per the AC434 (2016)

(b) Constitutive model of FRCM in the ACI 549.4R (2013)

Fig. 2.2 Constitutive model of FRCM composite.

Interfacial behavior of FRCM-concrete substrate

To assess the strengthening behavior of RC members using FRCM composite, the bond behavior of the FRCM-concrete interface is crucial to understand the strengthening mechanism in which the force is transferred from the fabric to the around matrix and eventually to the concrete substrate (D'Antino et al., 2018). Several studies have been conducted to clarify the bond behavior of FRCM to the concrete substrate by using the single-lap shear (Sneed et al., 2014; Ombres., 2015; D'Antino et al., 2016) that is shown as Fig. 2.3(a) and double-lap shear (Awani et al., 2015; Raoof et al., 2016) tests as showing in Fig. 2.3(b). The shear stress-slip law for bonding FRCM to the concrete substrate is presented in Fig. 2.4. D'Antino et al. (2015) proposed a parabolic/exponential law for the bond behavior between FRCM and concrete through the single-lap shear tests. Grande and Milani (2018) proposed a bilinear relationship based on the numerical study developed by using a newly conceived efficient spring-model. As far as the failure mode is concerned, the most observed

failure is the debonding failure at the fabric-matrix and the matrix-concrete substrate interface plane. Younis and Ebead (2018) proposed the simplified models to predict the bond strength corresponding to both debonding failure modes that are presented in Eqs. (2.1) and (2.2). The detailed description of both equations can refer to Younis and Ebead (2018).

$$\tau_{FD} = \alpha_{FD}\beta_L\sqrt{\frac{nE_f\sqrt{f_m}}{t_f}} \quad \text{.....(2.1)}$$

$$\tau_{DB} = \alpha_{DB}\beta_L\sqrt{\frac{E_{frcm}\sqrt{f_m}}{t_{frcm}}} \quad \text{.....(2.2)}$$

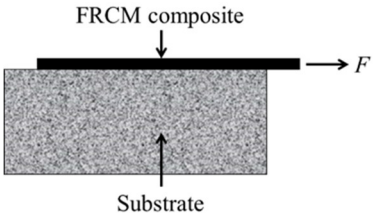

(a) Single-lap shear test

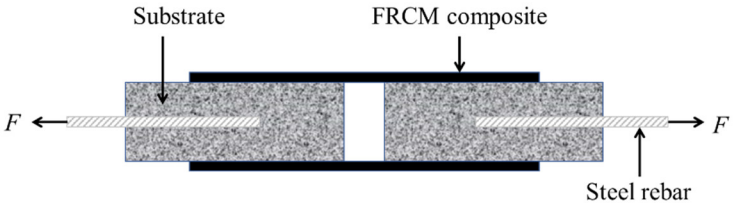

(b) Double-lap shear test

Fig. 2.3 Schematic diagrams of test methods for bond behavior between FRCM and concrete.

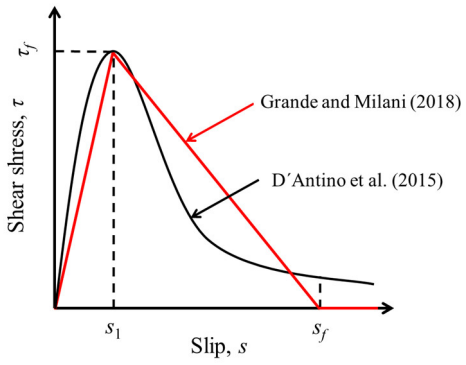

Fig. 2.4 Shear stress-slip law for bonding FRCM to concrete.

Failure modes

When strengthening RC beam by FRCM composite, six possible failure modes can take place, which is presented in Fig. 2.5. Mode 1 is a concrete crushing failure in the extreme compression zone that occurs when extensive reinforcement materials are used involving steel reinforcement and

external FRCM composites. In general, this failure is considered brittle since the steel reinforcement does not reach yielding. Mode 2 and mode 3 are the debonding failure at the matrix-concrete and fabric-matrix interface plane, respectively. They are also considered brittle when the debonding failure occurs, although the strengthened beam becomes an un-strengthened beam after the debonding of FRCM. Mode 4 is the fabric rupture in the FRCM composite. Mode 5 is the peeling-off of concrete cover at the cut-off end to the concrete. The failure of mode 1, mode 2, mode 4 and mode 5 are also observed in the FRP system. However, mode 6 is fabric slippage from the mortar matrix that is differentiated from the FRP system. This is due to the low penetration of the matrix into fiber yarns in the FRCM composite. While fabric slippage is considered as ductile because large deformation of the strengthened beam will occur before the ultimate failure. It gives earlier forewarning than a brittle failure mode, which mostly occurs suddenly. Several experimental studies (D'Ambrisi and Focacci, 2011; Ebead et al., 2017; Elghazy et al., 2017, 2018; Jabr et al., 2017; Aljazaeri et al., 2019; Su et al., 2019) have observed such fabric slippage failure mode. Accordingly, fabric slippage is a common failure mode, especially for using the fabric without impregnating polymeric resin, in the FRCM strengthening beam.

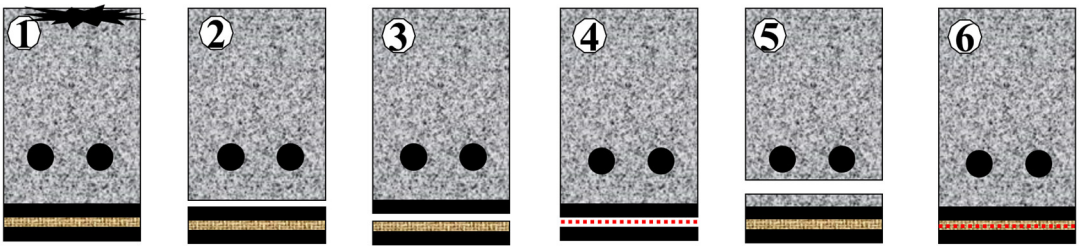

Fig. 2.5 Failure modes for RC beams with externally bonded FRCM composite.

2.2.2 Design approach by standardized guidelines

ACI 549.4R (2013) - Guide to design and construction of externally bonded fabric reinforced cementitious matrix (FRCM) systems for repair and strengthening concrete and masonry structures

The American Concrete Institute (ACI) has published the guide to design and construction of externally bonded FRCM for strengthening concrete and masonry structures - ACI 549.4R (2013) – that is currently the only available guideline for FRCM system. The design approach in the ACI 549.4R (2013) is design by testing where the tensile tests of a specified FRCM composite material in the light of AC434 (2016) is necessary before prediction. The tensile stress-strain behavior of FRCM is presented in Fig. 2.2. In the ACI 549.4R (2013), a limitation of an effective tensile strain (ε_{frcme}) in the FRCM attained at failure is defined that is the minimum value between the design ultimate tensile strain (ε_{frcmd}) and 0.012 as shown in Eq. (2.3). The ε_{frcmd} is defined as the average value of ultimate tensile strain (ε_{frcmu}) minus one standard deviation based on the results of tensile tests performed in accordance with the AC434 (2016).

$$\varepsilon_{frcme} = \min\left(\varepsilon_{frcmd}, 0.012\right) \qquad \text{……..……(2.3)}$$

Consequently, the effective tensile stress (σ_{frcme}) in the FRCM for strengthening in flexure attained at failure is calculated according to Eq. (2.4).

$$\sigma_{frcme} = E_{frcm}\varepsilon_{frcme} \quad \text{……..……(2.4)}$$

Where E_{frcm} is the average modulus of elasticity of the cracked FRCM specimens, which is obtained from the second linear part of the tensile stress-strain curve of the FRCM as shown in Fig. 2.2.

New Italian guidelines ready to be published

In addition to the published ACI 549.4R (2013), other countries also make great efforts to the publication of design guidelines for the FRCM system. In Italy, two new guidelines providing acceptance criteria and design provisions for externally bonded FRCM in strengthening concrete and masonry structures will be published by the Ministry of Public Works (Ascione et al., 2018).

The bond properties of the FRCM composite to a specific substrate are not investigated in the AC434 (2016). The new ready-to-be-published Italian guidelines are the design by testing as well, however, involving both the debonding tests and tensile tests. The debonding tests are the single-lap shear tests (see Fig. 2.3(a)) of an adopted FRCM to a specified substrate to obtain the maximum force (F_{max}) at failure. The tensile tests include the tests of FRCM specimens and dry fabric mesh to gain some fundamental constitutive characteristics such as ultimate tensile stress (σ_{frcmu}) and strain (ε_{frcmu}) of FRCM composites and ultimate tensile stress (σ_{fu}), strain (ε_{fu}) and Young modulus (E_f) of the dry fabric mesh. The dry fabric mesh is comprised of fibers that are individually coated but are not bonded together by a polymeric resin (ACI 549.4R, 2013).

Conventional limit stress ($\sigma_{lim,conv}$) is obtained by debonding tests, as illustrated as Eq. (2.5). The stress is calculated using the cross-section area of dry fabric mesh (A_f) in the FRCM composite, without considering the cementitious matrix. Then, the corresponding conventional limit strain ($\varepsilon_{lim,conv}$) is derived from the tensile tests of dry fabric mesh, according to Eq. (2.6).

$$\sigma_{\lim,conv} = \frac{F_{\max}}{A_f} \quad \text{……..……...(2.5)}$$

$$\varepsilon_{\lim,conv} = \frac{\sigma_{\lim,conv}}{E_f} \quad \text{……..……...(2.6)}$$

Considering the phenomenon of debonding, the tensile strain ($\varepsilon^{(\alpha)}_{lim,conv}$) and stress ($\sigma^{(\alpha)}_{lim,conv}$) of the fabric for strengthening at failure have to be utilized as following Eqs. (2.7) and (2.8).

$$\varepsilon^{(\alpha)}{}_{\lim,conv} = \alpha\varepsilon_{\lim,conv} \quad \text{……..……..(2.7)}$$

$$\sigma^{(\alpha)}{}_{\lim,conv} = E_f\varepsilon^{(\alpha)}{}_{\lim,conv} \quad \text{……..……..(2.8)}$$

The coefficient α is assumed to 1.5 (Ascione et al., 2018). Finally, the tensile stress of the fabric should not exceed the ultimate tensile stress (σ_{frcmu}) of the FRCM composite and the ultimate tensile stress (σ_{fu}) of the dry fabric mesh, as shown in Eq. (2.9).

$$\sigma^{(\alpha)}{}_{\lim,conv} \le \min\left(\sigma_{frcmu}, \sigma_{fu}\right) \quad \text{……..……..(2.9)}$$

2.2.3 Prediction approach by modification of FRP system guidelines

Compared to the FRCM system, the mature studies of the FRP system have obtained through many experiments, finite element analysis (FEA), and theoretical analysis since the emerging application of FRP material. Indeed, the bond behavior between FRCM and FRP system is different to some extent due to the adhesive being used. However, it is considered that the bond-slip concept based on fracture mechanics is similar in both cases (Jung et al., 2015). Therefore, the bond strength models of the FRCM system can be modified by using the models of the FRP system to evaluate the effective stress of the FRCM composite. Jung et al. (2015) proposed a new bond strength model that was based on the model of FRP by Teng et al. (2003), as illustrated as Eq. (2.10).

$$\sigma_p = \alpha\beta_p\beta_L\sqrt{\frac{E_p\sqrt{f_c'}}{t_p}}$$

$$\beta_p = \sqrt{\frac{2-b_p/b_c}{1+b_p/b_c}}$$

$$\beta_L = \begin{cases} 1, & \text{if } L \geq L_e \\ \sin\dfrac{\pi L}{\sqrt{f_c'}} & \text{if } L < L_e \end{cases} \qquad \text{……..……(2.10)}$$

$$L_e = \sqrt{\frac{E_p t_p}{\sqrt{f_c'}}}$$

In the FRP system, the total nominal thickness of FRP (t_p) is calculated as Eq. (2.11). However, D'Ambrisi et al. (2013) conducted the experimental studies for bond-slip behavior between an FRCM and concrete. They suggested that the strain of fabric mesh corresponding to its debonding (ε_{f_deb}) decreases at the rate of $1/\sqrt{n}$ with multilayer fabric mesh. n is the layers of fabric mesh. Therefore, Eq. (2.11) can be modified into Eq. (2.12) in the bond strength model for the FRCM system (Jung et al., 2015).

$$t_p = t_1 \times n \qquad \text{……..(2.11)}$$

$$t_p = t_1 \times \sqrt{n} \qquad \text{……..(2.12)}$$

Where t_1 is the nominal thickness of one layer of fabric reinforcement.

Besides, the reduction factor α was given as 0.427 by Teng et al. (2003). Further, Jung et al. (2015) calibrated the coefficient α as 0.729 from regression analysis to account for the difference between FRCM and FRP system.

2.2.4 Prediction approach based on the analysis of available database

A critical review based on experimental bond tests

Ceroni et al. (2018) collected a total of 856 shear bond test results from the scientific literature. The bond tests were carried out to investigate the bond behavior of several FRCM systems bonded to different substrates, including concrete and masonry. Among the total database, 509 data are

related to the masonry substrate, while 347 data refer to the concrete substrate (Ceroni et al., 2018). For the bond tests conducted on the concrete substrate, 87% of the failure mode was debonding that includes the debonding at the fabric-mortar interface plane and the mortar-substrate interface plane (Ceroni et al., 2018). Consequently, the analysis of the data referring debonding failure has evidenced that the theoretical maximum strain ($\varepsilon_{max,th}$) increased with the compressive strength of concrete and decreased with the axial stiffness of the fabric mesh in the FRCM composite as illustrated as Eq. (2.13) (Ceroni et al., 2018).

$$\varepsilon_{\max,th} = \alpha \cdot \left(E_f \cdot A_f\right)^{\beta} \left(f_c\right)^{\gamma} \quad \text{……..……(2.13)}$$

Where E_f and A_f are the Young moduli and cross-section area of the dry fabric mesh, f_c is the compressive strength of the concrete substrate.

The parameters α, β, and γ have been assessed through a multivariate regression analysis leading to minimizing the sum of the squared differences between the experimental and theoretical results. Ceroni et al. (2018) determined the results of parameters, as shown in Eq. (2.14). It is noted that only data referring to debonding failure mode has been considered for the regression.

$$\begin{aligned} &\alpha = 0.008 \\ &\beta = -0.30 \\ &\gamma = 1.15 \end{aligned} \quad \text{……...……...(2.14)}$$

A critical analysis based on experimental flexural tests

Bencardino et al. (2018) collected the experimental results on RC beams and slabs strengthened with a variety of FRCM composites, where a total of 94 data were obtained. Among the 94 data, 25 are relevant to the carbon-FRCM, 38 to the PBO-FRCM, 22 to the S-FRCM (steel fabric), 5 and 4 to the B-FRCM (basalt fabric) and G-FRCM (glass fabric), respectively (Bencardino et al. 2018). The database is used to identify critical factors of the flexural behavior of FRCM-strengthened RC members.

For the S-FRCM system, a clear trend of the evaluated debonding strain (ε_{deb}) against the product E_f and t_f was found to suggest the proposal of the prediction formulas, as illustrated as Eq. (2.15). Considering the debonding failure is at the steel mesh-matrix interface plane rather than the concrete-matrix interface plane so that the proposed formulas do not account for the strength of the concrete substrate.

$$\begin{aligned} &\varepsilon_{deb} = 2.24\left(E_f \cdot t_f\right)^{-0.52} \\ &t_f = t_1 \times n \end{aligned} \quad \text{…….……(2.15)}$$

Where ε_{deb} is the debonding strain of S-FRCM composites, E_f is the Young modulus of steel fabric, t_f is the total thickness of steel fabric, t_1 is the thickness of one layer of steel fabric, and n is the number of layers of steel fabric.

However, Bencardino et al. (2018) stated that for carbon-FRCM and PBO-FRCM systems, a clear dependence of the debonding strain on the axial stiffness of the fabric could not be inferred from the experimental results. Further experimental work is needed to identify a procedure for the evaluation of the debonding strain.

2.2.5 Assessment of available prediction approaches

As far as the design approach by standardized guidelines “design by testing” is concerned, two issues should be considered when the design approach in the ACI 549.4R (2013) is adopted. Firstly, it leads to a general underestimation of the FRCM contribution to flexural strength since only the second linear part of the bilinear tensile stress-strain curve is used where the modulus of elasticity after cracking (E_{frcm}) is generally small due to the slippage of fabric within the matrix. Secondly, the controlling failure mode corresponding to the design approach is not clarified. However, despite that, ACI 549.4R (2013) provides an available design guideline in the FRCM system.

Compared with ACI 549.4R (2013), the new ready-to-be-published Italian guidelines (Ascione et al., 2018) not only consider the tensile behavior of both dry fabric mesh and FRCM composites but also the bond behavior of FRCM system to a specified substrate. Alternatively, the Young modulus of the dry fabric mesh (E_f) is utilized in the coming Italian guidelines, while the modulus of FRCM (E_{frcm}) after cracking is adopted in the ACI 549.4R (2013). However, more detailed information in the coming Italian guidelines is necessary and verified (Ascione et al., 2018), such as the evaluation of the coefficient α in Eq. (2.7).

In the case of considering the well-established bond strength model of FRP system, strictly speaking, it cannot be extended to cement-based composites since the debonding mechanisms of the polymeric resin-based FRP composite is different from that of the cement-based FRCM composite. When FRP is bonded to concrete, the debonding typically occurs in a thin layer within the concrete. Consequently, both the mechanical properties and interfacial roughness of concrete substrate have a fundamental role in the bond behavior. While for concrete externally bonded FRCM composite using a cementitious adhesive, the debonding generally occurs at the fabric-matrix interface in the FRCM composite.

Lastly, the prediction formulas for the debonding strain of FRCM composite based on the experimental bond tests are useful in the FRCM system. However, the reliability of the proposed formulas is sensitive to the different bond test setups. Regarding the prediction formulas for the debonding strain of FRCM composite based on the experimental flexural tests (Bencardino et al. 2018), it is only useful for S-FRCM strengthening that is a relatively smaller application than carbon-FRCM and PBO-FRCM. Moreover, the formulas only consider the mechanical properties of dry fabric mesh and do not consider explicitly the bond properties of the fabric-matrix interface.

However, only the debonding failure mode, involving the fabric-matrix and matrix-substrate interface plane, was considered in the available prediction approaches. The fabric slippage failure within the matrix in the FRCM composite should be investigated and analyzed. The prediction formulas of flexural load-carrying capacity for RC beams with externally bonded carbon-FRCM considering slippage of fabric are introduced in this chapter.

2.3 Experimental program

2.3.1 Carbon-FRCM composites

Carbon fabric (CF) mesh

Fig. 2.6 shows the bidirectional carbon fabric (CF) mesh used to make up the carbon-FRCM composites, in which there are 100 bundles of carbon fiber in the primary direction and 130 bundles in the secondary direction per unit of meter. The nominal number of carbon filaments is 12,000 in a piece of fiber bundle for both directions, and each filament has a nominal diameter of 7 μm. Table 2.1 gives the tensile properties of the carbon fiber filament from the manufacturer and the tested tensile properties of the dry (non-impregnated) carbon fiber bundle in which the fiber filaments are individually coated but are not bonded. The tensile tests of dry carbon fiber bundles are refereed to ASTM D4018 (1999). Three carbon fiber bundles were involved in the tensile loading. The extensometer with the gauge length of 50 mm was used to measure the deformation of carbon fiber bundles, as shown in Fig 2.7. Six repeated specimens were tested. The tensile strength, tensile modulus, and tensile strain to failure were 2125 MPa, 196.4 GPa, and 1.1%, respectively. The differences in the tensile strength between a piece of fiber filament provided by the manufacture and test results of fiber bundles might be due to the substantial probability of flaws on the carbon fiber filaments, and the non-uniform tensile stress distribution occurred in the tensile tests of bundles.

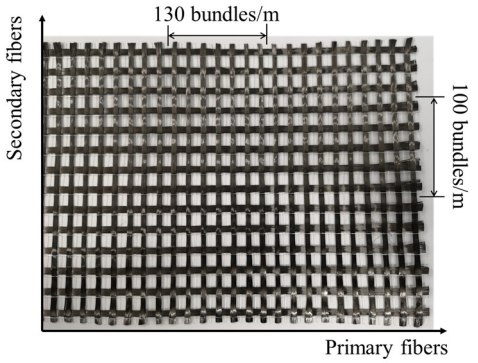

Fig. 2.6 Carbon fabric mesh for making carbon-FRCM composites.

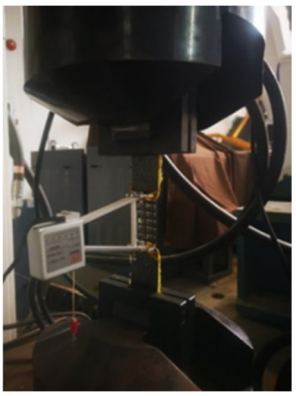

Fig. 2.7 Tensile tests of dry carbon fiber bundles.

Table 2.1 Tensile properties of carbon fibers.

Carbon fibers	Tensile strength, f_f [1], f_{cf} [2] (MPa)	Elastic modulus, E_f [1], E_{cf} [2] (GPa)	Strain-to-failure, ε_f [1], ε_{cf} [2] (%)	Cross-sectional area, A_f [1], A_{cf} [2] (mm^2)
Fiber filament [1]	4900	230.0	2.1	3.85×10^{-5}
Fiber bundle [2]	2125	196.4	1.1	0.462

Note: [1] represents the tensile properties of the carbon fiber filament provided by the manufacturer; [2] represents the tensile properties of the dry carbon fiber bundle obtained from the tensile tests conducted by the author.

Cement-based mortar matrix

A cement-based mortar matrix composition for carbon-FRCM composites is shown in Table 2.2. The binder is Portland cement type 52.5 R, and the water-to-cement ratio is 0.35. Quartz sand with different particle sizes is used; the fine sand size ranges from 0.1 mm to 0.5 mm, and the moderate sand size is smaller than 1.0 mm. The weight ratio between fine and moderate sand is 0.5. The mortar contains 0.75 wt. % (measured as a percent of the weight of cement) short, dispersed carbon fibers with a nominal length of 3 mm and a diameter of 7 μm. Adequate workability was obtained using a small amount of superplasticizer. The measured average flexural strength and compressive strength of the mortar after curing for 28 days were 9.3 MPa and 71.5 MPa, respectively; these values were measured per BS EN 196 (1995), as shown in Fig. 2.8.

Table 2.2 Cement-based mortar composition (unit: kg/m^3).

Cement	Water	Quartz sand		Superplasticizer	Short carbon fibers
		Fine sand size	Moderate sand size		
851	298	284	567	0.85	6.38

(a) Flexural strength testing

(b) Compressive strength testing

Fig. 2.8 Test methods for the mechanical properties of the mortar matrix.

Carbon-FRCM specimens for tensile tests

The specified size carbon-FRCM specimens used for the tensile tests are cut from large size carbon-FRCM panels. All panels are square with an edge length of 650 mm. The thickness of the panel depends on the number of layers of CF mesh: 10 mm for one layer, 15 mm for two layers, and 25 mm for four layers. The fabric reinforcement ratio (ρ_{cf}) is the cross-sectional area of the CF mesh (A_{cf}) in the carbon-FRCM divided by the cross-sectional area of the composite matrix (A_{FRCM}), as shown in Eq. (2.16). The ρ_{cf} for one-, two- and four-layer carbon-FRCM are 0.462%, 0.615% and 0.739%, respectively. A schematic example of the preparation of two-layer carbon-FRCM panels is shown in Fig. 2.9. At first, put the ready-mixed mortar into the bottom of the wooden mould with the thickness of about 5 mm; and then, align the ready-cut CF mesh onto the matrix and impregnate with mortar matrix; after that, cast the mortar with the thickness of 5 mm again covering the mesh. This procedure should be repeated if more than one layer of CF mesh is embedded into the carbon-FRCM composite.

$$\rho_{cf} = A_{cf} / A_{FRCM} \quad \text{……(2.16)}$$

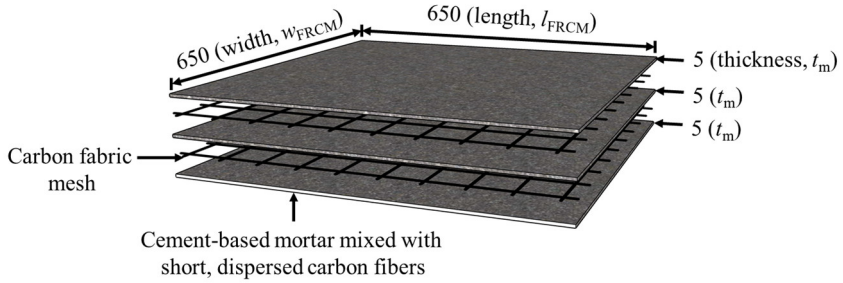

Fig. 2.9 Preparation of carbon-FRCM panels (w_{FRCM} = width of FRCM panel; l_{FRCM} = length of FRCM panel; t_m = thickness of each layer of cementitious mortar matrix. units: mm).

The carbon-FRCM specimens for tensile tests were trimmed from the large size square carbon-FRCM panels. The dimensions of the carbon-FRCM specimens for the tensile tests were designed per ICC-ES AC434 (2016). Firstly, a 25-mm strip around the edge of each carbon-FRCM panel (650 mm × 650 mm) should be removed with a cutting machine. Subsequently, carbon-FRCM specimens with a nominal dimension of 600 mm × 100 mm were obtained from the trimmed panel (600 mm × 600 mm), as shown in Fig. 2.10. After that, metallic tabs with a thickness of 2 mm and a bond length of 200 mm were bonded to both ends of the carbon-FRCM specimen with a polymeric resin. The middle region of the specimen, which was 200 mm in length, was tested. Finally, the carbon-FRCM specimen with metallic tabs, as shown in Fig. 2.10, can be used to perform the tensile tests after the resin solidifies for more than 2 days.

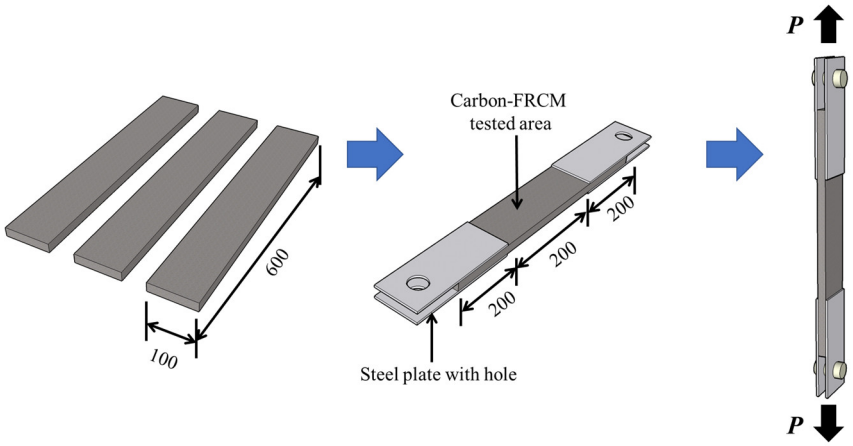

Fig. 2.10 Preparation of carbon-FRCM specimens for tensile tests.

Carbon-FRCM plates for strengthening beams

The specified carbon-FRCM plates used for externally bonding to the soffit of beams are also cut from large size carbon-FRCM panels, as shown in Fig. 2.11. All panels are rectangular with a length of 1150 mm and a width of 730 mm. The thickness of the panel is 10 mm for one-layer, 15 mm for two-layer, and 25 mm for four-layer carbon-FRCM. The procedure for casting the carbon-FRCM panels is identical to the preparation of carbon-FRCM panels for tensile tests mentioned above.

Fig. 2.11 Large size carbon-FRCM panels in structural strengthening program.

The carbon-FRCM plates for strengthening beams were trimmed from the large size rectangular carbon-FRCM panels. Firstly, a 25-mm strip around the edge of each carbon-FRCM panel (1150 mm × 730 mm) should be removed with a cutting machine. And then, carbon-FRCM plates with a nominal dimension of 1100 mm × 170 mm were obtained from the trimmed panel (1100 mm × 680 mm), as shown in Fig. 2.12. The width between the carbon-FRCM plates and beams is identical.

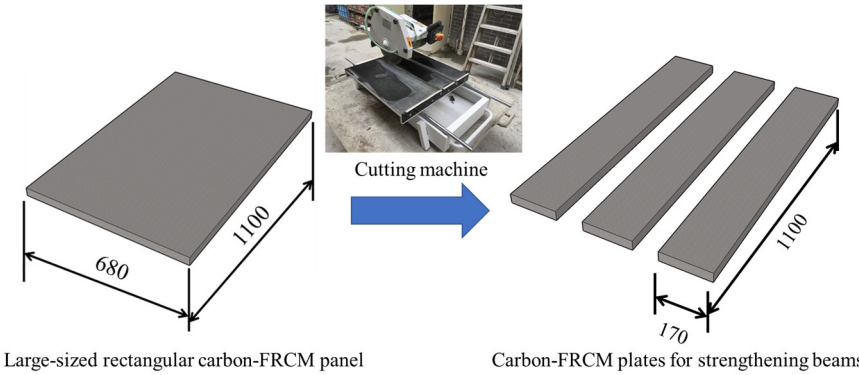

Fig. 2.12 Preparation of carbon-FRCM plates for externally bonding to the soffit of RC beams.

2.3.2 Reinforced concrete beams

Preparation of beams

Table 2.3 shows the concrete composition, for each cubic meter volume, the weight of cement is 390 kg, river sand is 652 kg, coarse aggregate is 977 kg, and water is 187 kg that results in the water-to-cement ratio is 0.48. A small amount of superplasticizer was used to improve the workability of the concrete mixture. Note that 3% sodium chloride (NaCl) salt (by the weight of cement) was dissolved into the water for mixing concrete. At the time of casting concrete, three standard concrete cubes with dimensions of 150 mm were prepared for obtaining the compressive strength of concrete. After 28-days of curing, the tested average cubic compressive strength (f_{cu}) was 42.2 MPa with a standard deviation of 1.8 MPa.

Table 2.3 Concrete composition (unit: kg/m^3).

Cement	Water	River sand	Coarse aggregate	Superplasticizer	NaCl salt
390	187	652	977	0.5	11.7

Fig. 2.13 shows the schematic diagram of reinforced concrete (RC) beams in which the geometric dimensions are 1500 mm in length, 170 mm in width, and 300 mm in height. Two

deformed steel rebars with a diameter of 12 mm are placed at the tension zone of the beam, while two round steel rebars with a diameter of 8 mm are placed at the compression zone. The same round steel rebars are used as stirrups as well, which are placed at the interval of 80 mm in both sides of the beam except the intermediate zone of 400 mm. The thickness of the concrete cover is 30 mm from the surrounding surface of the beam to the outer surface of the stirrup. The total RC beams were curing atmospherically outside of the laboratory, as shown in Fig. 2.14. Table 2.4 summaries the mechanical properties of deformed and round steel rebars embedded into the concrete.

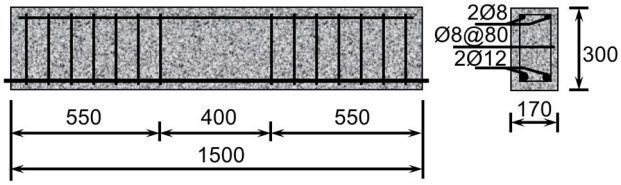

Fig. 2.13 Schematic diagram of reinforced concrete beams.

Fig. 2.14 RC beams curing outside atmospherically.

Table 2.4 Mechanical properties of steel rebars embedded into concrete.

Type	Nominal diameter, ϕ (mm)	Yielding strength, f_{sy} (MPa)	Tensile strength, f_{su} (MPa)	Modulus of elasticity, E_s (GPa)	Yielding strain, ε_{sy} (%)	Tensile strain, ε_{su} (%)
Tension steel	12	496.7	601.3	200	0.25	9.3
Compression steel / stirrup	8	340.0	544.0	200	0.17	13

RC beams strengthened with carbon-FRCM

The carbon-FRCM plates were externally bonded to the soffit of beams, as shown in Fig. 2.15. The beams were inversed to make the soffit to an upturn in order to bond the carbon-FRCM plates easily. The soffit was sandblasted, and then both the beams and carbon-FRCM plates were wet but without apparent water before bonding. The same cement-based mortar was used as adhesive material with a thickness of 5 mm. The bond length was 1100 mm in the middle of beams. The strengthened beams were cured more than 28 days before the final four-point bending tests.

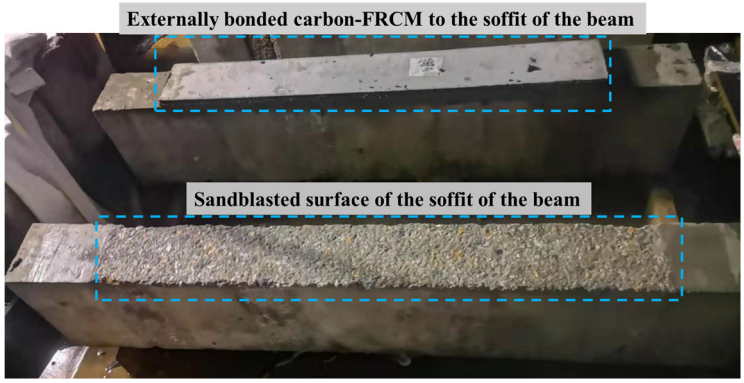

Fig. 2.15 RC beams externally strengthened with carbon-FRCM plates.

2.3.3 Static tensile tests of M/C-FRCM

Fig. 2.16 shows the tensile tests setup of carbon-FRCM specimens that is referred to the test method recommended in the ICC-ES AC434 (2016), in which clevis grips are used to connect the carbon-FRCM specimen and the loading heads. A test frame with a maximum capacity of 50 kN is used to perform the tensile loads. Two clip-on extensometers with gauge lengths of 200 mm are placed at the middle of the specimen on two sides to measure the deformation of the carbon-FRCM during tensile loading, as shown in Fig. 2.16. The global deformation measurements permit us to account for all the cracks developed and propagated along with the carbon-FRCM specimens.

Fig. 2.16 Tensile tests setup of carbon-FRCM specimens.

The static tensile loading was performed by the displacement control at a constant rate of 0.20 mm/min. Recording the tensile load, deformations of the carbon-FRCM specimen until tensile failure. Data acquisition was performed at a frequency of 5Hz. Table 2.5 gives the overall information of the carbon-FRCM specimens used in the static tensile tests. A total of 9 multilayer carbon-FRCM (M/C-FRCM) specimens were prepared. Three repeated specimens were used for each type of carbon-FRCM. The labeling of the carbon-FRCM specimens was termed starting with S-T (static tensile loading), followed by the number of layers of CF mesh (i.e., L1, L2, and L4).

Table 2.5 M/C-FRCM specimens in the static tensile tests.

Carbon-FRCM specimens	Layer of CF mesh	Size of carbon-FRCM	Number of repeated specimens
S-T-L1	1	600×100×10	3
S-T-L2	2	600×100×15	3
S-T-L4	4	600×100×25	3

2.3.4 Static bending tests of RC beams with externally bonded M/C-FRCM

Fig. 2.17 shows the four-point bending tests setup of beam specimens. A hydraulic servo system was used to apply the loads to the beam through a spreader beam. The applied load was recorded by a load cell placed between the hydraulic loading head and the spreader beam. Fig. 2.18 presents the detailed information of four-point bending tests of carbon-FRCM-strengthened beams. The clear span of the beam is 1200 mm between two supports, and the shear span is 400 mm between one of the loading points to the nearest support. The stirrups are used in the region of the shear span to prevent shear failure. The pure bending area of 400 mm is left in the middle of the beam. In the process of loading, deflections at the midspan and the two corresponding loading points of the beam are measured using a linear variable differential transformer (LVDT). Two strain gauges with a gauge length of 50 mm are attached to the top of the concrete beam at midspan on both sides; six strain gauges with a gauge length of 5 mm are attached to the two steel rebars in tension. It is important to note that two clip-on extensometers with the gauge length of 200 mm are used to measure the deformations of the carbon-FRCM plate. The extensometers are set in the middle of the carbon-FRCM plate on both sides.

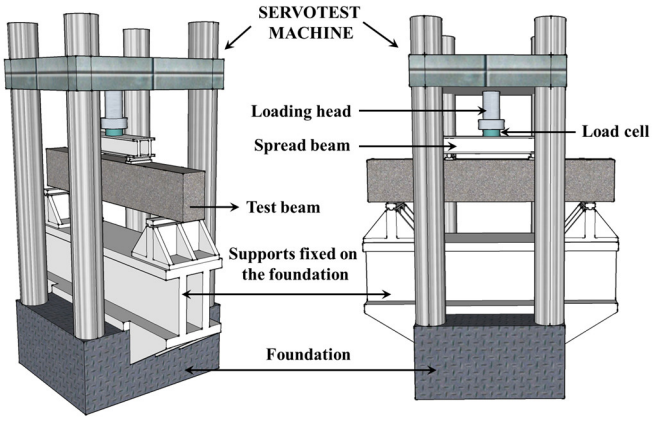

Fig. 2.17 Four-point bending tests setup of beam specimens.

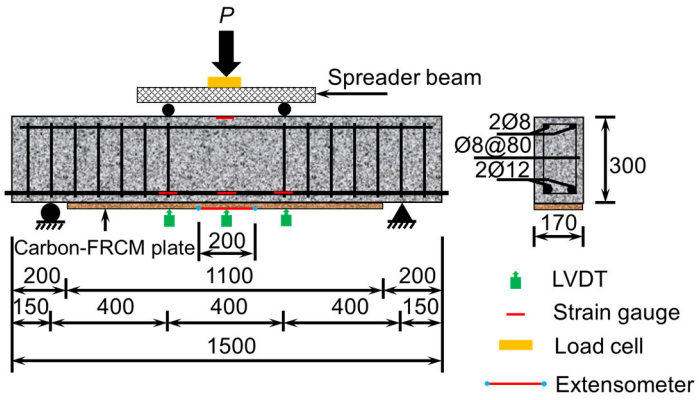

Fig. 2.18 Detailed information on four-point bending tests of beams with externally bonded carbon-FRCM.

The static bending tests were performed by the displacement control at a constant rate of 0.5 mm/min. Recording the load, deflections of beams, strains of concrete at the top of the beam and strains of steel rebars, and the deformations of the carbon-FRCM plate. Data acquisition was performed at a frequency of 5Hz. Table 2.6 gives the overall information of beams with externally bonded M/C-FRCM in the static bending tests. A total of 4 beams were prepared. The labeling of beams was termed starting with S-B (static bending loads), followed by the number of layers of CF mesh (i.e., L0, L1, L2, and L4) in the carbon-FRCM plate.

Table 2.6 RC beams strengthened with M/C-FRCM in the static bending tests.

Beams	Layer of CF mesh	Size of carbon-FRCM
S-B-L0	0	/
S-B-L1	1	1100×100×10
S-B-L2	2	1100×100×15
S-B-L4	4	1100×100×25

2.4 Tensile test results and discussion

2.4.1 Load-deformation and failure modes

The tensile load-deformation behaviors of the tested carbon-FRCM specimens are shown in Fig. 2.19. Table 2.7 summarizes the measured experimental tensile load and deformation values at the occurrence of the first crack on the mortar matrix and ultimate load and deformation. The pre-cracking and post-cracking tensile stiffness are also involved. The pre-cracking tensile stiffness represents the slope of the load-deformation curve between the initial zero loads and cracking load, while the post-cracking tensile stiffness represents the slope of the load-deformation curve between cracking and ultimate capacity.

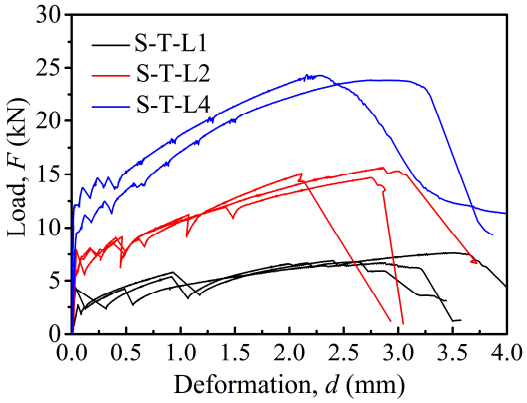

Fig. 2.19 Tensile load vs. deformation of M/C-FRCM specimens.

Table 2.7 Experimental results of M/C-FRCM specimens under static tensile loading.

Carbon-FRCM specimens	F_{cr_frcm} (kN)	d_{cr_frcm} (mm)	k_{cr_frcm} (kN/mm)	F_{u_frcm} (kN)	d_{u_frcm} (mm)	k_{u_frcm} (kN/mm)
S-T-L1-1	2.696	0.058	46	6.714	2.854	1.437
S-T-L1-2	4.264	0.032	133	6.806	2.614	0.985
S-T-L1-3	4.530	0.028	162	7.632	3.416	0.916
Average	3.830	0.039	114	7.051	2.961	1.112
Cov	0.259	0.414	0.527	0.072	0.139	0.255
S-T-L2-1	6.119	0.028	219	15.656	2.862	3.365
S-T-L2-2	6.168	0.060	103	14.680	2.754	3.160
S-T-L2-3	7.929	0.042	189	15.080	2.114	3.451
Average	6.739	0.043	170	15.139	2.577	3.325
Cov	0.153	0.370	0.353	0.032	0.157	0.045
S-T-L4-1	12.379	0.072	172	24.356	2.166	5.720
S-T-L4-2	9.967	0.082	122	23.866	2.750	5.210
Average	11.173	0.077	146	24.111	2.458	5.465
Cov	0.153	0.092	0.243	0.014	0.168	0.066

Note: F_{cr_frcm} = Load at the occurrence of the first crack on the mortar matrix; d_{cr_frcm} = Deformation corresponding to F_{cr_frcm}; k_{cr_frcm} = Pre-cracking stiffness; F_{u_frcm} = Ultimate load; d_{u_frcm} = Ultimate deformation; k_{u_frcm} = Post-cracking stiffness.

The load-deformation can be modeled as a bi-linear behavior representing the uncracked and cracked zones. In the uncracked zone, the carbon fabric (CF) mesh reinforcement and mortar matrix are assumed to carry the tensile load together. The average tensile cracking load was 3.83 kN, 6.74 kN, 11.17 kN in S-T-L1, S-T-L2, and S-T-L4 specimens, respectively. The large pre-cracking tensile stiffness was observed in all specimens. However, the random results were due to the sensitivity of the smaller deformation before cracking. In the cracked zone, countable cracks progressively occurred at the mortar matrix firstly, and then one of the cracks became the major crack as the width of the crack increased. After reaching the peak load, the load slightly deceased, followed by a sudden tensile failure, except for S-T-L4 specimens. The characteristics of the sudden tensile failure were:

(1) the load immediately dropped to a low value towards zero; (2) the corresponding deformation increased largely; (3) the width of the major crack became very large at that moment. Whereas, the tensile load of S-T-L4 specimens decreased and deformation increased continuously. The post-cracking tensile stiffness was 1.11 kN/mm, 3.33 kN/mm, 5.47 kN/mm that are extremely smaller than the pre-cracking tensile stiffness. The CF meshes were assumed to carry the tensile load after cracking, and the mechanism of slippage between CF meshes and mortar matrix resulted in the reduction of tensile stiffness. Fig. 2.20 shows the tensile failure modes of M/C-FRCM composites that are fabric slippage at the major crack. There were two cracks in S-T-L1, three or four cracks in S-T-L2, and four cracks in S-T-L4 specimens. The number of cracks at the mortar matrix increased as the fabric reinforcement ratios increase. The nearly intact carbon fiber bundles were observed, while a few fiber filaments rupture could also be observed at the major crack.

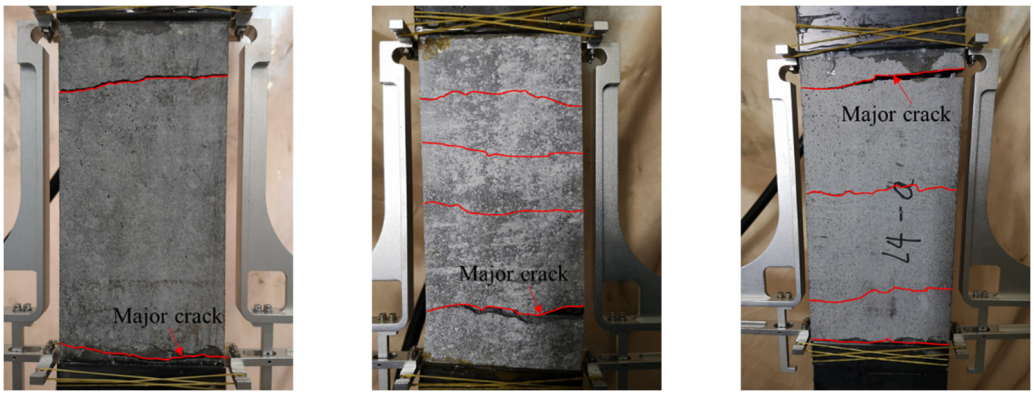

(a) S-T-L1 (b) S-T-L2 (c) S-T-L4

Fig. 2.20 Tensile failure modes of M/C-FRCM specimens.

2.4.2 Tensile stress-strain relation of M/C-FRCM

The tensile stress and strain at a specific data point are calculated using Eq. (2.17) and Eq. (2.18):

$$\sigma_i = F_i / A_{cf} \quad \text{.....(2.17)}$$

$$\varepsilon_i = d_i / L_g \quad \text{.....(2.18)}$$

Where: F_i = load at the ith data point; A_{cf} = cross-section area of fabric mesh reinforcement; d_i = extensometer displacement at the ith data point; L_g = gauge length of extensometer.

The comparison of experimental tensile stress-strain behavior of M/C-FRCM is shown in Fig. 2.21. The average maximum tensile strength was 1527.5 MPa in S-T-L1, 1639.9 MPa in S-T-L2, and 1306.0 MPa in S-T-L4 specimens. The utilization efficiency (δ_{cf}) was defined as the percentage of the tested average tensile strength of the carbon-FRCM (f_{u_frcm}) to the tensile strength of the dry carbon fiber bundle (f_{cf} = 2125 MPa), as shown in Eq. (2.19). The corresponding utilization efficiency δ_{cf} values of S-T-L1, S-T-L2, and S-T-L4 were 71.9%, 77.2%, and 61.5% of the tensile strength of the dry carbon fiber bundle, respectively. It shows that the tensile capacity of carbon fabric in carbon-FRCM composite does not be utilized thoroughly. This is contributed to the different loading behavior and failure modes between the dry carbon fiber bundles and carbon-FRCM composite. The failure of carbon fiber bundles was almost rupture of carbon fibers, while

the tensile failure of carbon-FRCM was the slippage of carbon fiber bundles within the mortar matrix. Besides, there were 20 fiber bundles in the S-T-L2 specimen, which might not be under uniform stress distribution, especially after the cracking of the mortar matrix. Whereas for dry carbon fiber, 3 bundles were loaded more evenly. Moreover, the ultimate tensile strain of M/C-FRCM was higher than that of dry carbon fiber bundles because of the slippage of fiber bundles within the mortar matrix.

$$\delta_{cf} = \frac{f_{u\_frcm}}{f_{cf}} \qquad \text{.....(2.19)}$$

Where: δ_{cf} = utilization efficiency of carbon fabric in the carbon-FRCM composite; f_{u_frcm} = tested average tensile strength of carbon-FRCM; f_{cf} = tensile strength of dry carbon fiber bundle.

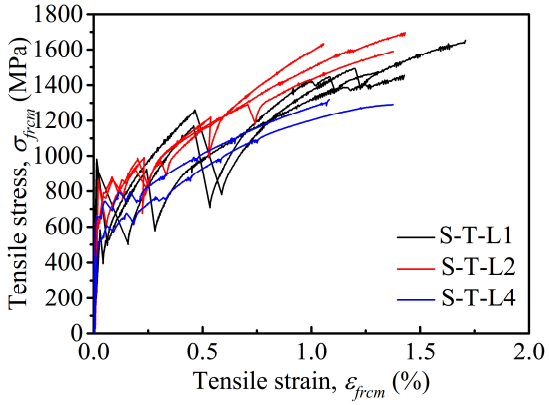

Fig. 2.21 Experimental tensile stress-strain relation of M/C-FRCM specimens.

Unlike FRP material, the characteristic of cracking of FRCM composites under tension loads results in complicated tensile stress-strain behavior. The guideline AC434 (2016) provides a series of calculation processes to simplify and clarify the bi-linear tensile behavior of FRCM composites. Appendix A.1 presents a detailed calculation process for the tensile modulus of elasticity of the uncracked (E_{frcm}^{*}) and cracked specimen (E_{frcm}), ultimate tensile stress (f_{u_frcm}) and tensile strain (ε_{u_frcm}). The comparison of experimental and calculated tensile stress-strain of M/C-FRCM specimens are presented in Appendix A.2. Table 2.8 shows the detailed calculated data of M/C-FRCM. Accordingly, the comparison of the constitutive behavior of carbon-FRCM is shown in Fig. 2.22. The average modulus of elasticity in the post-cracking stage was 58.8 GPa in S-T-L1, 74.0 GPa in S-T-L2, and 63.6 GPa in S-T-L4 specimens. The ultimate tensile strain of carbon-FRCM decreased from 1.34% in S-T-L1 to 1.19% in S-T-L2 and 1.06% in S-T-L4. The explanation is that more carbon fabric mesh mitigated the slippage of fiber bundles within the mortar matrix. Consequently, the two-layer carbon-FRCM has a superior constitutive property of higher tensile strength and cracked tensile modulus of elasticity, and relative higher tensile strain. The higher utilization efficiency δ_{cf} of 77.2% indicated that two-layer of carbon fabric mesh was an optimized selection in the design of multilayer carbon-FRCM.

Table 2.8 Tensile properties of M/C-FRCM based on the guideline AC434 (2016).

Carbon-FRCM Specimen	σ_{cr_frcm} (MPa)	ε_{cr_frcm} (%)	E_{frcm}^{*} (GPa)	σ_{u_frcm} (MPa)	ε_{u_frcm} (%)	E_{frcm} (GPa)
S-T-L1-1	769.7	0.037	2088.4	1454.6	1.244	56.7
S-T-L1-2	690.3	0.012	5762.1	1474.5	1.079	73.5
S-T-L1-3	873.8	0.013	6885.9	1653.4	1.699	46.2
Mean	777.9	0.021	4912.1	1527.5	1.341	58.8
Cov	0.118	0.685	0.511	0.072	0.240	0.234
S-T-L2-1	738.9	0.016	1690.0	1696	1.273	76.1
S-T-L2-2	783.5	0.035	2215.8	1590.1	1.237	67.1
S-T-L2-3	812.5	0.013	6330.9	1633.5	1.055	78.7
Mean	778.3	0.021	3412.2	1639.9	1.188	74.0
Cov	0.048	0.560	0.745	0.032	0.098	0.082
S-T-L4-1	747	0.04	1878.1	1319.2	1.033	57.6
S-T-L4-2	564.4	0.038	1481.5	1292.7	1.084	69.6
Mean	655.7	0.039	1679.8	1306.0	1.059	63.6
Cov	0.197	0.036	0.167	0.0143	0.034	0.133

Note: σ_{cr_frcm} = cracking stress; ε_{cr_frcm} = cracking strain; E_{frcm}^{*} = modulus of elasticity of uncracked carbon-FRCM; σ_{u_frcm} = ultimate stress; ε_{u_frcm} = ultimate strain; E_{frcm} = modulus of elasticity of cracked carbon-FRCM.

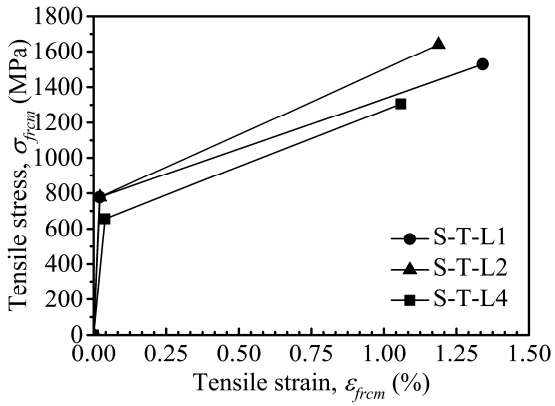

Fig. 2.22 Calculated tensile stress-strain relation of M/C-FRCM composites.

2.4.3 Apparent strain of CF mesh in M/C-FRCM

It is noted that the characteristic of fabric slippage within the mortar matrix is a unique behavior of the FRCM composite under tension; the dry fabric mesh is embedded into the matrix. The slippage behavior results in the ambiguous deformation of carbon-FRCM involving the deformation of CF mesh itself and the displacement between CF mesh and mortar matrix. The tensile strain of carbon-FRCM (ε_{frcm}) is calculated as Eq. (2.18) in which the δ_i is the displacement of extensometer, and L_g is the gauge length of the extensometer. However, ε_{frcm} is not the activated strain of CF mesh in the mortar matrix due to the measured δ_i involving the displacement of CF mesh and matrix. The

strain of CF mesh should be the deformation of CF mesh within a specified gauge length. It is rather difficult to measure the deformation and displacement of CF mesh separately. Thus, a regression model of the apparent strain of CF mesh ($\varepsilon_{ap,f}$) based on the measured global strain of carbon-FRCM (ε_{frcm}) was proposed in this section.

In the tensile tests of carbon-FRCM composites, it is assumed that the strain of CF mesh is identical to the strain of carbon-FRCM before cracking of mortar matrix. After cracking, the CF mesh is the dominant load carrying component of the carbon-FRCM under tension. The deformation of CF mesh is concentrated at the region of the crack where the CF mesh is exposed to the outside. Therefore, the apparent strain of CF mesh ($\varepsilon_{ap,f}$) is defined as the strain as all the force (F) is carried by CF mesh (i.e., the Young modulus of CF is E_f) with the total cross-section area (A_f), which is followed by the Eq. (2.20).

$$\varepsilon_{ap,f} = \frac{F}{A_f E_f} \qquad \text{.....(2.20)}$$

Where F is the tensile loads, A_f is the cross-section area of dry CF mesh, E_f is the Young modulus of dry CF mesh.

Meanwhile, the displacement of CF mesh is predominant in the mortar matrix within the gauge length of the extensometer after cracking of mortar matrix. A regression fitting was performed to obtain the apparent strain ($\varepsilon_{ap,f}$) of CF mesh based on the measured global strain of carbon-FRCM (ε_{frcm}) in the form of a logarithm like Eq. (2.21). The fitting process is presented in Appendix A.3. Table 2.9 shows the fitting parameters α, β, γ between $\varepsilon_{ap,f}$ and ε_{frcm}. It should be noted that the apparent strain of CF ($\varepsilon_{ap,f}$) is limited by the ultimate strain of FRCM (ε_{frcmu}).

$$\varepsilon_{ap,f} = \alpha \ln\left(\varepsilon_{frcm} + \beta\right) + \gamma \qquad \text{.....(2.21)}$$

Table 2.9 Fitting parameters between the apparent strain of CF mesh and measured global strain of carbon-FRCM.

Specimens	α	β	γ
S-T-L1	0.196	0.034	0.671
S-T-L2	0.158	0.011	0.728
S-T-L4	0.137	0.013	0.608

Fig. 2.23 shows the comparison of the apparent strain of CF mesh in M/C-FRCM composites against the measured global strain of carbon-FRCM specimens. The $\varepsilon_{ap,f}$ increased over the ε_{frcm} at the beginning of tension because the exposed CF mesh at the region of the crack sustained the tensile force to compensate for the cracking of matrix. The slippage was not significant since the CF mesh within the mortar matrix was much restrained. As the tensile force increased further, the slippage of CF mesh was superior, growing $\varepsilon_{ap,f}$ was inferior to the growth of ε_{frcm}. Fig. 2.23 shows that the apparent strain of CF mesh ranged from 0.006 to 0.008 at the tensile failure of M/C-FRCM. With regarding to the tensile strength of dry carbon fiber bundles, the utilization efficiency of fibers was around 70% on average, where the lower was 62% in the four-layer carbon-FRCM, and higher was up to 76% in the two-layer carbon-FRCM. It was also proven that the two-layer of CF mesh was an

optimized selection in the design of multilayer carbon-FRCM composites.

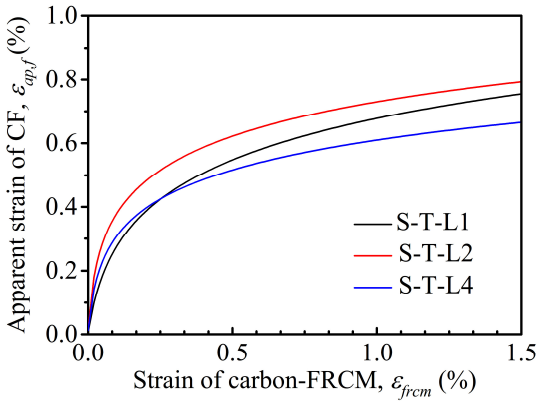

Fig. 2.23 Comparison of the apparent strain of CF mesh in M/C-FRCM composites.

2.5 Bending test results and discussion

2.5.1 Failure modes

Fig. 2.24 shows the failure modes of the control beam without strengthening and beams with externally bonded M/C-FRCM. The yielding of steel rebars was observed in all beam specimens. Conventionally, the failure mode of the S-B-L0 beam was the yielding of steel rebars followed by the concrete crushing at the extreme compression zone (CC), as shown in Fig. 2.24(a). Regarding the strengthened beams, S-B-L1 and S-B-L2 beams had the same failure mode that was the slippage of CF mesh within the mortar matrix in the carbon-FRCM followed by the concrete crushing at the extreme compression zone (FS+CC) as shown in Fig. 2.24(b) and (c). As increasing the applied load, a critical crack was observed to progressively propagate from the carbon-FRCM plate to the top of concrete in the pure bending zone of the beam. The gradual increase of the width of cracks at the carbon-FRCM was observed as well before the flexural failure. Whereas increasing the number of layers of CF mesh, the failure mode of the S-B-L4 beam changed to the debonding at the matrix-concrete interface starting from the cut-off end of the carbon-FRCM plate followed by the peeling-off of concrete cover (D+PO) as shown in Fig. 2.24(d). The fracture of concrete at the top extreme side was not observed. A sudden failure phenomenon occurred in the S-B-L4 beam due to the intense peeling-off of concrete cover.

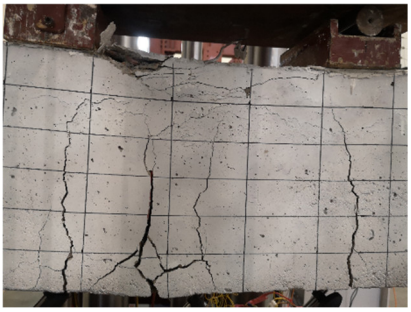

(a) S-B-L0 (CC)

(b) S-B-L1 (FS+CC)

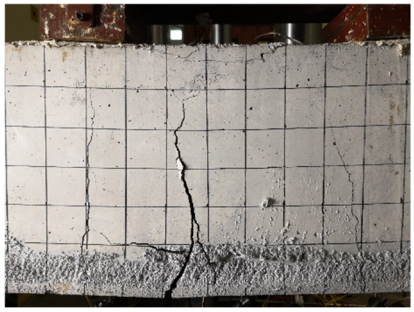

(c) S-B-L2 (FS+CC)

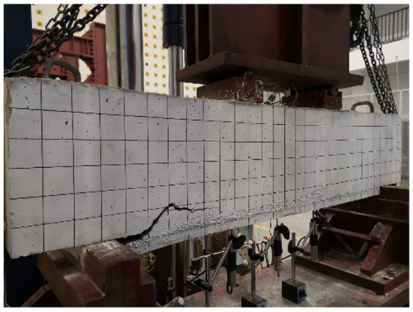

(d) S-B-L4 (D+PO)

Fig. 2.24 Failure modes of RC beams.

2.5.2 Load-deflection behavior

The load-deflection curves of the tested beams are shown in Fig. 2.25. Table 2.10 summarizes the measured experimental load and deflection values at cracking of the concrete, yielding of steel rebars, ultimate load, and deflection. The experimental load and deflection at the fabric slippage (FS) failure are also included in Table 2.10. The FS failure is distinguished from the ultimate FS+CC failure mode. The FS failure is defined as a specified loading state where the applied load dropped suddenly to some extent after the yielding of steel rebars as a consequence of significant loss of FRCM composite action. However, the FRCM still reserved the effect of strengthening due to the residual composite action at the fabric-matrix and matrix-concrete interface. Table 2.10 also shows the ductility indexes, gains in the load capacity of the strengthened beams compared to the control beam.

The load-deflection curves of each beam can be modeled as a tri-linear behavior representing uncracked stage, post-cracking stage, and post-yielding stage. The yielding load and ultimate capacity, as well as the load at the FS failure, are highlighted in Fig. 2.25. Compared with the S-B-L0 beam, the ultimate capacity of strengthened beams increased, while the corresponding deflection decreased as the increase of layers of CF mesh. Except for the S-B-L4 beam, the phenomenon of excessive slippage of fabric was observed in both S-B-L1 and S-B-L2 beams where the fabric slippage within the mortar matrix along with the full flexural crack was found. The load increased gradually after the sudden drop caused by the excessive slippage of fabric until concrete crushing.

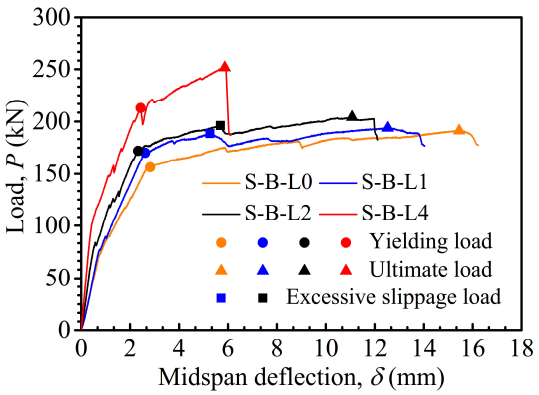

Fig. 2.25 Load-deflection curves of RC beams.

Table 2.10 Summary of static bending test results of beams with externally bonded M/C-FRCM.

Beams	P_c (kN)	P_y (kN)	P_{fs} (kN)	P_u (kN)	δ_y (mm)	δ_{fs} (mm)	δ_u (mm)	δ_u / δ_y	Loss in ρ (%)	Gain in P_y (%)	Gain in P_u (%)	FRCM failure mode	Ultimate failure mode
S-B-L0	68.30	156.31	/	191.15	2.82	/	15.45	5.48	/	/	/	/	CC
S-B-L1	77.21	170.19	188.38	193.72	2.62	5.27	12.53	4.78	12.77	8.88	1.34	FS	FS+CC
S-B-L2	84.07	172.12	196.12	204.02	2.33	5.69	11.07	4.75	13.32	10.11	6.73	FS	FS+CC
S-B-L4	102.81	212.78	/	251.60	2.43	/	5.87	2.42	55.84	36.13	31.62	D+PO	D+PO

Note: P_c = load capacity at the cracking of concrete; P_y and δ_y = load capacity and mid-span deflection at the yielding of steel rebars in tension; P_{fs} and δ_{fs} = load capacity and mid-span deflection at the fabric slippage leading to the sudden drop of the load; P_u and δ_u = load capacity and mid-span deflection at the ultimate state; δ_u / δ_y = ductility index at the ultimate state; Loss in $\rho = (\delta_{unstr} - \delta_{str}) / \delta_{unstr}$; Gain in $P_y = ((P_y)_{str} - (P_y)_{unstr}) / (P_y)_{unstr}$; Gain in $P_u = ((P_u)_{str} - (P_u)_{unstr}) / (P_u)_{unstr}$; CC = concrete crush at the compression zone; FS = fabric slippage within mortar matrix; D = FRCM debonding at the matrix-concrete interface; PO = peeling-off of the concrete cover.

Fig. 2.26 compares the gain in load capacity and loss in ductility of RC beams with externally bonded M/C-FRCM with regarding the S-B-L0 beam. The gain in the yielding load was 8.88% and 10.11% for the S-B-L1 and S-B-L2 beams, respectively. The gain in the yielding load increased to 36.13% in the S-B-L4 beam. However, the gain in the ultimate load was only 1.34% in the S-B-L1 beam and increased to 6.73% in the S-B-L2 beam. This was due to the insufficient amount of CF mesh for strengthening. When the four-layer carbon-FRCM composite was used, the gain in the ultimate capacity increased to 31.62% that was moderate because a design limitation of the FRCM contribution to flexural strength is recommended not exceed 50% of the existing flexural capacity of the structures without strengthening (ACI 549.4R, 2013). Except for the gain in load capacity, the performance of ductility is also an important factor in the design procedure. The ductility of all strengthened beams was lower than that of the control beam. The loss of ductility was 12.77% and 13.32% for the S-B-L1 and S-B-L2 beams making the remaining ductility still acceptable. However, the loss of ductility increased to 55.84% in the S-B-L4 beam due to a premature failure mode of D+PO. According to the studies of FRP system (Dai et al., 2009; Li et al., 2013), it could be considered that using efficient U-shaped reinforcement at both ends of strengthening to avoid such premature failure and improve the performance of ductility and possible gain in load capacity further.

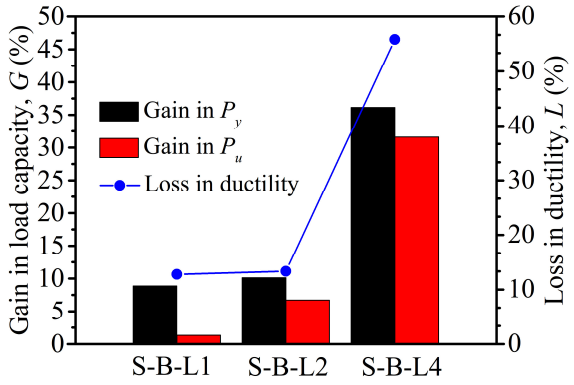

Fig. 2.26 Gain in load capacity and loss in ductility of RC beams with externally bonded M/C-FRCM.

Fig. 2.27 compares the flexural stiffness at different load-carrying stages. In the present paper, the pre-cracking, post-cracking, and post-yielding flexural stiffness represent the slopes of the load-deflection curve between zero points and cracking load, between cracking and yielding loads, and between yielding and ultimate capacity, respectively. The flexural stiffness at all three stages increased as the increase of layers of CF mesh in the carbon-FRCM. Compared with the S-B-L0 beam, although the rise of flexural stiffness was negligible in the S-B-L1 beam. This was contributed to the lower amount of CF mesh reinforcement in the carbon-FRCM and the significant slippage of CF mesh within the mortar matrix. A moderate increase of flexural stiffness was obtained in the S-B-L2 beam. The significant increase of pre-cracking stiffness in the S-B-L4 beam was due to the large thickness of four-layer carbon-FRCM, and the considerable growth of post-yielding stiffness was attributed to the less slippage of CF mesh.

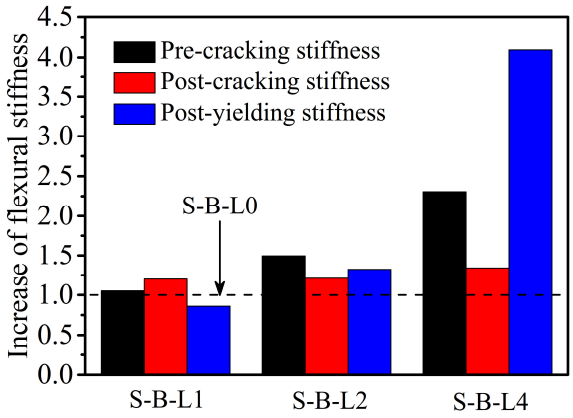

Fig. 2.27 Comparison of flexural stiffness at different load-carrying stages.

2.5.3 Behavior of externally bonded M/C-FRCM

Fig. 2.28 presents the development of a measured global strain of carbon-FRCM plate at different load-carrying stages. The strain of carbon-FRCM was less than 0.1% at the concrete cracking stage in all of three strengthened beams. As the increase of loading, the strain of carbon-FRCM increased to 0.453% in the S-B-L1, to 0.346% in the S-B-L2, and 0.219% in the S-B-L4 at the stage of yielding of steel rebars. The strain at fabric slippage (FS) of the S-B-L1 and S-B-L2 was closed to the ultimate tensile strain of themselves. It was evidenced that the ultimate load-carrying capacity of the strengthened beam was obtained when the strain of carbon-FRCM was the ultimate strain in the tensile tests. After that, the slippage of fabric was dominant until the ultimate flexural load-carrying capacity with the concrete crushing at the top of the beam.

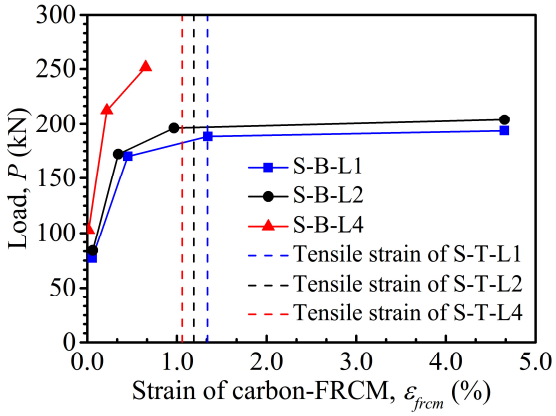

Fig. 2.28 Development of measured strain of carbon-FRCM bonded to the soffit of beams.

Fig. 2.29 presents the development of apparent strain of CF within carbon-FRCM at different load-carrying stages. The apparent strain of CF was calculated according to the Eq. (2.21). Table 2.11 shows the measured strain of carbon-FRCM and apparent strain of CF, as well as the utilization efficiency (η) of CF in tensile strain that is calculated as Eq. (2.22). The utilization efficiency of CF between S-B-L1 and S-B-L2 was almost identical at the stage of yielding of steel rebars and the FRCM failure. It indicated that the utilization efficiency of CF in S-B-L1 and S-B-L2 was rather high. The utilization efficiency η was only 50.2% in the S-B-L4 due to the premature failure mode of debonding, followed by a sudden peeling-off of the concrete cover.

$$\eta=\frac{\varepsilon_{ap,f}}{\varepsilon_{fu}}\times 100\% \quad \text{.....(2.22)}$$

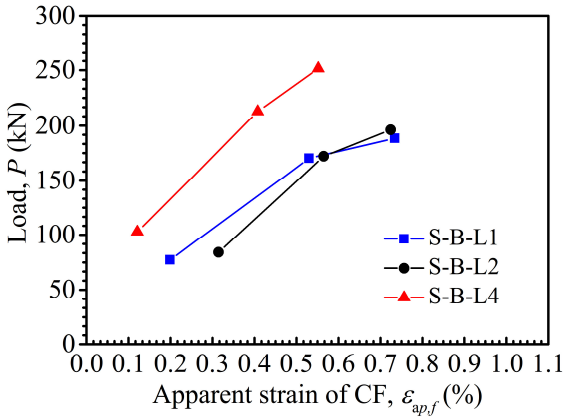

Fig. 2.29 Development of apparent strain of CF mesh in carbon-FRCM composites.

Table 2.11 Comparison of measured strain of carbon-FRCM and apparent strain of CF mesh.

Beams	Cracking of concrete			Steel yielding			FRCM failure		
	ε_{frcm_c} (%)	ε_{ap,f_c} (%)	η_c (%)	ε_{frcm_y} (%)	ε_{ap,f_y} (%)	η_y (%)	ε_{frcm_f} (%)	ε_{ap,f_f} (%)	η_f (%)
S-B-L1	0.056	0.199	18.1	0.453	0.530	48.2	1.346	0.734	66.7
S-B-L2	0.062	0.314	28.6	0.346	0.565	51.4	0.967	0.725	65.9
S-B-L4	0.016	0.121	11.0	0.219	0.408	37.1	0.652	0.552	50.2

2.6 Prediction formulas in flexure for RC beams with externally bonded carbon-FRCM

Fig. 2.30 presents a schematic diagram of the typical plane sectional analysis of a rectangular reinforced concrete cross-section with externally bonded FRCM composite at different loading states. The compatibility of strain among the concrete, steel rebars, and carbon-FRCM is considered. Four possible load-carrying capacity are discussed, including the cracking of concrete in tension, yielding of steel in tension, failure of FRCM, and crushing of concrete in compression. The corresponding control factors are the tensile strain of concrete, the yielding strain of steel rebars in tension, the effective strain of FRCM, and ultimate compressive strain of concrete.

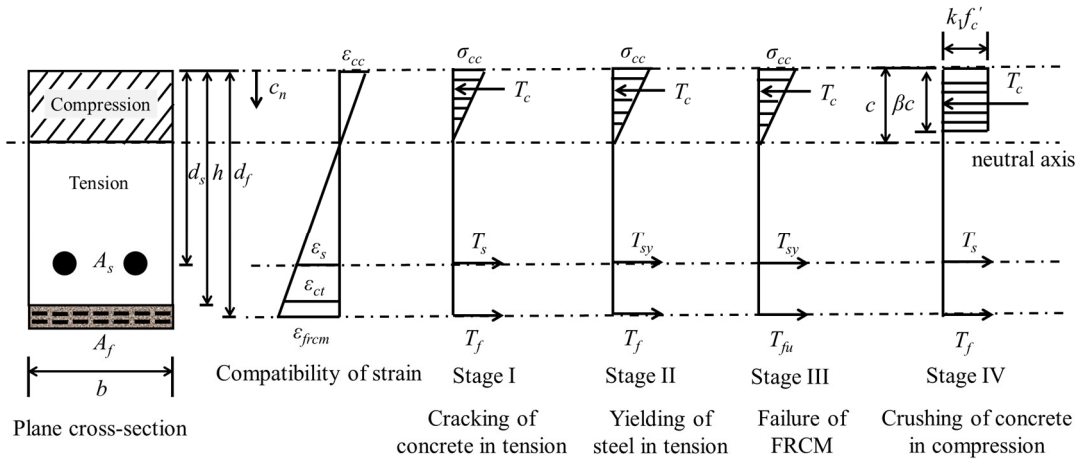

Fig. 2.30 Schematic diagram of the typical plane sectional analysis of a rectangular reinforced concrete cross-section with externally bonded carbon-FRCM composite.

Stage I – Cracking of concrete in tension

According to ACI 318 (2014), Eq. (2.23) can be used to calculate the moment of the beam when the concrete at the extreme tension side reaches its tensile strength. The FRCM-strengthened beam is made up of concrete, steel rebars, carbon fabric mesh and mortar matrix, each of which has a different modulus of elasticity. In stage I, it is assumed that all these materials behave linearly and elastically. The depth of the neutral axis (c_n) is calculated by the balance of the cross-section moment, as showing in Eq. (2.24), where the transformed area method (Toutanji and Deng., 2007) is used to convert the cross-section area of steel rebars, CF mesh, and mortar matrix into the concrete. Eq. (2.25) shows the equivalent section stiffness of each material that are derived by converting the elastic modulus of steel rebars (E_s), dry CF mesh (E_f), and mortar matrix (E_m) to the elastic modulus of concrete (E_c). Thus, the initial moment of inertia of uncracked FRCM-strengthened RC beam is calculated by Eq. (2.26).

$$M_{cr} = \frac{f_r I_0}{h - c_n} \qquad \text{……(2.23)}$$

$$c_n = \frac{\frac{1}{2}bh^2 + \alpha_s A_s d_s + \alpha_f A_f d_f + \alpha_m A_m d_m}{bh + \alpha_s A_s + \alpha_f A_f + \alpha_m A_m} \qquad \text{……(2.24)}$$

$$\alpha_s = \frac{E_s}{E_c}$$
$$\alpha_f = \frac{E_f}{E_c} \qquad \text{……(2.25)}$$
$$\alpha_m = \frac{E_m}{E_c}$$

$$I_0 = \frac{1}{3}bc_n^3 + \frac{1}{3}b(h - c_n)^3 + \alpha_s A_s (d_s - c_n)^2 + \alpha_f A_f (d_f - c_n)^2 + \alpha_m A_m (d_m - c_n)^2 \qquad \text{……(2.26)}$$

Where $f_r = 0.62\sqrt{f_c'}$, is the tensile strength of concrete; $E_c = 4700\sqrt{f_c'}$, is the elastic modulus of concrete.

Fig. 2.25 shows that the load-deflection curve of FRCM-strengthened beams can be modeled as a tri-linear behavior. Thus, a straight-line model is used to approach the load-deflection behavior, for each critical load-carrying capacity, the theoretical deflection (d) of the beam is calculated using Eq. (2.27).

$$d = \frac{Pa}{24E_cI}(3l^2 - 4a^2) \quad \text{.....(2.27)}$$

Where P is the load-carrying capacity at the different stages; $a = \frac{1}{3}l$, is the distance between one load point to the nearest support point; l is the distance between the two support points, I is the corresponding moment of inertia.

To calculate the deflection of the FRCM-strengthened beam at the stage of cracking of concrete in the extreme tension side, the Eq. (2.28) is adopted.

$$d_{cr} = \frac{P_{cr}a}{24E_cI_0}(3l^2 - 4a^2) \quad \text{.....(2.28)}$$

Stage II – Yielding of steel in tension

Stage II represents the load-deflection behavior from the cracking of concrete to the yielding of steel rebars in tension. The strain of steel rebars knows so that the strain of FRCM and concrete at the extreme compression zone are calculated based on the assumption of the plane cross-section, as described in Eq. (2.29). Comparing with the prediction approach provided by the ACI 549.4R (2013), the significant modification is that the apparent strain of CF is used to calculate the contribution of M/C-FRCM to the flexural load-carrying capacity like Eq. (2.30). The factors α, β, γ are obtained through regression in the tensile tests of carbon-FRCM, as developed in section 2.4.3. To achieve the depth of the neutral axis (c_n) by solving the internal force equilibrium as showing in Eq. (2.31). The Young modulus of dry carbon fabric (E_{cf}) is used rather than the modulus of carbon-FRCM after cracking (E_{frcm}) as per the ACI 549.4R (2013). Thus, the fabric slippage behavior in the M/C-FRCM can be characterized by using apparent strain of CF mesh ($\varepsilon_{ap,f}$). Finally, the theoretical load-carrying capacity at the yielding of steel rebars is calculated using Eq. (2.32).

$$\varepsilon_{frcm} = \frac{d_f - c_n}{d_s - c_n}\varepsilon_{sy}$$
$$\varepsilon_{cc} = \frac{c_n}{d_s - c_n}\varepsilon_{sy} \quad \text{.....(2.29)}$$

$$\varepsilon_f = \varepsilon_{ap,f} = \alpha\ln(\varepsilon_{frcm} + \beta) + \gamma \quad \text{.....(2.30)}$$

$$\frac{1}{2}bc_n\sigma_{cc} = f_{sy}A_s + E_f\varepsilon_f A_f \quad \text{.....(2.31)}$$

$$M_y = f_{sy}A_s\left(d_s - \frac{1}{3}c_n\right) + E_f\varepsilon_f A_f\left(d_f - \frac{1}{3}c_n\right) \quad \text{.....(2.32)}$$

The deflection of the FRCM-strengthened beam at the stage of yielding of steel rebars in tension will be given as Eq. (2.33).

$$d_y = \frac{P_y a}{24 E_c I_{ey}}(3l^2 - 4a^2) \quad \text{.....(2.33)}$$

Where $I_{ey} = I_{cr} + (I_0 - I_{cr})\left(\frac{M_{cr}}{M_y}\right)^c$, is the effective moment of inertia (ACI 318, 2014); c=3 for steel reinforced concrete; $I_{cr} = \frac{1}{3}bc_n^3 + \alpha_s A_s (d_s - c_n)^2 + \alpha_f A_f (d_f - c_n)^2$, is the moment of inertia of cracked FRCM-strengthened RC beams. The depth of the neutral axis at this stage is solved using $\frac{1}{2}bc_n^2 - \alpha_s A_s (d_s - c_n) - \alpha_f A_f (d_f - c_n) = 0$.

The yielding moment M_y of FRCM-strengthened RC beams is higher than that of un-strengthened RC beams. It will cause a smaller moment of inertia *Iey* when c=3 is used, which results in factor c cannot directly be used for externally strengthened beams (Toutanji and Deng., 2007). Based on the experimental results of four-point bending tests in this chapter, a new factor c =2.05 is obtained by regression analysis and is adopted in the calculation procedure.

Stage III – Failure of FRCM composites

The characteristic of stage III is that the steel rebars yields, the carbon-FRCM fails, but the concrete at the extreme compression zone does not crack. Thus, the effective apparent strain of CF at the failure of FRCM is calculated as Eq. (2.34). The effective tensile strain of FRCM at failure is evaluated as a recommendation as ACI 549.4R (2013). Then, using the effective apparent strain of CF (ε_{ff}) to assess the contribution of the carbon-FRCM to flexure. Finally, the moment of the beam with externally bonded carbon-FRCM at the FRCM failure is equal to Eq. (2.35). Similarly, the deflection at the FRCM failure will be given as Eq. (2.36). Based on the beam test results in this chapter, the factor c =4.4 should be adopted to calculate the effective moment of inertia at the post-yielding stage accounting for the FRCM failure.

$$\varepsilon_{ff} = \alpha \ln(\varepsilon_{frcme} + \beta) + \gamma$$
$$\varepsilon_{frcme} = \min\left(\varepsilon_{frcmu}, 0.012\right) \quad \text{.....(2.34)}$$

$$M_{uf} = f_{sy} A_s \left(d_s - \frac{1}{3}c_n\right) + E_f \varepsilon_{ff} A_f \left(d_f - \frac{1}{3}c_n\right) \quad \text{.....(2.35)}$$

$$d_{uf} = \frac{P_{uf} a}{24 E_c I_{euf}}(3l^2 - 4a^2) \quad \text{.....(2.36)}$$

Where $I_{euf} = I_{cr} + (I_0 - I_{cr})\left(\frac{M_{cr}}{M_{uf}}\right)^c$, is the effective moment of inertia at the post-yielding stage accounting for the FRCM failure.

Stage IV – Crushing of concrete in compression

The characteristic of the last possible stage is that the steel rebars yields followed by the crushing of concrete in compression, but the carbon-FRCM does not fail. Thus, the conventional

calculation procedure at the ultimate limit state can be adopted. The ultimate load-carrying capacity and deflection are obtained according to Eqs. (2.37) - (2.39).

$$M_{uc} = f_{sy}A_s\left(d_s - \frac{1}{2}\beta c\right) + E_f\varepsilon_f A_f\left(d_f - \frac{1}{2}\beta c\right) \quad \text{.....(2.37)}$$

$$k_1 f_c' bc = f_{sy}A_s + E_f\varepsilon_f A_f \quad \text{.....(2.38)}$$

$$d_{uc} = \frac{P_{uc}a}{24E_c I_{euc}}(3l^2 - 4a^2) \quad \text{.....(2.39)}$$

Where $I_{euc} = I_{cr} + (I_0 - I_{cr})\left(\frac{M_{cr}}{M_{uc}}\right)^c$ is the effective moment of inertia at the post-yielding stage accounting for the concrete crushing failure at the extreme compression zone.

2.7 Comparison between experimental and analytical results

Fig. 2.31 compares the experimental and analytical results of the load-carrying capacity and deflection in the load-deflection curve. The prediction formulas in the ACI 549.4R (2103) and the proposed formulas in this chapter are included. Table 2.12 and Table 2.13 present the experimental and analytical values of both the load-carrying capacity and deflection of RC beams with externally bonded M/C-FRCM where involves the yielding of steel rebars (i.e., stage II) and failure of FRCM (i.e., stage III). Results show that the experimental and analytical results compared well; moreover, the proposed prediction formulas were better than the results obtained from ACI 549.4R (2013).

The results show that the load-carrying capacity at the yielding of steel and the FRCM failure were underestimated by ACI 549.4R (2013). The explanation is that only the second linear part of the bi-linear tensile stress-strain curve of the carbon-FRCM composite is used in the ACI 549.4R (2013). The contribution of the mortar matrix to the tensile properties of the carbon-FRCM composite is neglected. In addition, the slippage of CF mesh results in the smaller modulus of elasticity of carbon-FRCM in the second linear part. The results based on the proposed prediction formulas fit well with the experimental results. It also should be noted that it is a slight underestimate for the S-B-L1 beam, and a slight overestimate for the S-B-L2 beam. It is possible due to the accuracy of the model to predict the apparent strain of CF mesh from the measured strain of carbon-FRCM in the tensile tests. In further research, more repeated carbon-FRCM specimens need to be prepared to improve the prediction model of CF mesh within the mortar matrix in the carbon-FRCM.

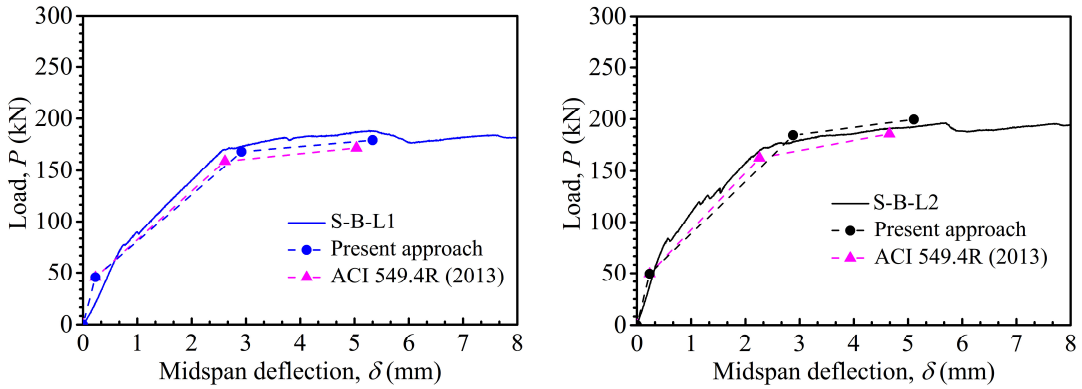

(a) S-B-L1 beam (b) S-B-L2 beam

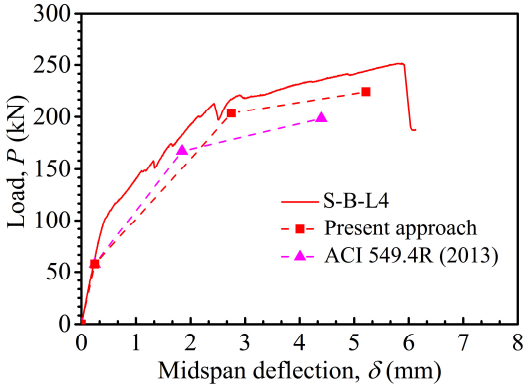

(c) S-B-L4 beam

Fig. 2.31 Comparison of load-deflection behavior between experimental and analytical results.

Table 2.12 Comparison of the deflection of beams with externally bonded M/C-FRCM between experimental and analytical results.

Beam	Deflection at yielding of steel (mm)			Deflection at failure of carbon-FRCM (mm)		
	Experimental	Present approach	ACI 549.4R	Experimental	Present approach	ACI 549.4R
S-B-L1	2.62	2.92	2.61	5.27	5.34	5.04
S-B-L2	2.33	2.88	2.26	5.69	5.11	4.66
S-B-L4	2.43	2.75	1.84	5.87	5.22	4.40

Table 2.13 Comparison of the load-carrying capacity of beams with externally bonded M/C-FRCM between experimental and analytical results.

Beam	Load-carrying capacity of beam at yielding of steel (kN)			Load-carrying capacity of beam at failure of carbon-FRCM (kN)		
	Experimental	Present approach	ACI 549.4R	Experimental	Present approach	ACI 549.4R
S-B-L1	170.19	168.15	158.93	188.38	179.17	171.66
S-B-L2	172.12	184.30	162.59	196.12	199.48	185.70
S-B-L4	212.78	203.43	167.32	251.50	224.20	198.25

2.8 Conclusions of this chapter

In this chapter, to propose new prediction formulas in flexure for RC beams with externally bonded carbon-FRCM, the static tensile tests of M/C-FRCM was performed. To verify the prediction formulas, the flexural behavior of RC beams with externally bonded M/C-FRCM was experimentally investigated under static loading. The results can be concluded as follows:

(1) In the static tensile tests of M/C-FRCM, the typical failure mode of M/C-FRCM was fabric slippage at the cracks of the mortar matrix, and the number of layers of CF mesh had a slight

influence on the tensile stress-strain relation. Even so, two-layer carbon-FRCM was an optimized selection in the design of multilayer carbon-FRCM composites due to the superior mechanical characteristics (i.e., higher modulus of elasticity and tensile strength as well as tensile strain at failure) under tensile loading.

(2) To characterize the fabric slippage behavior in the M/C-FRCM under tensile loading, the apparent strain of carbon fabric (CF) mesh was proposed to represent the actual strain of carbon-FRCM composite in tension. The model of apparent strain of CF mesh was obtained based on the global tensile strain of carbon-FRCM in the static tensile tests. It was revealed that the apparent strain of CF mesh ranged from 0.006 to 0.008 at the tensile failure of M/C-FRCM. With regarding the tensile strength of dry carbon fiber bundles, the utilization efficiency of fibers was around 70% on average.

(3) By assessing the currently available prediction approaches for the FRCM system, it was concluded that the ACI 549.4R could be firstly considered in the design and analysis of the FRCM system. The new ready-to-be-published Italian guidelines are worth to be expected. The design method of the modified bond strength model of FRP system might not be used in the FRCM system. The prediction formulas of debonding strain of FRCM based on both experimental bond tests and flexural tests could be further considered.

(4) Results of static four-point bending tests evidenced the effectiveness of M/C-FRCM in strengthening RC beams by increasing the load-carrying capacity at the yielding of steels and ultimate capacity. The failure mode was differentiated as the layers of CF mesh increased in which the fabric slippage was typical at a lower amount of CF mesh scenarios (one- and two-layer carbon-FRCM), and it changed to debonding and peeling-off of concrete cover at a higher amount of CF mesh scenarios (four-layer carbon-FRCM). The utilization efficiency of CF mesh in the M/C-FRCM reached at 61% on average for strengthening beams

(5) An analytical study on the prediction formulas in flexure for RC beams with externally bonded carbon-FRCM was performed. The critical modification for the prediction approach provided by the ACI 549.4R is that the apparent strain of CF mesh (i.e., mechanical properties of CF mesh) was adopted in the proposed prediction formulas to assess the contribution of M/C-FRCM to strengthening. The flexural capacity predicted by ACI 549.4R using the simplified mechanical properties of FRCM underestimated the experimental results, while the prediction results of the proposed prediction formulas in this chapter agreed well with the experimental results.

APPENDIX A.1. Calculation process for the tensile stress-strain of FRCM composite

ICC-ES AC434 (2016) provides an expected bi-linear tensile stress-strain relation of FRCM composite material through a series of definitions and calculations. The bi-linear response curve is comprised of an initial line for uncracked specimen, the secondary line for cracked specimen, and possibly a curved transition segment in between. The initial and secondary lines shall be continued until they intersect at the one point that the corresponding stress and strain are calculated as the transition point data. In the initial line, the tensile modulus of elasticity of the uncracked specimen (E_{frcm}^{*}) is calculated using Eq. (A.1.1):

$$E_{frcm}^{*} = \Delta\sigma / \Delta\varepsilon \qquad \text{.....(A.1.1)}$$

Where: $\Delta\sigma$ = difference in tensile stress between two selected points; $\Delta\varepsilon$ = difference in tensile strain between two selected points.

In the secondary line corresponding to cracked behavior after the transition, two points are selected on the experiment curve at a stress level equal to $0.9f_{u\_frcm}$ and $0.6f_{u\_frcm}$. The slope of the line that connects these two points represents the tensile modulus of elasticity in that region, as shown in Eq. (A.1.2):

$$E_{frcm} = \Delta\sigma / \Delta\varepsilon = \frac{0.9f_{u\_frcm} - 0.6f_{u\_frcm}}{\varepsilon_{@0.9\,fu\_frcm} - \varepsilon_{@0.6\,fu\_frcm}} \qquad \text{.....(A.1.2)}$$

The ultimate tensile stress (f_{u_frcm}) is calculated using Eq. (A.1.3):

$$f_{u\_frcm} = F_{max} / A_{cf} \qquad \text{.....(A.1.3)}$$

Where: F_{max} = maximum load before failure; A_{cf} = cross-section area of fabric mesh reinforcement.

Meanwhile, the ultimate tensile strain (ε_{u_frcm}) is by obtaining the y-intercept (Eq. (A.1.4)) of the line used to compute E_{frcm} as defined in Eq. (A.1.2) and the following equation Eq. (A.1.5):

$$y_{intercept} = 0.6f_{u\_frcm} - E_{frcm}\varepsilon_{@0.6\,fu\_frcm} \qquad \text{.....(A.1.4)}$$

$$\varepsilon_{u\_frcm} = \left(f_{u\_frcm} - y_{intercept}\right) / E_{frcm} \qquad \text{.....(A.1.5)}$$

APPENDIX A.2. Comparison of tensile stress-strain of M/C-FRCM

Fig. A.2.1 presents the comparison of tensile stress-strain of M/C-FRCM based on the calculation process shown in Appendix A.1. The continuous line in each figure represents the experimental results, and the line with marks represents the calculated results according to the ICC-ES AC434 (2016).

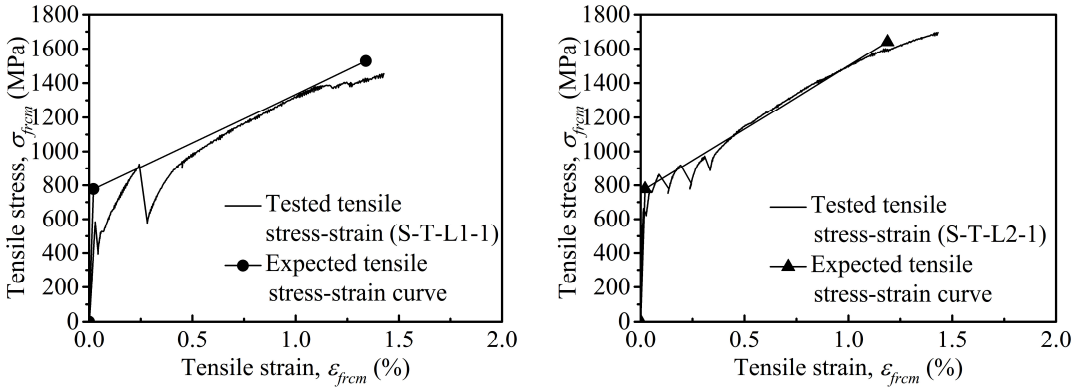

(a) S-T-L1-1 (b) S-T-L2-1

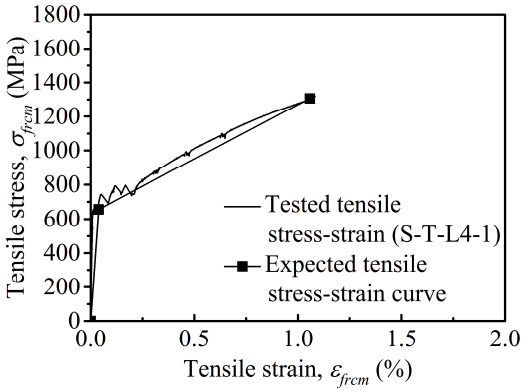

(c) S-T-L4-1

Fig. A.2.1 Comparison of tensile stress-strain of M/C-FRCM specimens.

APPENDIX A.3. Fitting process of apparent strain of CF

Fig. A.3.1 presents the fitting process of apparent strain of CF mesh in M/C-FRCM under static loading. The black lines in each figure represent the experimental results, and the red dash curve represents the fitting results.

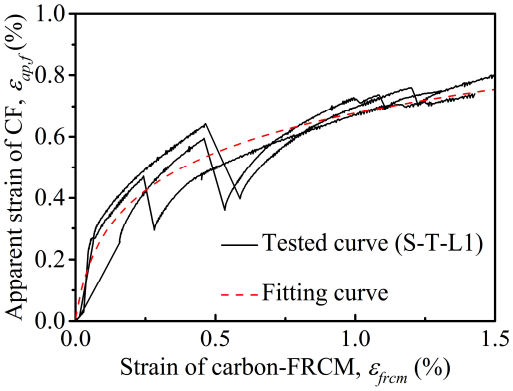

(a) S-T-L1

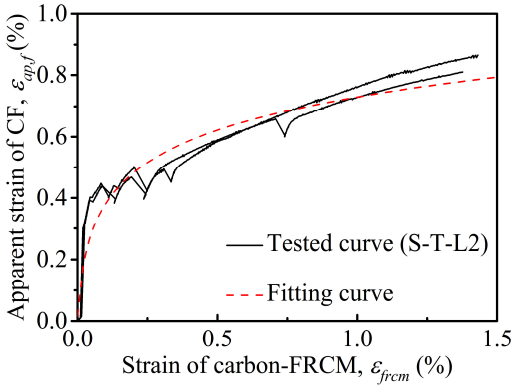

(b) S-T-L2

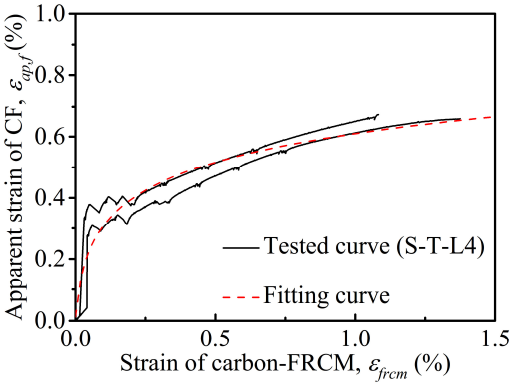

(c) S-T-L4

Fig. A.3.1 Apparent strain of CF mesh vs. strain of carbon-FRCM composite.

List of Figures

List of Tables

References

AC434, 2016. Acceptance Criteria for Masonry and Concrete Strengthening Using Fabric-reinforced Cementitious Matrix (FRCM) and Steel Reinforced Grout (SRG) Composite Systems. ICC Evaluation Service.

ACI 318, 2014. Building Code Requirements for Structural Concrete and Commentary. American Concrete Institute. U.S.A.

ACI 549.4R, 2013. Guide to design and construction of externally bonded fabric-reinforced cementitious matrix (FRCM) systems for repair and strengthening concrete and masonry structures. American Concrete Institute, U.S.A.

Aljazaeri, Z.R., Janke, M.A. and Myers, J.J., 2019. A novel and effective anchorage system for enhancing the flexural capacity of RC beams strengthened with FRCM composites. Composite Structures, 210, 20-28.

Ascione, L., Carozzi, F.G., D'Antino, T. and Poggi, C., 2018. New Italian guidelines for design of externally bonded Fabric-Reinforced Cementitious Matrix (FRCM) systems for repair and strengthening of masonry and concrete structures. Procedia Structural Integrity, 11, 202-209.

ASTM D4018, 1999. Standard Test Methods for Properties of Continuous Filament Carbon and Graphite Fiber Tows. American Society for Testing and Materials, U.S.A.

Awani, O., El Refai, A. and El-Maaddawy, T., 2015. Bond characteristics of carbon fabric-reinforced cementitious matrix in double shear tests. Construction and Building Materials, 101, 39-49.

Bencardino, F., Carloni, C., Condello, A., Focacci, F., Napoli, A. and Realfonzo, R., 2018. Flexural behaviour of RC members strengthened with FRCM: State-of-the-art and predictive formulas. Composites Part B: Engineering, 148, 132-148.

BS EN 196-1, 1995. Methods of testing cement — Part 1: Determination of strength. British Standard.

Ceroni, F. and Salzano, P., 2018. Design provisions for FRCM systems bonded to concrete and masonry elements. Composites Part B: Engineering, 143, 230-242.

Dai, J.G., Yokota, H. and Ueda, T., 2009. A hybrid bonding system for improving the structural performance of FRP flexurally strengthened concrete beams. Advances in Structural Engineering, 12(6), 821-832.

D'Ambrisi, A. and Focacci, F., 2011. Flexural strengthening of RC beams with cement-based composites. Journal of Composites for Construction, 15(5), 707-720.

D'Ambrisi, A., Feo, L. and Focacci, F., 2013. Experimental analysis on bond between PBO-FRCM strengthening materials and concrete. Composites Part B: Engineering, 44(1), 524-532.

D'Antino, T., Colombi, P., Carloni, C. and Sneed, L. H., 2018. Estimation of a matrix-fiber interface cohesive material law in FRCM-concrete joints. Composite Structures, 193, 103-112.

D'Antino, T., Sneed, L.H., Carloni, C. and Pellegrino, C., 2015. Influence of the substrate characteristics on the bond behavior of PBO FRCM-concrete joints. Construction and Building Materials, 101, 838-850.

D'Antino, T., Sneed, L.H., Carloni, C. and Pellegrino, C., 2016. Effect of the inherent eccentricity in single-lap direct-shear tests of PBO FRCM-concrete joints. Composite Structures, 142, 117-129.

Ebead, U., Shrestha, K.C., Afzal, M.S., El Refai, A. and Nanni, A., 2017. Effectiveness of fabric-reinforced cementitious matrix in strengthening reinforced concrete beams. Journal of Composites for Construction, 21(2), 04016084.

Elghazy, M., El Refai, A., Ebead, U. and Nanni, A., 2017. Effect of corrosion damage on the flexural performance of RC beams strengthened with FRCM composites. Composite Structures, 180, 994-1006.

Elghazy, M., El Refai, A., Ebead, U. and Nanni, A., 2018. Post-repair flexural performance of corrosion-damaged beams rehabilitated with fabric-reinforced cementitious matrix (FRCM). Construction and Building Materials, 166, 732-744.

Grande, E. and Milani, G., 2018. Interface modeling approach for the study of the bond behavior of FRCM strengthening systems. Composites Part B: Engineering, 141, 221-233.

Jabr, A., El-Ragaby, A. and Ghrib, F., 2017. Effect of the fiber type and axial stiffness of FRCM on the flexural strengthening of RC beams. Fibers, 5(1), 2.

JSCE guidelines for concrete, 2007. Standard Specifications for Concrete Structures – Design. Japan Society of Civil Engineers.

Jung, K., Hong, K., Han, S., Park, J. and Kim, J., 2015. Prediction of flexural capacity of RC beams strengthened in flexure with FRP fabric and cementitious matrix. International Journal of Polymer Science, 2015.

Li, X., Gu, X., Song, X., Ouyang, Y. and Feng, Z., 2013. Contribution of U-shaped strips to the flexural capacity of low-strength reinforced concrete beams strengthened with carbon fibre composite sheets. Composites Part B: Engineering, 45(1), 117-126.

Ombres, L., 2015. Analysis of the bond between fabric reinforced cementitious mortar (FRCM) strengthening systems and concrete. Composites Part B: Engineering, 69, 418-426.

Raoof, S. M., Koutas, L. N. and Bournas, D. A. 2016. Bond between textile-reinforced mortar (TRM) and concrete substrates: Experimental investigation. Composites Part B: Engineering, 98, 350-361.

Sneed, L.H., D'Antino, T. and Carloni, C., 2014. Investigation of Bond Behavior of

Polyparaphenylene Benzobisoxazole Fiber-Reinforced Cementitious Matrix-Concrete Interface. ACI Materials Journal, 111, 1-12.

Su, M.N., Wei, L.L., Zeng, Z.W., Ueda, T., Xing, F. and Zhu, J.H., 2019. A solution for sea-sand reinforced concrete beams. Construction and Building Materials, 204, 586-596.

Teng, J.G., Smith, S.T., Yao, J. and Chen, J.F., 2003. Intermediate crack-induced debonding in RC beams and slabs. Construction and building materials, 17(6-7), 447-462.

Toutanji, H. and Deng, Y., 2007. Comparison between organic and inorganic matrices for RC beams strengthened with carbon fiber sheets. Journal of Composites for Construction, 11(5), 507-513.

Younis, A. and Ebead, U. 2018. Bond characteristics of different FRCM systems. Construction and Building Materials, 175, 610-620.

CHAPTER 3

INVESTIGATION OF RC BEAMS WITH EXTERNALLY BONDED M/C-FRCM UNDER CYCLIC LOADING

3.1 Introduction

A study of RC beams with externally bonded M/C-FRCM was carried out under static loading in chapter 2. Considering the urgent requirements for understanding the fatigue response of FRCM composites and helping the development of fatigue design of RC beams in the FRCM system, an investigation of RC beams with externally bonded M/C-FRCM was conducted under cyclic loading in this chapter.

The cyclic tensile tests of M/C-FRCM and cyclic bending tests of RC beams with externally bonded M/C-FRCM were carried out. The preparation of M/C-FRCM for tensile tests was the same with specimens in section 2.3.1 of chapter 2. Meanwhile, the preparation of M/C-FRCM for strengthening RC beams was the same as beam specimens in section 2.3.1 and section 2.3.2 of chapter 2. Here, the cyclic tensile tests program and cyclic bending tests program are presented.

3.2 Experimental program

3.2.1 Cyclic tensile tests program of M/C-FRCM

The loading program of the cyclic tensile tests is shown in Fig. 3.1. A constant-amplitude cyclic load was used. The load ratio of the minimum load to the maximum load was 10%. The load force level (L_t) and load ratio (R_t) were calculated as Eq. (3.1) and Eq. (3.2), respectively. A sinusoidal wave load was performed at a loading frequency of 5 Hz. All test specimens were tested under a static loading after a pre-determined number of cycles to detect the evolution of the constitutive properties of M/C-FRCM suffering from cyclic tensile loading. The static tensile test setup of M/C-FRCM was the same as described in section 2.3.3 of chapter 2. The static loading was from 0 to the fatigue maximum load (F_{max_t}) at a constant rate of 0.20 mm/min and then unloaded to 0. Recording the tensile load, deformations of M/C-FRCM at the intermittent static tensile loading tests and the corresponding number of cycles.

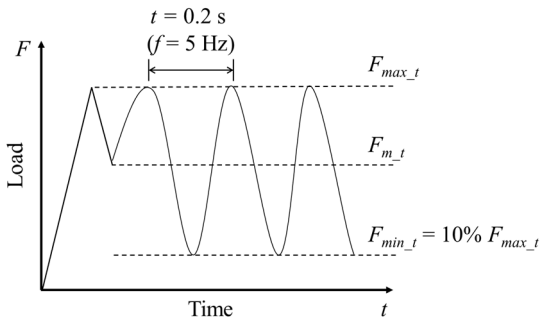

Fig. 3.1 Cyclic loading program for tensile tests of carbon-FRCM specimens.

$$L_t = F_{\max\_t} / F_{u\_t} \quad \text{.....(3.1)}$$

$$R_t = F_{\min\_t} / F_{\max\_t} \quad \text{.....(3.2)}$$

Table 3.1 presents the overall information of M/C-FRCM specimens used in the cyclic tensile tests. A total of 9 carbon-FRCM specimens were prepared. The labeling of the carbon-FRCM specimens was termed starting with C-T (cyclic tensile loading), followed by the number of layers of CF mesh (i.e., L1, L2, and L4) and load force levels (i.e., F40, F50, F60) in the percentage of the relevant ultimate tensile capacity of the control specimens that were tested statically until failure occurred.

Table 3.1 M/C-FRCM specimens in the cyclic tensile tests.

Carbon-FRCM specimens	Layer of CF mesh	Load force level, L_t (%)	Maximum load force, F_{max_t} (kN)	Minimum load force, F_{min_t} (kN)
C-T-L1-F40		40	2.82	0.28
C-T-L1-F50	1	50	3.53	0.35
C-T-L1-F60		60	4.23	0.42
C-T-L2-F40		40	6.06	0.61
C-T-L2-F50	2	50	7.57	0.76
C-T-L2-F60		60	9.08	0.91
C-T-L4-F40		40	9.64	0.96
C-T-L4-F50	4	50	12.06	1.21
C-T-L4-F60		60	14.47	1.45

3.2.2 Cyclic bending tests program of RC beams with externally bonded M/C-FRCM

The main objective of this program was to obtain data regarding the fatigue performance of RC beams with externally bonded carbon-FRCM plates that could be used for design. It should consider the requirement of comparing the fatigue life and behavior of a strengthened beam with that of a comparable un-strengthened beam. Typical fatigue loading on RC structures is in the region of 10^7 to 10^8 cycles (Barnes et al., 1999). Within the confines of the program, it was not practical to conduct cycling on each beam for periods more than 10^7 cycles. However, some reasonable linear extrapolation is possible from the S-N curve plotted by a logarithmic scale.

Three loading options to achieve a meaningful comparison are briefly summarized as follows (Barnes et al., 1999):

(1) Apply the same loads to both strengthened and un-strengthened beams. In practice, it is unlikely that the actual loading on a strengthened structure will be increased significantly. Therefore, it could be argued that this relates closely to the real-life scenario.

(2) Apply loads to give the same stress range in the rebar in both strengthened and un-strengthened beams. The fatigue life of the RC beam is dependent on the stress range in the steel rebars. Therefore, to make a valid comparison between the strengthened and un-strengthened beams, it could be argued that they should be tested at loads to produce the same stress range in the steel rebar.

(3) Apply the same percentage of the ultimate load capacity to each beam. It is reasonable to expect that the fatigue life of the un-strengthened beam is achieved in the strengthened beam under increased load. Thus, if an un-strengthened beam is tested at a given percentage of its ultimate capacity, then the strengthened beam should be tested at the same percentage of its capacity.

The first loading option was adopted in this program. The loading program of the cyclic bending tests is presented in Fig. 3.2. A constant minimum load level of the applied minimum limit load to the yielding load of the control beam (i.e., S-B-L0 beam, P_{y_b}) was 20%. The maximum load levels of the applied maximum limit load to the yielding load of the control beam (P_{y_b}) were 55%, 60%, and 70% to both strengthened and un-strengthened beams and 80% only to the beam strengthened with four-layer carbon-FRCM composite. The applied load level (L_b) and load ratio (R_b) was calculated as Eq. (3.3) and Eq. (3.4), respectively. A sinusoidal wave load was performed at a loading frequency of 5 Hz. All beams were tested under a static loading after a pre-determined number of cycles to detect the evolution of the structural behavior of the beam suffering from cyclic loading. The static bending test setup of beams was the same as described in section 2.3.4 of chapter 2. The static loading was from 0 to the fatigue maximum limit (P_{y_b}) at a constant rate of 0.5 mm/min and then unloaded to 0. Recording the load, deflections of beams, strains of concrete at the top of the beam and strains of steel rebars, deformations of the carbon-FRCM plate, and recoding the corresponding number of cycles.

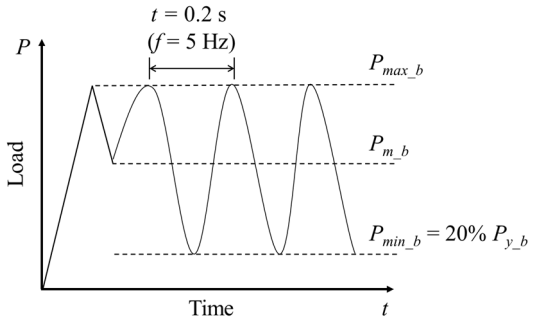

Fig. 3.2 Cyclic loading program for four-point bending tests of beams.

$$L_b = P_{\max\_b} / P_{y\_b} \quad \text{……..(3.3)}$$

$$R_b = P_{\min\_b} / P_{\max\_b} \quad \text{……..(3.4)}$$

Table 3.2 presents the overall information of beams used in the cyclic bending tests. A total of 12 beams were prepared in which 3 were un-strengthened beams, and 9 were beams with externally bonded M/C-FRCM composites. The labeling of beams was termed starting with C-B (cyclic bending loads), followed by the number of layers of CF mesh (i.e., L0, L1, L2, and L4) and applied load levels (i.e., F55, F60, F70, F80) in the percentage of the yielding load capacity of the control beam (i.e., S-B-L0 beam) that were tested statically.

Table 3.2 RC beams with externally bonded M/C-FRCM in the cyclic bending tests.

Beams	Layer of CF mesh	Applied load level, L_b (%)	Applied minimum limit load, P_{min_b} (kN)	Applied maximum limit load, P_{max_b} (kN)
C-B-L0-F55	0	55	31.3	86.0
C-B-L0-F60		60	31.3	93.8
C-B-L0-F70		70	31.3	109.4
C-B-L1-F55	1	55	31.3	86.0
C-B-L1-F60		60	31.3	93.8
C-B-L1-F70		70	31.3	109.4
C-B-L2-F55	2	55	31.3	86.0
C-B-L2-F60		60	31.3	93.8
C-B-L2-F70		70	31.3	109.4
C-B-L4-F60	4	60	31.3	86.0
C-B-L4-F70		70	31.3	93.8
C-B-L4-F80		80	31.3	109.4

3.3 Fatigue tensile test results of M/C-FRCM

3.3.1 Failure modes of M/C-FRCM under cyclic loading

Fig. 3.3 shows the comparison of tensile failure modes of carbon-FRCM under static and cyclic loading. Both failure modes were independent of the layers of CF mesh. With regarding the number of cracks, more than two cracks were observed in the M/C-FRCM under static loading, while only one crack was observed under cyclic loading. All these cracks were perpendicular to the longitudinal carbon fibers in the direction of tensile loading. As far as the propagation of the width of cracks, the maximum width of the major crack in the carbon-FRCM was less than 3 mm under static loading. When the carbon-FRCM suffering from the cyclic loading, the crack was around 1.5 mm before the catastrophic tensile failure as the width of crack sharply increased to 15-20 mm. The most apparent distinguish referred to the condition of carbon fibers at the crack. The fiber bundles maintained nearly intact at the major crack caused by the static loading. In contrast, the fibers breakage and fiber bulking were observed in the middle of the crack resulted from the cyclic loading (see Fig. 3.3(b)). The defect of fibers and the accumulation of fatigue damage might induce fiber breakage. The extensive slippage of fibers within the mortar matrix caused the exposure of fibers with long length. The fiber bulking occurred when the remaining unbroken fibers could not sustain the tensile load. Thus, the fatigue failure mode of M/C-FRCM was the fiber breakage in the primary direction combined with extensive slippage of fibers at the crack of the mortar matrix.

(a) Tensile failure mode under static loading

(b) Tensile failure mode under cyclic loading

Fig. 3.3 Comparison of tensile failure modes of carbon-FRCM under static and cyclic loading.

3.3.2 Fatigue degradation characteristics of M/C-FRCM

It is a great understanding that the cyclic loading can induce damage in composite materials where the damage accumulates with increasing cycles, and the failure occurs when some critical level of damage is exceeded (Degrieck et al., 2001; Sevenois et al., 2015). The damage process of M/C-FRCM may have several components involving the fiber breakage, decohesion between fibers, and mortar matrix that could eventually increase the slippage of fibers within the mortar matrix. Moreover, the slippage of fibers leads to the stiffness reduction of M/C-FRCM. The damage grows as increasing the number of cycles until a critical slippage caused by the aggregation of damage (suffering from the fiber breakage and decohesion of fibers within mortar matrix) forms and propagates catastrophically.

The tensile stress versus strain hysteresis curves after different cycles are representative to clarify the evolution of the tensile properties of M/C-FRCM under cyclic loading. Fig. 3.4 describes the tensile stress versus strain hysteresis curves for C-T-L2 specimens. The black dash lines in Fig. 3.4 represents the initial state of each M/C-FRCM before testing. The tensile stress of M/C-FRCM increased until the cracking of the mortar matrix occurred, and then unloaded to zero. It can be found that the initial stiffness of M/C-FRCM was more than a thousand GPa that was rather higher than the Young modulus of dry CF mesh. This is due to the calculation of tensile stress was in terms of the cross-section area of dry CF mesh, but the tensile load was carried by both the mortar matrix and dry CF mesh. All M/C-FRCM specimens had an initial one crack before the first recording of the static loading up to the maximum fatigue load (F_{max_t}). It should be noted that there was an initial residual deformation of M/C-FRCM at the first cycle that was followed by the initiation of cracking and before the cyclic loading. The residual deformation was due to the fabric slippage after cracking of the mortar matrix. The residual deformation at the first cycle increased as the fatigue maximum load increased, where it was 0.029 mm in the C-T-L2-F40, 0.036 in the C-T-L2-F50, and 0.219 mm in the C-T-L2-F60. The tensile stress-strain hysteresis curves were enclosed after lots of cycles. The possible fiber breakage and slippage of fibers caused the residual strain at every two adjacent hysteresis curves.

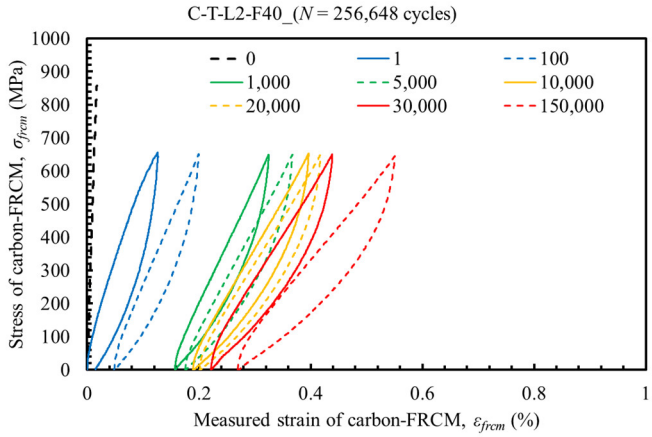

(a) C-T-L2-F40 specimen

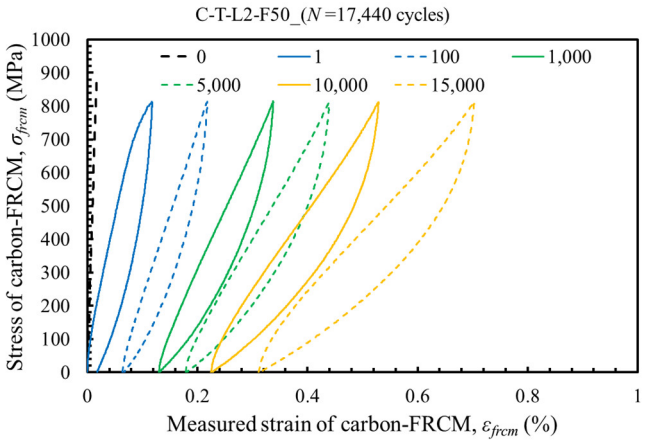

(b) C-T-L2-F50 specimen

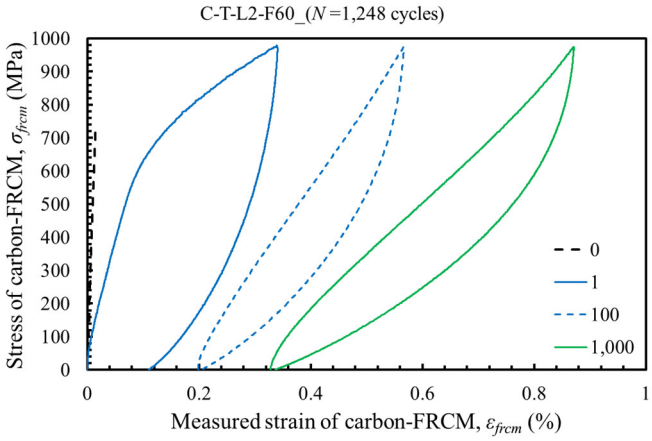

(c) C-T-L2-F60 specimen

Fig. 3.4 Tensile stress versus strain hysteresis curves of C-T-L2 specimens.

The general characteristics of tensile properties of M/C-FRCM under cyclic loading involved the increase of both residual strain and maximum strain and decrease of elastic modulus in the loading branch. Fig. 3.5 presents the cumulative deformation of M/C-FRCM with increasing cycles. The cumulative deformation is the maximum deformation up to the maximum fatigue load after specific cycles. It rose sharply when the cycles reached the coming failure. The cumulative deformation increased as an increase of the maximum fatigue load and decreased as increasing of the layers of CF mesh.

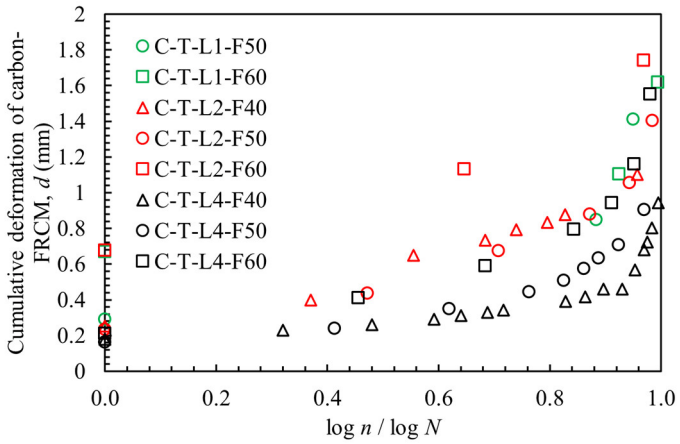

Fig. 3.5 Cumulative deformation of M/C-FRCM with increasing cycles.

Fig. 3.6 indicates the evolution of the stiffness of M/C-FRCM with increasing cycles. A significant stiffness reduction was observed that was attributed to the fabric slippage. To clarify the law of stiffness reduction, the ratio of the FRCM's stiffness (E_{frcm}) to the Young modulus of CF mesh (E_{cf}) was adopted. Linear fitting of the stiffness reduction was followed by Eq. (3.5). Considering the 95% probability survival, Eq. (3.5) is converted to Eq. (3.6). The E_{frcm} was equal to E_{cf} at the fatigue failure.

$$\frac{E_{frcm}}{E_{cf}} = -2.11 \times \frac{\log n}{\log N} + 3.26 \qquad \text{.....(3.5)}$$

$$\frac{E_{frcm}}{E_{cf}} = -2.11 \times \frac{\log n}{\log N} + 3.11 \qquad \text{.....(3.6)}$$

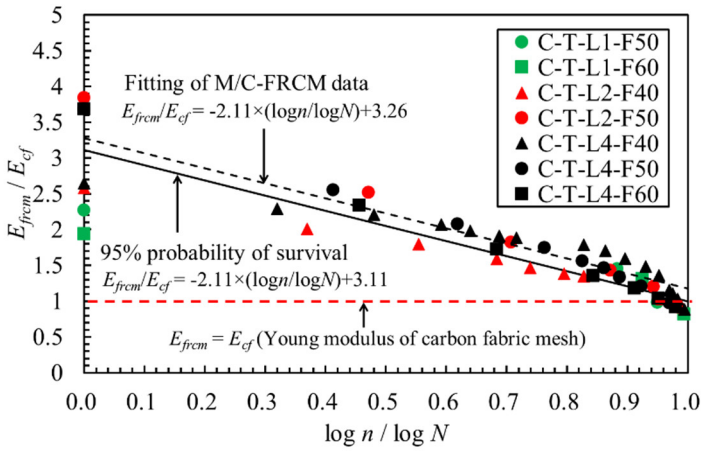

Fig. 3.6 Stiffness reduction of M/C-FRCM with increasing cycles.

3.3.3 Fatigue life performance of M/C-FRCM

Table 3.3 displays the results of the fatigue life performance of M/C-FRCM specimens. It seems that the influence of layers of CF mesh on the fatigue life performance was not observed. Thus, the prediction of fatigue life of M/C-FRCM was proposed based on the total fatigue tensile test data. Finally, the characteristic of fatigue life of M/C-FRCM was compared to the fatigue life

performance of steel rebar and fatigue strength of CFRP material that is impregnated by the epoxy resin.

Table 3.3 Fatigue life results of M/C-FRCM specimens.

Carbon-FRCM specimens	Layer of CF mesh	Load force level, L_t (%)	Load force ratio, R_t (%)	Number of cycles to failure, N ($\times 10^3$)
C-T-L1-F40	1	40	10	2000
C-T-L1-F50	1	50	10	33.7
C-T-L1-F60	1	60	10	22.2
C-T-L2-F40	2	40	10	256.6
C-T-L2-F50	2	50	10	17.4
C-T-L2-F60	2	60	10	1.25
C-T-L4-F40	4	40	10	1777.5
C-T-L4-F50	4	50	10	70.5
C-T-L4-F60	4	60	10	24.4

Fig. 3.7 compares the fatigue life models between M/C-FRCM tested in this chapter and conventional steel rebar. The stress range of material in the process of cyclic loading was used to assess the effect of minimum and maximum fatigue load on the fatigue life (Papakonstantinou et al., 2007). The stress range is obtained by the maximum tensile stress minus minimum tensile stress. The present regression model of M/C-FRCM is proposed as Eq. (3.7). Eq. (3.8) and Eq. (3.9) are the fatigue life model of steel rebar proposed by Helagson and Hanson (1974) and published by fib model code (2010). It is a general characteristic that fatigue life decreased as an increase of stress range. The fatigue life of M/C-FRCM was higher than the steel rebar at the same stress range. From the perspective of design, Helgason and Hanson (1974) reported that 121 MPa was the steel stress range where endurance limit occurs that is the fatigue cycle over two million. This value is 125 MPa by solving the Eq. (3.9). Besides, ACI 215R (1974) limits the steel stress range in rebar to be 138 MPa, while AASHTO (2017) limits the steel stress range to 162 MPa for design applications. The endurance limit stress range of M/C-FRCM can reach at 490 MPa by the linear extrapolation of Eq. (3.7). It concluded that the fatigue life performance of M/C-FRCM was superior to the steels.

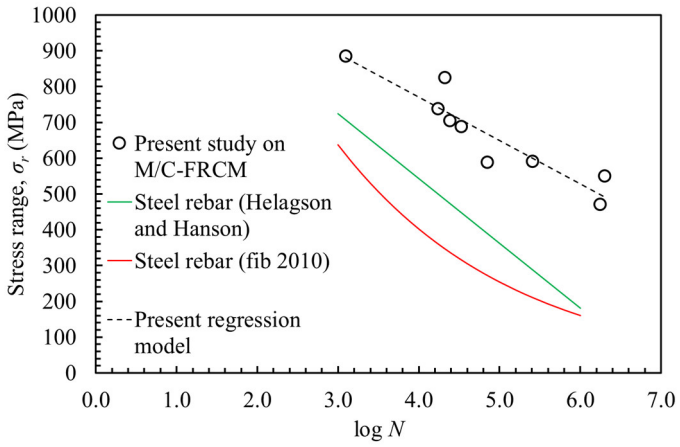

Fig. 3.7 Comparison of fatigue life model between the present M/C-FRCM and steel rebar.

$$\sigma_r = 1256.3 - 121.4 \log N \quad \text{.....(3.7)}$$

$$\log N = 6.969 - 0.0055 \sigma_r \quad \text{.....(3.8)}$$

$$\Delta\sigma_{Es} = \Delta\sigma_{Rsk}\left(\frac{N^*}{N_f}\right)^{\frac{1}{m}} = \Delta\sigma_{Rsk}\left(\frac{10^6}{10^{\log N}}\right)^{\frac{1}{5}} \quad \text{.....(3.9)}$$

When the diameter of steel rebar $\phi \leq 16$ mm, then $\Delta\sigma_{Rsk}$ = 160 MPa at $N^* = 10^6$; The stress exponent $m = 5$; therefore, the fatigue life N_f could be obtained based on the relevant stress range $\Delta\sigma_{Es} = \sigma_{max} - \sigma_{min}$.

Where $\Delta\sigma_{Rsk}$ is the stress range relevant to N^* cycles; m is a stress exponent in the characteristic fatigue strength function; N^* is the characteristic cycles; $\Delta\sigma_{Es}$ is the steel stress range under the acting loads; σ_{max} and σ_{min} are the maximum and minimum steel stress corresponding to the maximum and minimum applied load in the fatigue tests of beams; N_f is the predicted fatigue life at the stress range $\Delta\sigma_{Es}$.

Fig. 3.8 compares the fatigue strength model between M/C-FRCM and CFRP material. The fatigue strength model of M/C-FRCM with 95% probability of survival is proposed as Eq. (3.10). The normalized stress that is the ratio of the fatigue maximum stress to the ultimate tensile strength was used in the fatigue strength model (Pandita et al., 2001; Lian et al., 2010). The fatigue strength degradation of FRP material was studied by Demers (1998), and the fatigue strength model of CFRP is given as Eq. (3.11). Besides, Wu et al. (2010) investigated the fatigue response of FRP and proposed the fatigue strength model like Eq. (3.12), which is at 95% probability of survival. The maximum applied force ratio indicates the fatigue limit of FRP composites to achieve at least two million cycles of fatigue life. For the CFRP composites, it can be calculated based on Eq. (3.11) and Eq. (3.12), where the fatigue limits were 78.7% and 55.2% of the ultimate tensile load capacity, respectively. Besides, for the CFRP material, ACI 440.2R (2008) recommended that the fatigue stress limit is 55% of the static tensile strength. Moreover, for the FRCM composite, the identical fatigue stress limit of 55% is also recommended for the fiber type of carbon fabric in the ACI 549.4R (2013). However, results indicated that the fatigue performance of M/C-FRCM was inferior to the CFRP. The fatigue stress limit of carbon-FRCM was 36% by using Eq. (3.10). The mechanical behavior of FRCM that is impregnated by the mortar matrix is rather differentiated from the CFRP that is impregnated by epoxy resin. The fatigue failure mode of FRCM and FRP composites are also different in which the former is fiber breakage combined with extensive slippage of fibers, and the latter is complete rupture failure of FRP. Therefore, the fatigue stress limit of carbon-FRCM in the current design guideline for FRCM composite (ACI 549.4R, 2013) is possible to be unsafe. The fatigue stress limit of carbon-FRCM could be reduced to around 35% according to the study in this chapter. Further, an extensive database of tensile tests of carbon-FRCM is also necessary to make a more precise assessment for the fatigue stress limit.

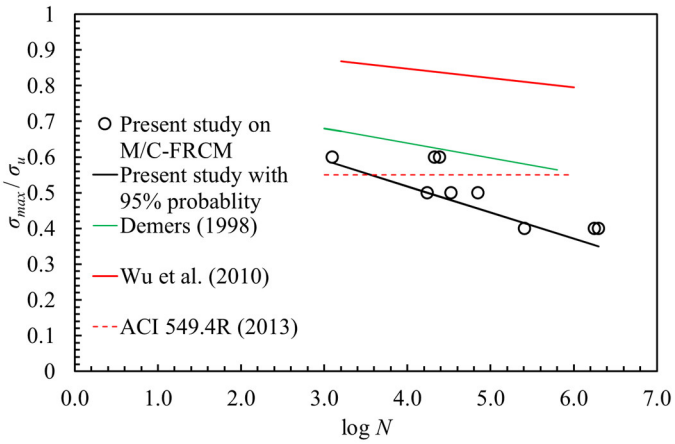

Fig. 3.8 Comparison of fatigue strength model between the present M/C-FRCM and epoxy resin-based CFRP composites.

$$\frac{\sigma_{max}}{\sigma_u} = 0.810 - 0.073 \log N \quad \text{.....(3.10)}$$

$$\frac{\sigma_{max}}{\sigma_u} = 0.8133 - 0.0415 \log N \quad \text{.....(3.11)}$$

$$\frac{\sigma_{max}}{\sigma_u} = 0.951 - 0.026 \log N \quad \text{.....(3.12)}$$

3.4 Fatigue bending test results of beams with externally bonded M/C-FRCM

3.4.1 Failure modes of beams with externally bonded M/C-FRCM under cyclic loading

The same failure mode was observed for all the beams under cyclic loading, except for the C-B-L4-F60 beam that reached the pre-setting limit of two million cycles. The failure mode was due to the fracture of steel rebars in tension (see Fig. 3.9(a)) for both non-strengthened and strengthened beams. The fracture of the steel rebar was visible after the completion of cyclic loading in a sudden way. In general, some flexural cracks initiated at the first cycle and propagated as the number of cycles increased. Both non-strengthened and strengthened beams exhibited one major flexural crack within the region of the two loading points, and some smaller cracks were observed near the region of the loading points (see Fig. 3.9(b) and (c)).

Although the steel fracture was identical regardless of bonding M/C-FRCM composites, some distinct behavior of carbon-FRCM was observed depending on the layers of CF mesh for strengthening. The fabric slippage at the major flexural crack was observed in all strengthened beams. Either debonding at the matrix-concrete interface or debonding at the fabric-mortar interface plane were not observed in C-B-L1 and C-B-L2 beams at all of three fatigue load levels, except for the C-B-L4 beams. The debonding occurred at the matrix-concrete interface initiating from the cut-off end of the four-layer carbon-FRCM and propagated along the bonding interface followed by a shear crack, as shown in Fig. 3.9(c).

In strengthened beams after the steel fracture, the failure of fabric within the mortar matrix can be seen in Fig. 3.9 (d) and (e). Before such catastrophic failure, the deflections of strengthened

beams increased significantly, and then the sudden fracture of steel occurred, followed by observing the fiber breakage and extensive slippage of fibers. The carbon fiber bundles were tightening at the major flexure crack before the completion of cyclic loading. It is proven that the failure of M/C-FRCM was caused by the sudden phenomenon of steel fracture leading to the rapid increase of deflection. The fabric slippage was always initiated during the first cycle and propagated with the increasing of cycles. Typically, the propagation of fabric slippage can be characterized by the width of the major flexural crack that increased gradually as well. After fracture of steel, the carbon fiber bundles almost ruptured completely in C-B-L1 and C-B-L2 beams (see Fig. 3.9 (d)); however, several fiber bundles were survival in C-B-L4 beams due to either more constraint between fibers and mortar matrix or non-uniform distribution of load-carrying at each bundle (see Fig. 3(e)).

(a) Steel fracture in tension

(b) C-B-L1-F60

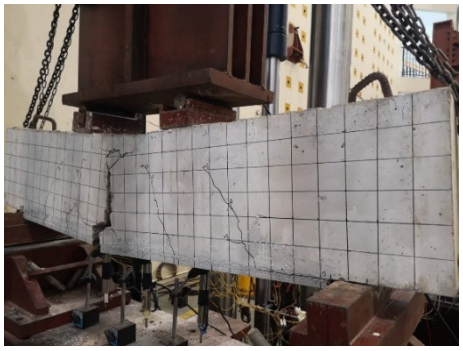

(c) C-B-L4-F80

(d) Carbon-FRCM failure in C-B-L2-60

(e) Carbon-FRCM failure in C-B-L4-F70

Fig. 3.9 Failure modes of beams with externally bonded M/C-FRCM under cyclic loading.

3.4.2 Fatigue degradation characteristics of beams with externally bonded M/C-FRCM

The load-deflection profiles for beams under the static loading tests after some pre-determined number of cycles until the final fatigue failure indicated the changes in deflections and stiffness of beams. The variation of deflections and stiffness can help characterize the damage accumulation due to the increasing the number of cycles (Katakalos et al., 2009). In Fig. 3.10 the load versus deflection hysteresis curves for beams at the applied load level of 60% are illustrated. Other similar curves are presented in Appendix B.1 in this chapter. From the results of the flexural behavior of beams under static loading tests in chapter 2, the tri-linear behavior of load-deflection was observed for all beams. Thus, in Fig. 3.10 the first two stages (i.e., uncracked stage and post-cracking stage) were found for C-B-L0-F60, C-B-L1-F60, and C-B-L2-F60 at the first cycle. It was indicated that cracking of the concrete in the tension side occurred during the uploading process; moreover, a significant residual deflection occurred when the load-carrying capacity of the beam unloaded from the pre-set maximum applied load to zero. This can be attributed mainly to the cracking of concrete that the energy was released. It was verified that the area under the first uploading-unloading curve was significantly larger than the areas under the remaining curves. This phenomenon was also observed in the fatigue response of beams in the FRP system (Gheorghiu et al., 2007; Dong et al., 2012).

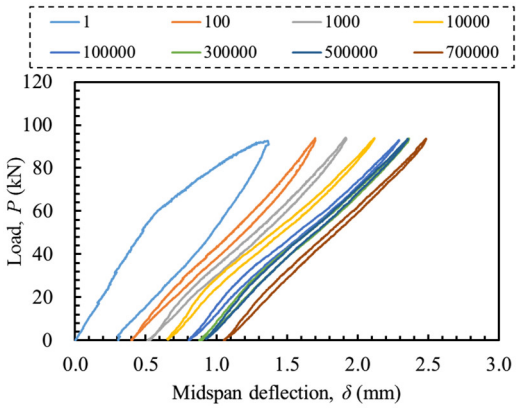

(a) C-B-L0-F60

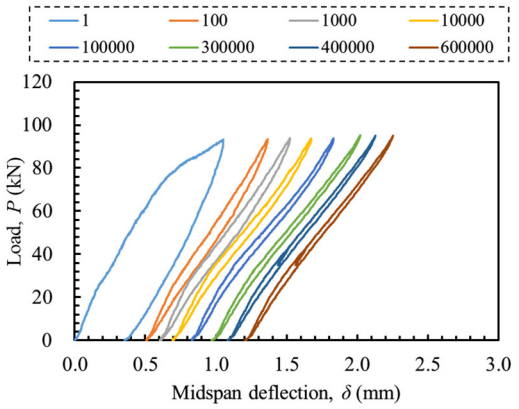

(b) C-B-L1-F60

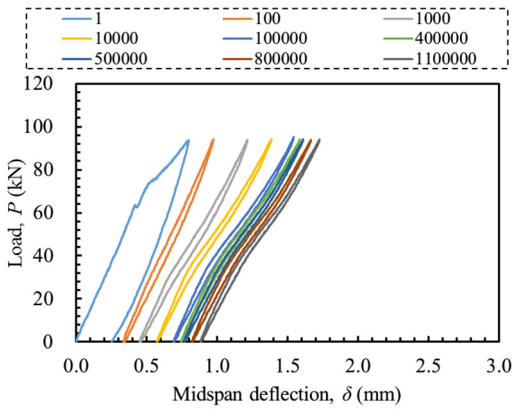

(c) C-B-L2-F60

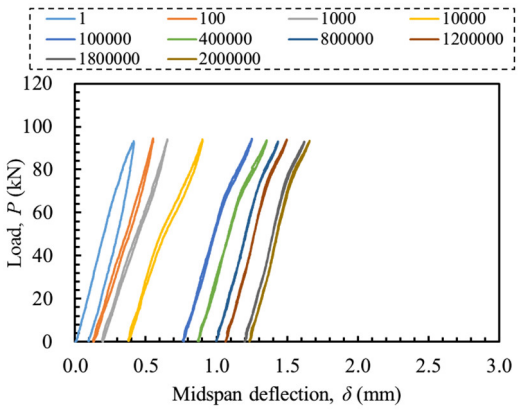

(d) C-B-L4-F60

Fig. 3.10 Load versus deflection hysteresis curves of beams at the applied load level of 60%.

From Fig. 3.10, the residual deflection and the maximum deflection of beams increased with increasing the number of cycles. The changes in the maximum mid-span deflection of beams are illustrated in Fig. 3.11. The general trend was that the maximum deflection of beams increased obviously within the initial 10,000 cycles and then maintained constantly or increased slowly, followed by a significant increase close to the final failure. The portion of the remaining minor changes accounted for more than 80% of the total fatigue life. This shows that the fatigue failure mechanism of beams is a process of accumulation of fatigue damage. The increasing of residual and maximum deflections of beams can be attributed to the creep of concrete during fatigue cycling (Papakonstantinou et al., 2002). With regarding the beams with externally bonded M/C-FRCM, the creep of inorganic mortar matrix and slippage of fabric from the matrix may also lead to an increase of the deflections of strengthened beams (Katakalos et al., 2009). An increase of deformation of M/C-FRCM was observed under cyclic tensile loading due to the fabric slippage and fiber breakage that is described in the section of 3.3.2.

As the same load level was applied, the maximum deflection of beams with increasing the number of cycles decreased as increasing the layers of CF mesh in the carbon-FRCM for strengthening. The changes of maximum deflection between C-B-L0-F55 and C-B-L1-F55 beams were almost identical. This can be due to the limited contribution of one-layer carbon-FRCM to the flexural strengthening at the lower applied load level. In general, the effect of layers of CF on the maximum deflection during fatigue cycling was more distinct at higher applied load level. The maximum deflection of C-B-L0-F70 beams was around 2.5 mm at the applied load level of 70%, which reduced to about 2.0 mm, 1.5 mm, and 1.0 mm as the number of layers increasing from one layer to four layers (see Fig. 3.11(c)). As expected, there was a significant increase of deflections before fracture of steel rebars in concrete. This is a very meaningful observation since the upcoming failure may be detected by monitoring the deflections.

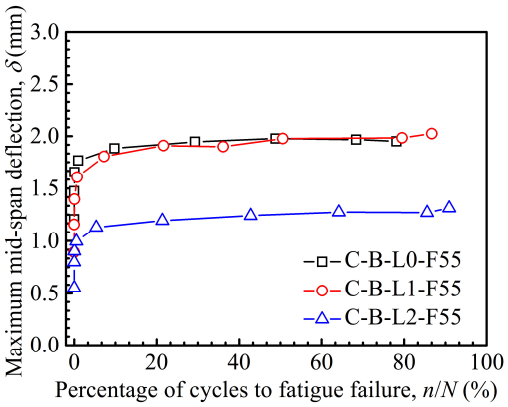

(a) Applied load level of 55%

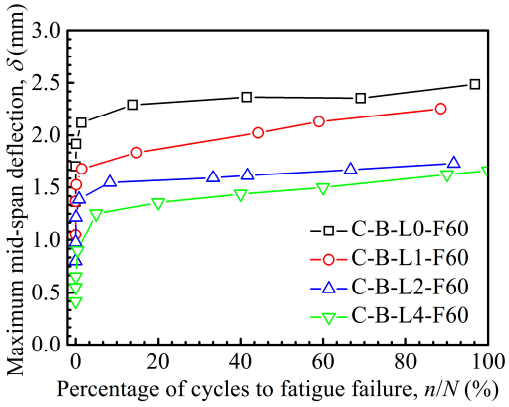

(b) Applied load level of 60%

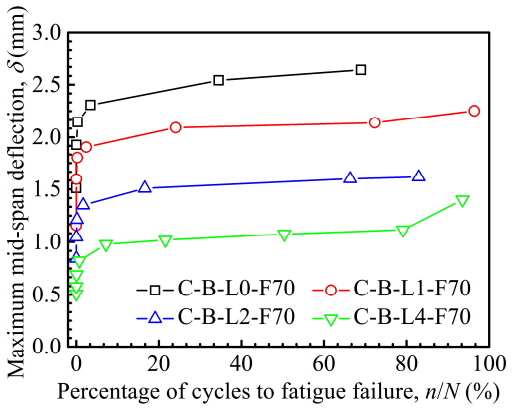

(c) Applied load level of 70%

Fig. 3.11 Maximum mid-span deflection of beams with increasing cycles.

The changes of stiffness of beams are illustrated in Fig. 3.12. The stiffness is obtained by the delta deflections divided by the delta loads between the applied minimum and maximum loads. For most of beams there was an initial decrease of the stiffness followed by a stable region where the stiffness remained almost the same. A significant reduction of stiffness was observed after about 10,000 cycles, and it remained at similar levels regardless of increasing the number of cycles. As expected, during the continued stable development of stiffness, the stiffness of the beams was higher as increasing the layers of CF in the M/C-FRCM. Two beams exhibited different behavior. Regarding the C-B-L4-F60 beam, the stiffness increased gradually until reaching the around 40% of testing cycles after the initial reduction and then continued by a similar stable development until arriving at two million cycles without steel fracture. For the C-B-L4-F70 beam, the stiffness decreased significantly from around 80% of fatigue failure cycles to about 90% of that. The observed debonding of four-layer carbon-FRCM at the mortar-concrete interface was probably the reason for the decrease of stiffness nearby final fatigue failure. However, the ultimate fatigue failure was still controlled by the fracture of steel rebars.

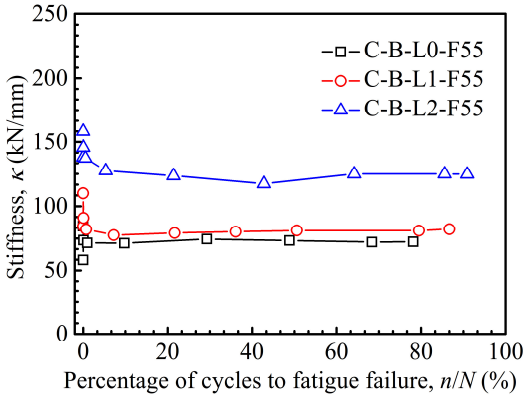

(a) Applied load level of 55%

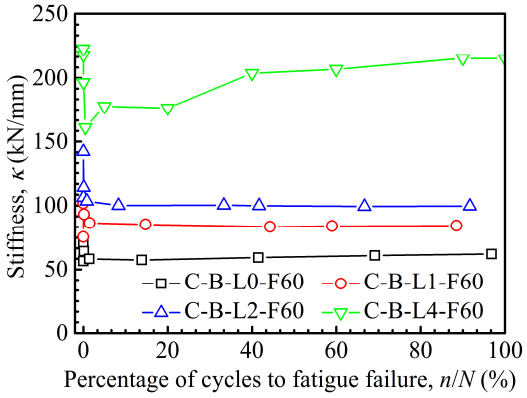

(b) Applied load level of 60%

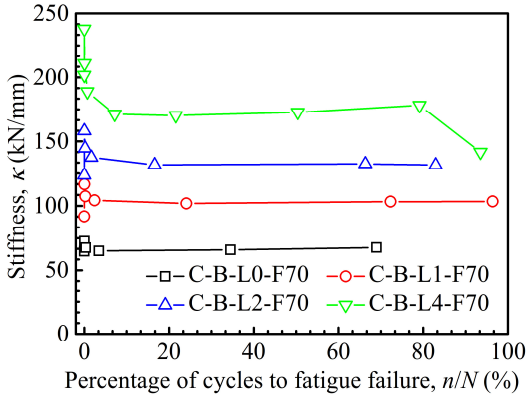

(c) Applied load level of 70%

Fig. 3.12 Stiffness of beams with increasing cycles.

The characteristic of M/C-FRCM for strengthening beams under cyclic loading is presented in Fig. 3.13. The change of maximum deformation of M/C-FRCM was adopted. In this figure, it is obvious that all beams with externally bonded M/C-FRCM behaved in a similar manner. There was an increase in the deformation of M/C-FRCM, followed by a minor increase with increasing the number of cycles. The deformation of four-layer carbon-FRCM in the C-B-L4-F60 beam was less than 0.1 mm until reaching two million cycles without steel fracture. However, the deformation of one-layer carbon-FRCM in the C-B-L1-F70 beam varied greatly. It increased from 0.408 mm at the first cycle to 1.243 mm after 10,000 cycles, and then gradually increased to 1.448 mm after 400,000 cycles. The rupture of steels in the C-B-L1-F70 occurred when the number of cycles achieved at 415,000 cycles. The maximum deformation of carbon-FRCM in the C-B-L1-F70 was close to the cumulative deformation of one-layer carbon-FRCM under cyclic tensile loading (see Fig. 3.5). Regarding other M/C-FRCM composites bonded onto the beams, their maximum deformation ranged between 0.3 mm and 0.7 mm that was much smaller than the cumulative deformation of M/C-FRCM under tensile cyclic loading. It is believed that the M/C-FRCM sustained cyclic load continuously until the steel rupture occurred that caused the consequent extensive slippage of fabric and fiber breakage, as shown in Fig. 3.9 (d) and (e).

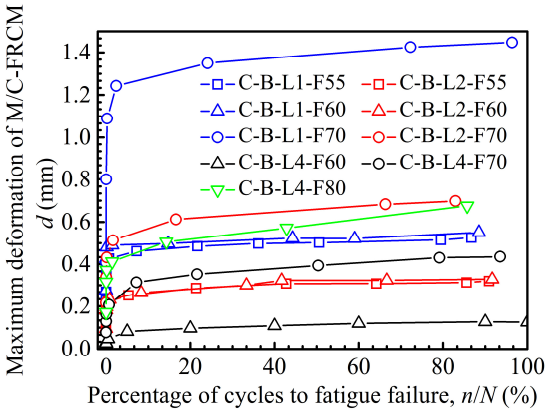

Fig. 3.13 Maximum deformation of M/C-FRCM with increasing cycles.

3.4.3 Fatigue life performance of beams with externally bonded M/C-FRCM

Fig. 3.14 indicates the enhancement of fatigue life of beams with externally bonded M/C-FRCM comparing to the non-strengthened beams at the same applied load levels. The fatigue life increased as increasing the layer of CF in the carbon-FRCM composites. The enhancement ratio was more significant at the higher applied load level. At the applied load level of 70%, the enhancement ratio was 43% in the C-B-L1-F70, 108% in the C-B-L2-F70, and up to 379% in the C-B-L4-F70 beam.

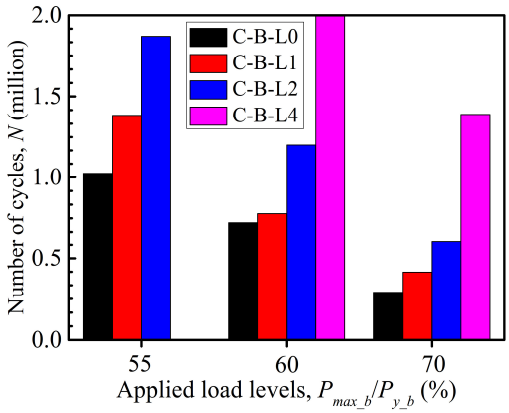

Fig. 3.14 Enhancement of fatigue life by using M/C-FRCM.

Table 3.4 presents the fatigue response of all beams involving the non-strengthened beams and beams with externally bonded M/C-FRCM. According to the applied minimum and maximum load, the corresponding stress of steel rebars and stress of M/C-FRCM can be calculated based on the prediction formulas that were proposed in chapter 2. The enhancement of fatigue life for beams with externally bonded M/C-FRCM was attributed to the reduction of stress of steel rebars in concrete. The reduction of steel stress varied at the strengthening ratio, i.e., the number of layers of CF mesh in the carbon-FRCM composites. The reduction ratio of the stress range of steel was 6.7% on average since one-layer carbon-FRCM was bonded to the beam. This value increased to 14.9% and 26.1% on average when two- and four-layer carbon-FRCM were used. It seems that the reduction ratio of the stress range of steel was proportional to the number of layers of CF in the carbon-FRCM. M/C-FRCM increase the strength and the stiffness of RC beams and consequently reduce the stress of steel rebars in concrete that resulted in prolonging the fatigue life.

Regarding the behavior of M/C-FRCM, the stress range of M/C-FRCM increased as increasing the applied load levels. According to the fatigue life mode of M/C-FRCM that was proposed in the section of 3.3.3 (see Eq. (3.7)), the prediction fatigue life of M/C-FRCM for strengthening beams in this chapter was all over than two million cycles due to the endurance limit stress range of M/C-FRCM is up to 490 MPa. Again, it is proven that the fatigue failure of beams with externally bonded M/C-FRCM was due to the rupture of steel, and no fatigue failure of M/C-FRCM was observed before steel rupture.

Table 3.4 Fatigue response of beams with externally bonded M/C-FRCM.

Beam	P_{min_b} (kN)	P_{max_b} (kN)	$\sigma_{s,min}$ (MPa)	$\sigma_{s,max}$ (MPa)	σ_r (MPa)	$\Delta\sigma_r$ (MPa)	$\sigma_{cf,min}$ (MPa)	$\sigma_{cf,max}$ (MPa)	σ_{cf_r} (MPa)	N_{frcm} (million)	N (million)	Φ_n (%)
C-B-L0-F55	31.3	86.0	98.3	271.2	172.9	/	/	/	/	/	1.024	/
C-B-L0-F60	31.3	93.8	98.3	296.0	197.7	/	/	/	/	/	0.723	/
C-B-L0-F70	31.3	109.4	98.3	345.7	247.4	/	/	/	/	/	0.290	/
C-B-L1-F55	31.3	86.0	83.4	244.4	160.9	12	375.4	673.8	298.4		1.384	35
C-B-L1-F60	31.3	93.8	83.4	267.7	184.3	13.4	375.4	702.8	327.4		0.778	8
C-B-L1-F70	31.3	109.4	83.4	314.9	231.5	15.9	375.4	755.7	380.3		0.415	43
C-B-L2-F55	31.3	86.0	58.6	204.1	145.5	27.4	491.4	822.6	331.2		1.870	83
C-B-L2-F60	31.3	93.8	58.6	226.5	167.9	29.8	491.4	852.4	361	> 2.000	1.200	66
C-B-L2-F70	31.3	109.4	58.6	271.7	213.1	34.3	491.4	905.2	413.8		0.603	108
C-B-L4-F60	31.3	93.8	43.0	187.0	144.0	53.7	337.9	656.5	318.6		2.000	177
C-B-L4-F70	31.3	109.4	43.0	228.5	185.5	61.9	337.9	705.5	367.6		1.390	379
C-B-L4-F80	31.3	125.07	43.0	270.9	228.0	/	337.9	747.9	410		0.700	/

3.5 S-N curves of RC beams with externally bonded carbon-FRCM

The stress states of steel rebars in concrete play the most critical role in assessing the fatigue life performance for either non-strengthened or strengthened beams. Fig. 3.15 presents the fatigue life results of all tested beams in this chapter. The S-N relationship is adopted to assess the effect of steel stress on fatigue life. The stress range (σ_r) is the range of stress of steel rebars between the applied minimum and maximum load under cyclic loading. The number of cycles to failure (N) is plotted on a logarithmic scale. Fig. 3.15 indicates that the fatigue life in logarithm exhibit almost linear increase as reducing the steel stress range. The mathematical regression model for fatigue life prediction is shown in Eq. (3.13).

$$\log N = 7.46 - 0.0079\sigma_r \qquad \text{.....(3.13)}$$

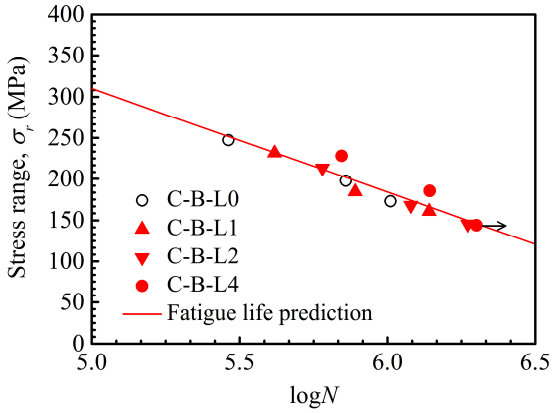

Fig. 3.15 Stress range of steels in concrete versus number of cycles.

Since the FRCM strengthening system is an emerging application, few experiments of RC beams strengthened with FRCM were carried out under cyclic loading. However, the nature of enhancing fatigue life by strengthening is the reduction of stress of steels in concrete. Some S-N curves for fatigue life prediction for strengthened beams were proposed that are based on the established relationship like Eq. (3.13). Moss (1982) suggested an S-N curve based on experimental results of steel rebars tested in RC beams subjected to flexural fatigue loading. The shape of the S-N curve in Eq. (3.14) was different from a linear relationship like Eq. (3.13), but the prediction of fatigue life was always extending by reducing the stress range of steel. Helagson and Hanson (1974) proposed a linear relationship between steel stress range and fatigue life in logarithm that is shown in Eq. (3.15) based on the statistical analysis performed on a database obtained from testing of deformed steel rebars tested axially in air. Subsequently, some other similar prediction models were proposed, such as Eq. (3.16) (Papakonstantinou et al., 2001) and Eq. (3.17) (Katakalos et al., 2009). Besides, from the perspective of fatigue design, ACI 215 (1974) recommends that the permissible stress range of steel should be 138 MPa. Although these prediction models do not explicitly consider the contribution of external bonding reinforcement such as FRP and FRCM composites, they do it implicitly. The prediction models based on the stress range of steels are reasonable for beams with externally bonded M/C-FRCM, given that the fatigue failure of FRCM-strengthened beams is primarily due to the rupture of steel rebars.

$$N\sigma_r^{\,m} = K \quad \text{.....(3.14)}$$

Where N = number of cycles to failure, σ_r = steel stress range, m =empirical constant of 8.7, and K =calibrated constant of 0.59×10^{27}.

$$\log N = 6.969 - 0.0055\sigma_r \quad \text{.....(3.15)}$$

$$\log N = 7.675 - 0.0067\sigma_r \quad \text{.....(3.16)}$$

$$\log N = 9.368 - 0.01\sigma_r \quad \text{.....(3.17)}$$

Table 3.5 collects some fatigue test results of beams with externally bonded fabric reinforcement by using an inorganic matrix. The type of fabric includes the carbon fiber mesh or sheet, PBO mesh, and steel cords mesh. The fact that the mechanical properties of fabric reinforcement and inorganic matrix varied greatly. The experimental results of the present study and the collected tests data (Toutanji et al., 2006; Katalalos et al., 2009; Pino et al., 2017; Akbari et al., 2018) in Table 3.4 were presented in Fig. 3.16. Besides, the fatigue life prediction models (ACI 215, 1974; Helagson and Hanson, 1974; Moss, 1982; Papakonstantinou et al., 2001; Katakalos et al., 2009) and the proposed model in the present study are also plotted in Fig. 3.16. The model proposed by Katakalos et al. (2009) does not seem to provide a safe fatigue prediction due to all the test data in Fig. 3.16 lie to the bottom of the prediction model. On the contrary, an excellent characteristic of fatigue life can be evaluated through the prediction model proposed by Helagson and Hanson (1974). Almost all beams with fabric reinforcement by inorganic matrix failed due to cyclic loading, where the corresponding points to failure lie to the upside of the prediction model as Eq. (3.15). Besides, the endurance stress range of steels in the beams with externally bonded M/C-FRCM is 147 MPa by the extrapolation of Eq. (3.13). Thus, it can be concluded that the current ACI 215 can be used for fatigue design and existing models developed for steel reinforcing bars tested in the air can also be used successfully to predict the fatigue life of RC beams with externally bonded fabric reinforcement by inorganic matrix, which are controlled by the fracture of steels at the soffit of the beam. Besides, the proposed fatigue life model in this chapter (see Eq. (3.13)) can also exhibit an effective fatigue life prediction for beams with externally bonded fabric reinforcement by the inorganic matrix.

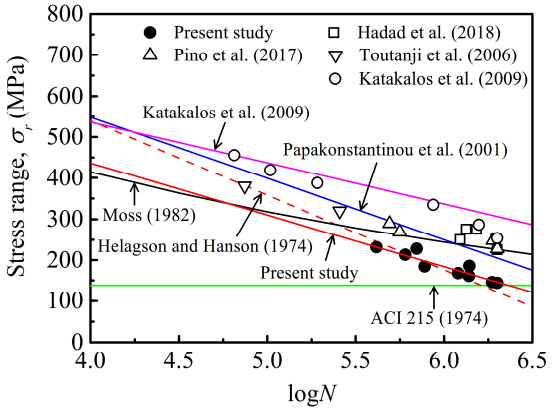

Fig. 3.16 Comparison of stress range of steels in strengthened beams versus number of cycles.

Table 3.5 Fatigue life performance of beams strengthened with various fabric reinforcement bonded by inorganic matrix.

References	Type of fabric	Stress range, σ_r (MPa)	N (million cycles)
Present study	Carbon fiber mesh	160.9	1.384
		184.3	0.778
		231.5	0.415
		145.5	1.870
		167.9	1.200
		213.1	0.603
Akbari et al. (2018)	Carbon fiber mesh	144.0	2.000
		185.5	1.390
		228.0	0.700
		275.7	1.334
		250.6	1.231
		225.5	2.000
		275.67	1.526
		250.6	1.959
		225.5	2.000
Pino et al. (2017)	PBO mesh	289.6	0.492
		268.9	0.562
		248.2	1.890
		227.5	2.000
Toutanji et al. (2006)	Carbon fiber sheet	380.0	0.075
		320.0	0.257
		260.0	2.000
Katalalos et al. (2009)	Steel mesh	253.8	2.000
		286.7	1.575
		334.6	0.870
		387.8	0.192
		418.5	0.104
		455.4	0.065

3.6 Conclusions of this chapter

In this chapter, the fatigue response of M/C-FRCM in tension and beams with externally bonded M/C-FRCM in flexure were studied. The following conclusions can be reached:

(1) The number of layers of CF mesh in the carbon-FRCM did not change the failure mode under cyclic loading. The fatigue failure of M/C-FRCM was the fiber breakage combined with extensive slippage of fibers at the crack of the mortar matrix. The fatigue degradation characteristics of M/C-FRCM were the increase of fabric slippage and the corresponding reduction of stiffness. The aggregation of fiber breakage and decohesion of fibers within the mortar matrix was the fatigue degradation of M/C-FRCM.

(2) The fatigue life model of M/C-FRCM composites was proposed based on the experimental data. By comparing the fatigue life model of M/C-FRCM with that of steel rebars, the fatigue life

performance of M/C-FRCM is superior to the steel rebars. The endurance limit stress range of M/C-FRCM can be up to 490MPa, which is higher than that of steels in fatigue design.

(3) The fatigue strength model of M/C-FRCM was also proposed based on the experimental data. Comparing with CFRP composite material, the fatigue life performance of M/C-FRCM is inferior due to poor impregnation of the mortar matrix into carbon fibers. The fatigue stress limit of M/C-FRCM is recommended to 35% of the ultimate tensile strength.

(4) The emerging carbon-FRCM composites can be used to improve the fatigue performance of RC beams. Still, the level of improvement is largely dependent on the fabric reinforcement ratios of FRCM composites and the applied load levels. The more fabric reinforcement ratio is, the more growth of fatigue life is. At a specified fabric reinforcement ratio, the improvement of fatigue life is more remarkable at the higher fatigue load level due to the significant contribution of FRCM to reducing the stress of steel rebar.

(5) Overall fatigue failure of un-strengthened beams and beams with externally bonded M/C-FRCM was due to fatigue fracture in the steel rebars, and the M/C-FRCM composites did not suffer from fatigue failure before steel fracture. The fatigue degradation characteristics of beams with externally bonded M/C-FRCM were the increasing of the maximum deflection and decreasing of stiffness at the early fatigue and remaining stable at the long period of fatigue loading followed by a detectable sudden change of the deflection and stiffness of RC beams.

(6) The fatigue life prediction model (i.e., S-N curve) for beams with externally bonded M/C-FRCM was proposed based on the experimental data. The endurance limit stress range of steels in the M/C-FRCM strengthened beams was extrapolated to be 147 MPa based on the proposed fatigue life prediction model so that the recommendations in the ACI 215 can be used for fatigue design. By comparing other S-N curves, the proposed S-N curve in this study and Helagson and Hanson's S-N curve can be used successfully to predict the fatigue life of RC beams with externally bonded fabric reinforcement by inorganic matrix, which are controlled by the fracture of steel rebars.

APPENDIX B.1. Load versus deflection hysteresis curves of non-strengthened beams and beams with externally bonded M/C-FRCM

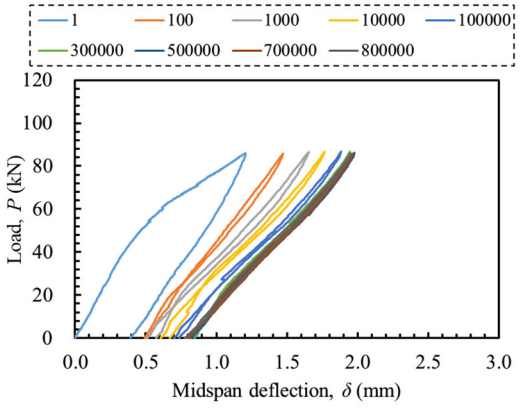

(a) C-B-L0-F55

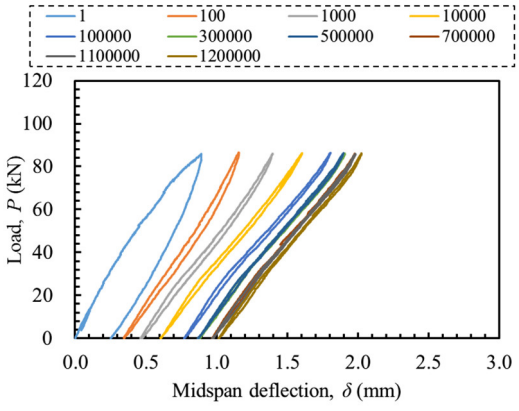

(b) C-B-L1-F55

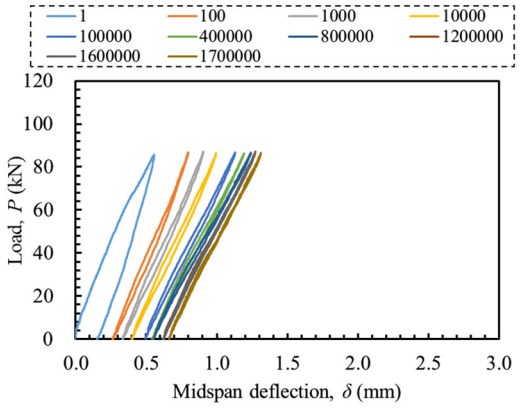

(c) C-B-L2-F55

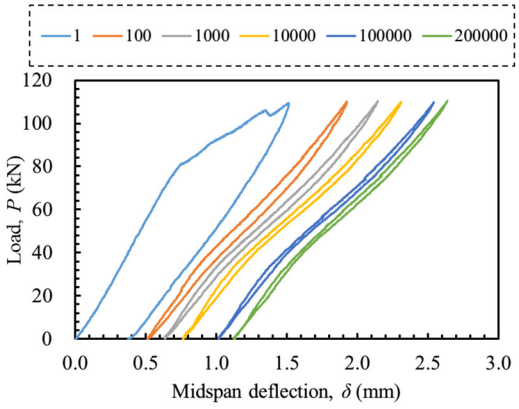

(d) C-B-L0-F70

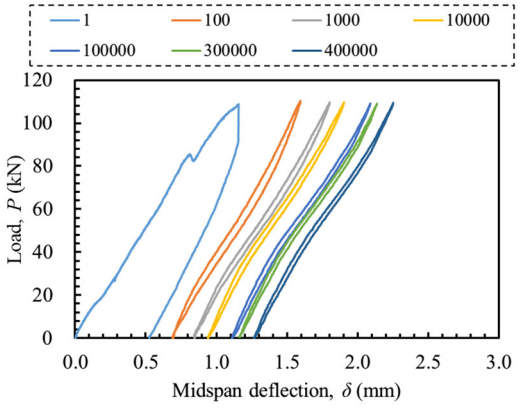

(e) C-B-L1-F70

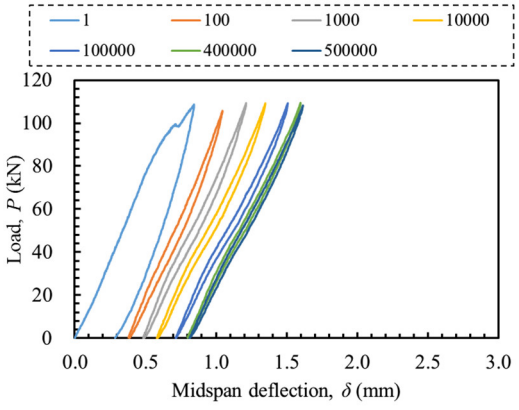

(f) C-B-L2-F70

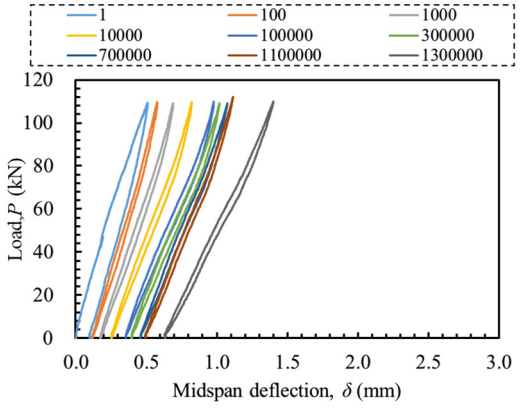

(g) C-B-L4-F70

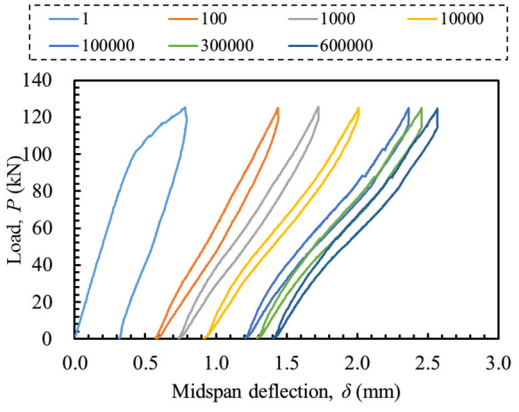

(h) C-B-L4-F80

Fig. B.1.1 Load versus deflection hysteresis curves of beams at the applied load levels of 55%, 70% and 80%.

List of Figures

List of Tables

References

AASHTO, 2017. AASHTO LRFD bridge design specifications, 8th edition. Washington (DC), USA. American Association of State Highway and Transportation Officials.

ACI 215R, 1974. Considerations for design of concrete structures subjected to fatigue loading. ACI 215R-74 (reapproved 1997). Farmington Hills, Mich., USA: ACI.

ACI 440.2R, 2008. Guide for the Design and Construction of Externally Bonded FRP Systems for Strengthening Concrete Structures. American Concrete Institute, U.S.A.

ACI 549.4R, 2013. Guide to design and construction of externally bonded fabric-reinforced cementitious matrix (FRCM) systems for repair and strengthening concrete and masonry structures. American Concrete Institute, U.S.A.

Akbari Hadad, H., Nanni, A., Ebead, U.A. and El Refai, A., 2018. Static and fatigue performance of FRCM-strengthened concrete beams. Journal of Composites for Construction, 22(5), 04018033.

Barnes, R.A. and Mays, G.C., 1999. Fatigue performance of concrete beams strengthened with CFRP plates. Journal of Composites for Construction, 3(2):63-72.

CEB-FIP, fib 2010. Fib model code for concrete structures. International Federation for Structural Concrete, Switzerland.

Degrieck, J. and Van Paepegem, W., 2001. Fatigue damage modeling of fibre-reinforced composite materials. Applied Mechanics Reviews, 54(4), 279-300.

Demers, C.E., 1998. Fatigue strength degradation of E-glass FRP composites and carbon FRP composites. Construction and Building Materials, 12(5), 311-318.

Dong, J.F., Wang, Q.Y. and Guan, Z.W., 2012. Structural behaviour of RC beams externally strengthened with FRP sheets under fatigue and monotonic loading. Engineering Structures, 41, 24-33.

Gheorghiu, C., Labossiere, P. and Proulx, J., 2007. Response of CFRP-strengthened beams under fatigue with different load amplitudes. Construction and Building Materials, 21(4), 756-763.

Helagson, T., and Hanson, J.M., 1974. Investigation of design factors affecting fatigue strength of reinforcing bars-statistical analysis. Special Publication, 41, 107-138.

Katakalos, K. and Papakonstantinou, C.G., 2009. Fatigue of reinforced concrete beams strengthened with steel-reinforced inorganic polymers. Journal of Composites for Construction, 13(2), 103-112.

Lian, W. and Yao, W., 2010. Fatigue life prediction of composite laminates by FEA simulation method. International Journal of Fatigue, 32(1), 123-133.

Moss, D. S., 1982. Bending fatigue of high-yield reinforcing bars in concrete. TRRL Supplementary Rep. No. 748, Transport and Road Research Laboratory, Crowthome, U.K

Pandita, S. D., Huysmans, G., Wevers, M. and Verpoest, I., 2001. Tensile fatigue behaviour of glass plain-weave fabric composites in on-and off-axis directions. Composites Part A: Applied Science and Manufacturing, 32(10), 1533-1539.

Papakonstantinou, C.G., Petrou, M.F. and Harries, K.A., 2001. Fatigue behavior of RC beams strengthened with GFRP sheets. Journal of Composites for Construction, 5(4), 246-253.

Papakonstantinou, C.G., Balaguru, P.N. and Petrou, M.F., 2002. Analysis of reinforced concrete beams strengthened with composites subjected to fatigue loading. ACI Special Publications, 206, 41-60.

Papakonstantinou, C.G. and Balaguru, P.N., 2007. Fatigue behavior of high temperature inorganic matrix composites. Journal of Materials in Civil Engineering, 19(4), 321-328.

Pino, V., Akbari Hadad, H., De Caso y Basalo, F., Nanni, A., Ali Ebead, U. and El Refai, A., 2017. Performance of FRCM-strengthened RC beams subject to fatigue. Journal of Bridge Engineering, 22(10), 04017079.

Sevenois, R.D.B. and Van Paepegem, W., 2015. Fatigue damage modeling techniques for textile composites: review and comparison with unidirectional composite modeling techniques. Applied Mechanics Reviews, 67(2).

Toutanji, H., Zhao, L., Deng, Y., Zhang, Y. and Balaguru, P., 2006. Cyclic behavior of RC beams strengthened with carbon fiber sheets bonded by inorganic matrix. Journal of Materials in Civil Engineering, 18(1), 28-35.

Wu, Z., Wang, X., Iwashita, K., Sasaki, T. and Hamaguchi, Y., 2010. Tensile fatigue behaviour of FRP and hybrid FRP sheets. Composites Part B: Engineering, 41(5), 396-402.

CHAPTER 4

STATIC PERFORMANCE OF RC BEAMS WITH EXTERNALLY BONDED CARBON-FRCM SUFFERING FROM ANODIC POLARIZATION

4.1 Introduction

Although the FRCM composite has a comparable mechanical behavior with FRP, the durability of FRCM exposure to different detrimental environment conditions should also be investigated. Donnini et al. (2017) evaluated the mechanical behavior of carbon-FRCM under high-temperature conditions. The ultimate tensile strength of carbon-FRCM with resin-coated carbon fabric was 27.8% higher than that with dry carbon fabric at room temperature. FRCM reinforced with coated carbon fabric decreased by 70% caused by the deterioration of the resin coating at the interface fiber-matrix when the exposure temperature increased to 80°C and 120°C, while FRCM reinforced with dry fabric has proven not to be affected by temperature up to 120°C. Other exposure environments have also been investigated, such as the resistance of glass-FRCM to alkaline and salt attack (Nobili, 2016; Donnini, 2019) and freeze-thaw durability of lime-based FRCM for strengthening historical masonry (Pekmezci et al., 2019). According to the preliminary experimental investigation (Su et al., 2019, 2020), the superior performance of ICCP-SS has been proven compared to the separate ICCP system and structural strengthening system. However, the influence of anodic polarization in the process of ICCP on the durability of the dual-functional carbon-FRCM composites needs to be taken into consideration. Conceivably, the bond between dry carbon fabric and mortar matrix subjects from the attack caused by the anodically electrochemical process that may also affect the mechanical behavior of carbon-FRCM for strengthening. This kind of study has not yet carried out so that it is first to clarify the durability of carbon-FRCM reinforced with dry carbon fabric exposure to the anodically electrochemical environment. Then, to evaluate the influence of anodically polarized carbon-FRCM on the effectiveness in strengthening beams.

The tensile tests of carbon-FRCM and four-point bending tests of RC beams with externally bonded carbon-FRCM were carried out under static loading in this chapter. Here, the two-layer carbon-FRCM was involved. The materials and preparation of carbon-FRCM for both two experiments were the same as described in section 2.3.1 and section 2.3.2 of chapter 2. Besides. the tensile tests setup and bending tests setup were also the same as presented in section 2.3.3 and 2.3.4 of chapter 2. Particularly, an accelerated electrochemical (AC-EC) test of carbon-FRCM was conducted before performing the tensile tests and strengthening RC beams in this chapter. Thus, the AC-EC tests program is introduced in this chapter.

4.2 Experimental program

4.2.1 Electrochemical tests of carbon-FRCM

AC-EC tests setup

For the study of tensile behavior of carbon-FRCM, it is not possible to conduct tensile tests of the carbon-FRCM specimens after bonding to concrete since it is rather difficult to remove the intact carbon-FRCM; therefore, a well-designed accelerated electrochemical (AC-EC) test was adopted

to investigate the influence of anodic polarization on the tensile behavior of carbon-FRCM when it was used as anode material in the ICCP system. Fig. 4.1 shows an AC-EC test of large size square carbon-FRCM panel that would be cut into small specified specimens for tensile tests. Note that all composites were two-layer carbon-FRCM when suffered from anodic polarization in the AC-EC tests in which it was termed as anodically polarized carbon-FRCM (AP/C-FRCM). At first, six deformed steel rebars with diameters of 12 mm, which were placed at intervals of 100 mm, were fixed at the vertical center of the wooden mould; and then, the mould with steel rebars was placed at the surface of the carbon-FRCM panel. The longitudinal direction of the rebars was parallel to the primary direction of the carbon fiber bundles. All joints were bonded and blocked off with a silica gel. All sides in the thickness of the carbon-FRCM panel were coated with a polymeric resin. Subsequently, saturated $Ca(OH)_2$ solution was added into the mould, filling more than 80% in volume of the mould. Finally, the steel rebars were chained together and connected to the negative terminal of a direct current (DC) power supply, while the top layer of the CF mesh close to the solution was connected to the positive terminal of the DC power supply. Stainless-steel strips were used to form an electrically conductive pathway between the CF bundles in the primary and secondary directions at the top layer of CF mesh. Besides, the steel rebars in the mould maintained to be submerged by adding saturated $Ca(OH)_2$ solution to counteract the evaporation of water. In the AC-EC test setup, the saturated $Ca(OH)_2$ solution assumed the role of the concrete, the steel rebars soaking in the solution served as the corroded steel reinforcement requiring protection in the concrete, and the carbon-FRCM composite acted as the anode material.

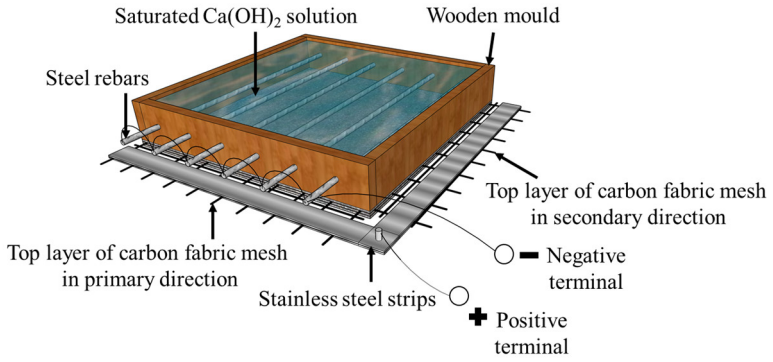

Fig. 4.1 An AC-EC test of carbon-FRCM for material preparation of tensile tests.

For the study of the structural behavior of the ICCP-SS intervened beams where the carbon-FRCM suffered from anodic polarization, a similar AC-EC test setup was adopted. In other words, the carbon-FRCM suffered from anodic polarization firstly, and then externally bonded to the soffit of beams, after that the four-point bending tests were conducted. This procedure can prevent the steel rebars and/or bond interface in concrete from deterioration in accelerated ICCP system so that the evolution of structural behavior of strengthened beams in the ICCP-SS system can be assumed to the contribution of the carbon-FRCM composite.

Fig. 4.2 shows an AC-EC test of large size carbon-FRCM panel that would be cut into small specified plates for externally bonding to the soffit of beams followed by the four-point bending tests. Likewise, the two-layer carbon-FRCM composites were adopted when they suffered from anodic polarization before bonding to the beams. Since the length of the carbon-FRCM panel was longer, the clamps were used to clip tight between the stainless-steel strips and CF mesh to maintain

the good conductive path in the anode system.

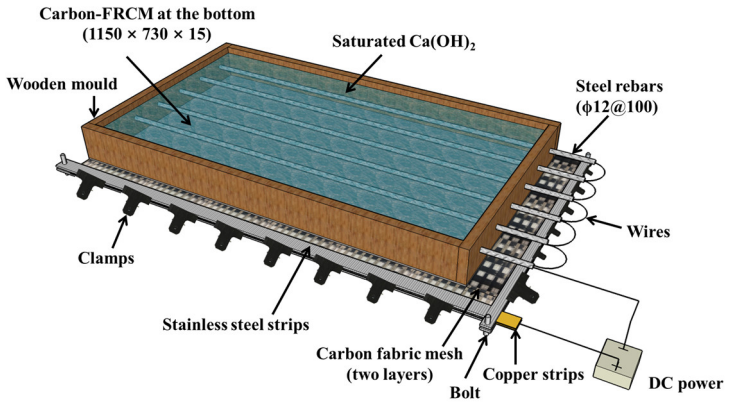

Fig. 4.2 An AC-EC test of carbon-FRCM for material preparation of strengthening beams.

Current density

The laboratory accelerated test method was adopted to investigate the influence of anodic polarization in ICCP on either the tensile behavior of carbon-FRCM or structural strengthening of beams. The AC-EC tests were performed by applying current densities that were higher than the typical current densities in practical ICCP application. The current density is defined as the current to or from a unit area of an electrode surface (NACE SP0169, 2007). It is the cathodic current density for the cathode electrode, such as steel reinforcement in concrete, while it is the anodic current density for the anode electrode in the ICCP system.

In terms of steel reinforcement in concrete, the recommended cathodic current densities were limited between 0.2 and 2 mA/m^2 for cathodic prevention technique, while ranging from 2 to 20 mA/m^2 for cathodic protection technique (Pedeferri, 1996; Bertolini et al. 1998). The corrosion of steels might not be protected if the applied cathodic current density was too lower, whereas the steels might suffer from hydrogen embrittlement if the applied cathodic current density was too higher. On the other hand, in terms of anode material, the maximum anodic current densities are limited below 108 mA/m^2 to prevent deterioration of concrete at the anode-concrete interface (NACE SP0290, 2007). This is an explanation for adopting the accelerated electrochemical (AC-EC) tests in the study of the structural behavior of ICCP-SS intervened beams.

Therefore, four different levels of anodic current densities (i_a) were considered in the AC-EC tests of carbon-FRCM composites: 125 mA/m^2, 375 mA/m^2, 500 mA/m^2, and 750 mA/m^2, respectively. The anodic current density is calculated by Eq. (4.1). The area of carbon fabric mesh (A_a) is defined as the geometric surface area of carbon fiber bundles in the two sides of one layer of CF mesh embedded in the mortar matrix. Through the analysis of image processing, the percentage of the geometric surface area of carbon fiber bundles on the one side is approximately 57.6% of the total surface area of CF mesh that includes the area of spacing between bundles (i.e., equal to 42.4%). A_a was calculated to 0.415 m^2 in the square carbon-FRCM panel (i.e., Fig. 4.1), while 0.862 m^2 in the rectangle carbon-FRCM panel (i.e., Fig. 4.2). The constant currents (I) were applied in the ICCP system.

$$i_a = I / A_a \qquad \text{.....(4.1)}$$

Signals during the AC-EC tests

During the AC-EC tests, the potentials of the steel rebars and the CF mesh were measured using an Ag/AgCl reference electrode (RE), as shown in Fig. 4.3(a). The RE was touched on the surface of carbon-FRCM in the saturated $Ca(OH)_2$ solution, as shown in Fig. 4.3(b), and connected to the positive terminal of data logger system, while the steel rebars were connected to the negative terminal of data logger system when the potentials of steel rebars were measured, and the CF mesh was connected to the negative terminal of that when its potentials were measured. Besides, the feeding voltages between the CF mesh and the steel rebars were also measured. All signals of both potentials and voltages were recorded by the data logger system, as shown in Fig. 4.3(c). The AC-EC tests were performed to approximately 60 days, and the potentials and voltages were tracked throughout. Moreover, it was necessary to calculate the accumulated charge densities (q) when the AC-EC tests finished. This value could be obtained from Eq. (4.2), which is the product of the anodic current density and the test duration (t).

$$q = i_a \times t \qquad \text{.....(4.2)}$$

(a) Ag/AgCl reference electrode

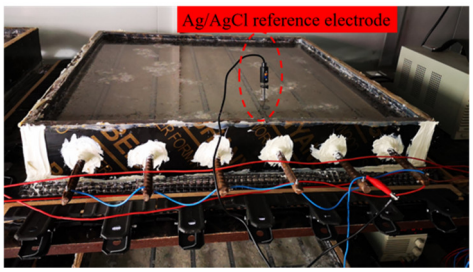

(b) measuring method of potentials

(c) data logger system

Fig. 4.3 Measurement of signals of voltages and potentials during the AC-EC tests.

4.2.2 Static tensile tests program of AP/C-FRCM

Table 4.1 presents the AP/C-FRCM specimens involved in the static tensile tests. A total of 12 two-layer carbon-FRCM specimens were prepared. The labeling of the carbon-FRCM specimens in this chapter was termed starting with S-T (static tensile loading), followed by AP (anodic polarization) and the applied anodic current densities (i.e., i125, i375, i500, and i750).

Table 4.1 AP/C-FRCM specimens in the static tensile tests.

Carbon-FRCM specimens	Layer of CF mesh	Size of carbon-FRCM	Current density, i_a (mA/m^2)
S-T-AP-i125	2	600×100×15	125
S-T-AP-i375	2	600×100×15	375
S-T-AP-i500	2	600×100×15	500
S-T-AP-i750	2	600×100×15	750

4.2.3 Static bending tests program of RC beams with externally bonded AP/C-FRCM

Table 4.2 shows the beams tested in the static four-point bending tests. A total of 4 beams were prepared. The labeling of beams was termed starting with S-B (static bending loads), followed by AP (anodic polarization) and the applied anodic current densities (i.e., i125, i375, i500, and i750).

Table 4.2 RC beams strengthened with AP/C-FRCM in the static bending tests.

Beams	Layer of CF mesh	Size of carbon-FRCM	Current density, i_a (mA/m^2)
S-B-AP-i125	2	1100×100×15	125
S-B-AP-i375	2	1100×100×15	375
S-B-AP-i500	2	1100×100×15	500
S-B-AP-i750	2	1100×100×15	750

4.3 AC-EC test results and discussion

4.3.1 Feeding voltages and electrode potentials

Fig. 4.4 shows the results of the feeding voltage (E_{feed}) between the carbon-FRCM and the steel cathode, the anode potential (E_{an}), and the steel potential (E_{cat}) as a function of the testing time. The instant-off steel potentials (E_{cat}) in all specimens were more negative than -800 mV with respect to the Ag/AgCl RE. According to BS EN 12696 (2016), the results of E_{cat} meet the criteria for the successful protection of steels in concrete, which indicates the efficiency of ICCP using carbon-FRCM as an anode material. A constant current density of 125 mA/m^2 was applied continuously in the S-T-AP-i125 specimen, in which both E_{feed} and E_{an} increased gradually as the testing time increased. The feeding voltage in the S-T-AP-i125 specimen started at 1.74 V and ended at 8.30 V. Compared with the results of the S-T-AP-i125 specimen, a higher rate of increase in the feeding voltage was found in the S-T-AP-i375, S-T-AP-i500, and S-T-AP-i750 specimens during the first month (see Fig. 4.4(b)-(d)). Although the current density was subsequently reduced to 125 mA/m^2 in the S-T-AP-i375, S-T-AP-i500, and S-T-AP-i750 specimens, the increasing rate in the feeding voltage did not slow in these specimens. Constant currents were applied in the ICCP system so that the change of feeding voltages could be a representative factor of electrical resistance of the system. It is possible that some deterioration could have occurred in the carbon-FRCM composites.

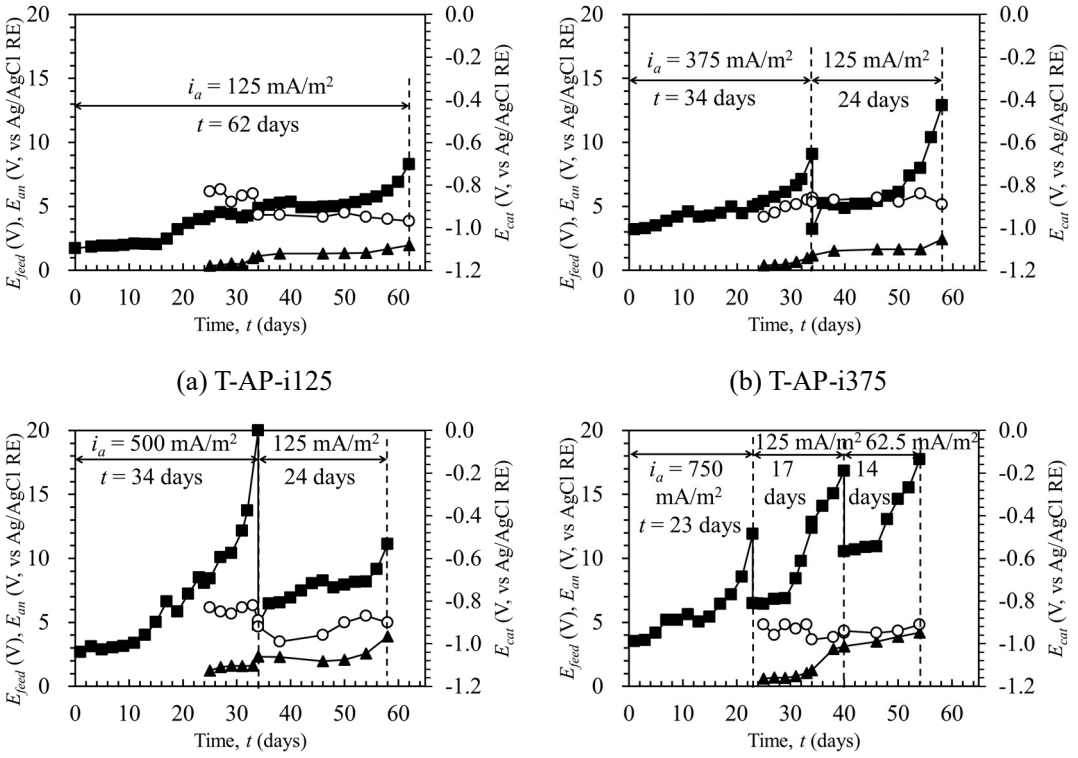

(a) T-AP-i125 (b) T-AP-i375

(c) T-AP-i500 (d) T-AP-i750

Fig. 4.4 Feeding voltage (■, E_{feed}), anode potential (▲, E_{an}) and steel potential (○, E_{cat}) in the period of AC-EC test.

4.3.2 Acidification phenomenon

When the AC-EC tests were finished after approximately two months, macroscopic deterioration was observed in the vicinity of the top layer of carbon fabric mesh, as shown in Fig. 4.5. The lateral section of the carbon-FRCM subjected to a current density of 375 mA/m^2 was sprayed with a phenolphthalein indicator to investigate the causes of deterioration. The phenolphthalein indicator is a kind of colorless solution. If the color of the surface of carbon-FRCM tended to be red or pink after spraying the phenolphthalein, it indicates the carbon-FRCM was remaining alkaline. However, if the surface was colorless, it means the surface of carbon-FRCM changed to be acid. Fig. 4.5 shows visual acidification that was detected around the carbon fiber bundles in the top layer. Similar deterioration was also found in the other specimens subjected to anodic polarization in the period of AC-EC tests. This phenomenon can be explained by the anodic reactions occurring at the interface between the carbon fibers and the mortar matrix, as shown in Eq. (4.3) (Bertolini et al., 2004). In these zones, the conductive cement-based mortar matrix and carbon fiber bundle appeared to be damaged (see Fig. 4.5), which could result in the loss of electrical continuity between them; hence, the increasing feeding voltage could be caused by the loss of electrical continuity (Bertolini et al., 2004). Thus, the feeding voltage can be assumed as an implicit parameter to evaluate the damage of the carbon-FRCM as an anode material in the ICCP-SS system.

$$2\,H_2O - 4\,e^- \rightarrow 4\,H^+ + O_2 \qquad \text{.....(4.3)}$$

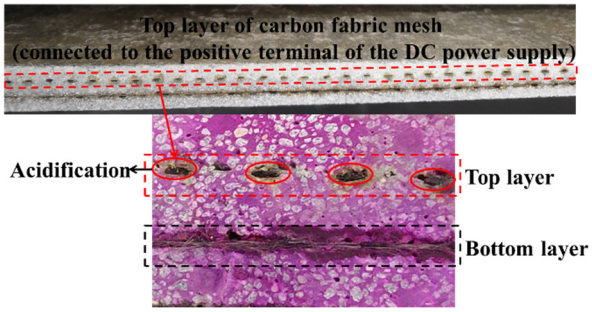

Fig. 4.5 Acidification detection around the CF mesh.

4.3.3 Discussion on the utilization period

Note that ICCP had protected some concrete structures for several years, such as the Yaquina Bay Bridge in Newport, Oregon (Cramer et al., 2002a), and the Sydney Opera House (Tettamanti, 1997), etc. To improve safety on-site, some preventative measures such as barriers, obstacles, or electrical insulation could be provided. More importantly, it is worthwhile to note that the total output from the power supply shall not exceed 50 V, and the output from the power supply unit is limited not to exceed 24 V (BS EN 12696, 2016). Thus, if the ICCP system complies with the design requirement in the standards, it is expected to be safe in the field condition.

In general, the current densities in practical ICCP for concrete structures are limited between 0.2 and 2 mA/m^2 for cathodic prevention and between 2 and 20 mA/m^2 for cathodic protection (Pedeferri, 1996). To investigate the long-term performance of carbon-FRCM as a dual-functional material in ICCP-SS within an adequate testing time in the laboratory, the adopted current densities of 125, 375, 500, and 750 mA/m^2 in this chapter accelerate the ICCP procedure. Research has been conducted to determine the relationship between accelerated tests using a large current density and practical conditions using a small current density. Chang et al. (1999) proposed converting the accelerated and practical conditions by the principle of the equal cumulative quantity of charge, wherein if the cumulative charge in the accelerated and practical conditions are the same, as shown in Eq. (4.4). It was assumed that the polarization effects are identical. This relationship has been adopted in many studies for accelerated tests (Anwar et al., 2014; Cramer et al., 2002b). Recently, Zhang et al. (2018) reported that a large current density had overestimated effects on the degradation of anode materials. It was concluded that using the principle of equal cumulative charge in accelerated tests will obtain more severe degradation than that from the practical condition (Zhang et al., 2016; 2018). It is true that the precise relation between the accelerated and normal conditions is still an ongoing research topic, although accelerated test methods have been used in the long-term cathodic protection and polarization studies.

An assessment of the optimal utilization period of the carbon-FRCM composites used in the ICCP-SS was conducted based on the principle of equal cumulative charge, as shown in Eqs. (4.4) – (4.6). The utilization period of carbon-FRCM represents the optimal period of carbon-FRCM considering both the mechanical properties and anodic performance in the ICCP-SS system. Taking the S-T-AP-i375 specimen into consideration, the total charge density was 15750 mA-d/m^2. If current densities of 2 and 20 mA/m^2 are applied in practical ICCP based on the specification in BS EN 12696 (2016), the convertible utilization period could be approximately 21.6 and 2.2 years, respectively, which means that the carbon-FRCM could maintain the tensile strength and strain for

strengthening when used as an anode in ICCP over a range of 2.2 to 21.6 years. And then, beyond the predicted utilization period, the rehabilitated structures with the ICCP-SS system must be assessed once again to determine reasonable measures, continue using the original carbon-FRCM, or replacing a new carbon-FRCM composite. The optimal utilization period of the dual-functional carbon-FRCM composite could be longer due to overestimated degradation in the accelerated tests.

$$Q_{test} = Q_{real} \quad \text{.....(4.4)}$$

$$Q_{test} = Q_{test\_i375} \quad \text{.....(4.5)}$$

$$Q_{real} = i_{real} \times t_{util} \quad \text{.....(4.6)}$$

Where Q_{test} is the total cumulative charge in the AC-EC tests conducted in the laboratory; Q_{real} is the total cumulative charge in the practical ICCP application in situ; Q_{test_i375} is the total cumulative charge of S-T-AP-i375 specimen; i_{real} is the current density applied in the practical ICCP application; t_{util} is the predicted utilization period of carbon-FRCM composite in situ.

Besides, methods are available to improve the ICCP scheme to extend the utilization period of dual-functional composites. For instance, intermittent ICCP (Glass et al., 2001) is a useful technique for balancing the efficiency of cathodic protection and the degradation of mechanical properties. Intermittent ICCP is a kind of strategy of cathodic protection for preventing steel rebars in concrete from corrosion in which the protection currents are occasionally rather than continuously applied (Byrne et al., 2016). The intermittent ICCP is developed due to the contribution of both the re-alkalization of the steel-concrete interface and aggressive ions such as chloride away from the steel when ICCP is “on” period (Byrne et al., 2016). During the ICCP “off” period, chloride ions present in the concrete disrupt the passive film to accelerate the corrosion reaction, lower the steel-concrete interfacial pH, and move the steel potential into the corrosion region. Under these conditions, the corrosion current will increase, eventually requiring the re-application of ICCP to the rebar. However, Christodoulou et al. (2010) found that when ICCP was “off” after five or more years, the steel rebars remained passive for another year. Therefore, the effect of the successful application of intermittent ICCP will be a decrease in the average current density for the ICCP system and as an associated increase in the utilization period of anodes material. This is also meaningful to the full fatigue life performance of concrete structures such as RC beams discussed in the next chapter. It will be a continuous research to seek for a balance between the effective utilization period of ICCP system and structural performance (i.e., fatigue issue) in the application of ICCP-SS intervention system.

4.4 Tensile test results and discussion

4.4.1 Effect of anodic polarization

Table 4.3 summarizes the tensile test results of AP/C-FRCM specimens under static loading, including the experimental tensile load and deformation values at the occurrence of the first crack on the mortar matrix and ultimate load and deformation. The pre-cracking and post-cracking tensile stiffness are also involved. Fig. 4.6 compares the tensile load-deformation relation of carbon-FRCM suffering from the anodically electrochemical process. All the carbon-FRCM specimens are two-

layer composites, so that the experimental results of S-T-L2 specimens are involved in Fig. 4.6 to evaluate the effect of anodic polarization on tensile behavior. The negligible influence of anodic polarization on the pre-cracking tensile behavior was observed. However, significant degradation of the post-cracking tensile behavior was found, which depends on the charge densities in the AC-EC tests. The ultimate tensile load of carbon-FRCM dropped by 25.5% in S-T-AP-i125, 50.2% in S-T-AP-i375, 60.6% in S-T-AP-i500, and 54.9% in S-T-AP-i750. The ultimate tensile deformation of carbon-FRCM decreased from 2.577 mm in S-T-L2 to around 1.500 mm in all AP/C-FRCM specimens, except S-T-AP-i750 at the ultimate deformation of 0.413 mm. It was found that strain-hardening behavior in carbon-FRCM composite become mild since the charge density increased in the AC-EC tests. The tensile failure modes of AP/C-FRCM were identical to the non-polarized carbon-FRCM (i.e., S-T-L2 specimens). The decrease of the ultimate tensile load of AP/C-FRCM was attributed to the reduction of bond strength between CF mesh and mortar matrix when the anodic reactions occurred at the carbon-FRCM in the AC-EC tests. The C-S-H gel around the carbon fibers reduced due to the calcium depletion because of the impressed current (Zhang et al., 2018).

Table 4.3 Experimental results of AP/C-FRCM specimens under static tensile loading.

Carbon-FRCM specimens	F_{cr_frcm} (kN)	d_{cr_frcm} (mm)	k_{cr_frcm} (kN/mm)	F_{u_frcm} (kN)	d_{u_frcm} (mm)	k_{u_frcm} (kN/mm)
S-T-AP-i125-1	7.345	0.024	304	11.408	1.270	3.261
S-T-AP-i125-2	6.377	0.025	254	10.887	1.463	3.137
S-T-AP-i125-3	8.661	0.024	355	11.547	1.656	1.768
Average	7.461	0.025	304	11.281	1.463	2.722
Cov	0.154	0.021	0.167	0.031	0.132	0.304
S-T-AP-i375-1	6.360	0.025	254	7.800	1.270	1.157
S-T-AP-i375-2	6.819	0.021	326	7.278	1.755	0.264
Average	6.590	0.023	290	7.539	1.513	0.711
Cov	0.049	0.129	0.178	0.049	0.227	0.888
S-T-AP-i500-1	4.122	0.015	272	6.455	1.775	1.326
S-T-AP-i500-2	3.624	0.029	125	5.482	1.585	1.194
Average	3.873	0.022	198	5.968	1.680	1.260
Cov	0.091	0.442	0.522	0.115	0.080	0.074
S-T-AP-i750-1	4.436	0.025	172	5.467	0.416	5.720
S-T-AP-i750-2	6.242	0.032	122	8.196	0.410	5.210
Average	5.339	0.029	147	6.831	0.413	5.465
Cov	0.239	0.191	0.243	0.283	0.009	0.066

Note: F_{cr_frcm} = load at the occurrence of the first crack on the mortar matrix; d_{cr_frcm} = deformation corresponding to F_{cr_frcm}; δ_{cr_frcm} = pre-cracking stiffness; F_{u_frcm} = ultimate load; d_{u_frcm} = ultimate deformation; δ_{u_Frcm} = post-cracking stiffness.

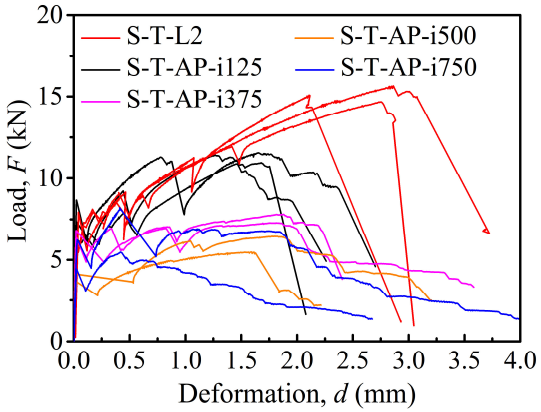

Fig. 4.6 Tensile load vs. deformation of AP/C-FRCM specimens.

4.4.2 Tensile stress-strain relation

According to the calculation procedure described in section 2.4.2 of chapter 2, the experimental tensile stress-strain curves of AP/C-FRCM are presented in Fig 4.7. In the light of AC434 (2016), some critical factors in the calculated tensile stress-strain relation are shown in Table 4.4, and the comparison of the calculated stress-strain relationship of AP/C-FRCM composite specimens is presented in Fig 4.8. The average maximum tensile strength of S-T-AP-i125, S-T-AP-i375, S-T-AP-i500, and S-T-AP-i750 were 1222.0 MPa, 816.7MPa, 646.5MPa, and 740.0 MPa, respectively. The maximum utilization efficiency δ_{cf} was S-T-AP-i125 at the percentage of 57.5%, while the minimum δ_{cf} was S-T-AP-i500 at 30.4%. Comparing to S-T-L2 at the δ_{cf} of 77.2%, the δ_{cf} reduced by around 20% when the anodic current density of 125 mA/m^2 was applied in the AC-EC tests for 62 days. The experimental ultimate tensile strain of AP/C-FRCM decreased from around 1.25% in S-T-L2 to the level of less than 1.0%. Notably, the experimental ultimate tensile strain of S-T-AP-i750 was only about 0.25%, which indicates the large current density caused more severe degradation of tensile behavior of carbon-FRCM suffering from the anodically electrochemical process.

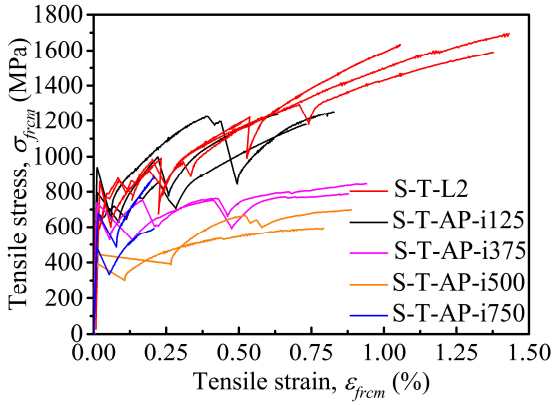

Fig. 4.7 Experimental tensile stress-strain relation of AP/C-FRCM specimens.

Table 4.4 Tensile properties of AP/C-FRCM based on the guideline AC434 (2016).

Carbon-FRCM Specimen	σ_{cr_frcm} (MPa)	ε_{cr_frcm} (%)	E_{frcm}^{*} (GPa)	σ_{u_frcm} (MPa)	ε_{u_frcm} (%)	E_{frcm} (GPa)
S-T-AP-i125-1	638.0	0.010	6624.2	1235.8	0.574	106.0
S-T-AP-i125-2	670.3	0.012	5532.4	1179.3	0.729	71.0
S-T-AP-i125-3	713.0	0.009	7757.7	1250.8	0.830	65.5
Average	673.8	0.010	6638.1	1222.0	0.711	80.8
Cov	0.056	0.153	0.168	0.031	0.182	0.272
S-T-AP-i375-1	504.7	0.009	5521.2	845.0	0.706	48.9
S-T-AP-i375-2	465.6	0.007	7120.4	788.4	0.713	45.7
Average	485.2	0.008	6320.8	816.7	0.709	47.3
Cov	0.057	0.235	0.179	0.049	0.008	0.048
S-T-AP-i500-1	258.3	0.004	5898.5	699.2	0.730	60.8
S-T-AP-i500-2	295.6	0.011	2717.2	593.8	0.579	52.5
Average	276.9	0.008	4307.9	646.5	0.655	56.6
Cov	0.095	0.602	0.522	0.115	0.163	0.104

Note: σ_{cr_frcm} = Cracking stress; ε_{cr_frcm} = Cracking strain; E_{frcm}^{*} = Modulus of elasticity of uncracked carbon-FRCM; σ_{u_frcm} = Ultimate stress; ε_{u_frcm} = Ultimate strain; E_{frcm} = Modulus of elasticity of cracked carbon-FRCM.

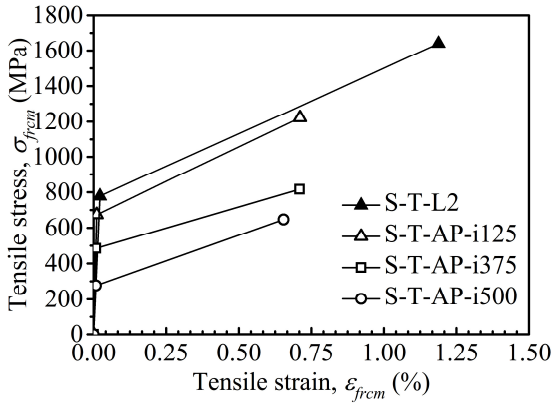

Fig. 4.8 Calculated tensile stress-strain relation of AP/C-FRCM composites.

Fig. 4.8 indicates that the degradation of the constitutive mechanism caused by anodic polarization in the electrochemical process not only in the cracked tensile strength and ultimate tensile strength but also the ultimate tensile strain. The calculated ultimate tensile strain of carbon-FRCM decreased from 1.19% in S-T-L2 to the range between 0.66% and 0.71% in S-T-AP-i125, i375 and i500 specimens. The S-T-AP-i750 was out of comparison because its ultimate tensile strain was incomparable to the other specimens. Fig. 4.9 demonstrates the relationship between the reduction of the tensile strength of AP/C-FRCM and accumulated charge densities (q) in the electrochemical process. Within the accumulated charge densities of 2.0×10^6 C/m^2, the ultimate tensile strength of AP/C-FRCM can be predicted based on the Eq. (4.7).

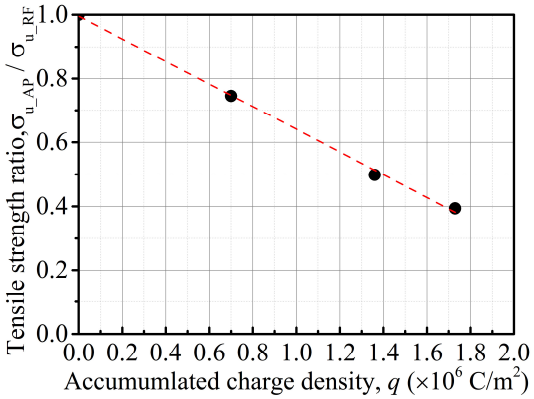

Fig. 4.9 Influence of charge density on degradation of carbon-FRCM in tensile strength.

$$\sigma_{u\_AP} = (-0.35q + 1)\sigma_{u\_RF} \quad \text{.....(4.7)}$$

Where: σ_{u_AP} = tensile strength of AP/C-FRCM; σ_{u_RF} = tensile strength of referenced carbon-FRCM with the identical fabric reinforcement ratio; q = accumulated charge densities in the electrochemical process, unit in $\times 10^6$ C/m^2.

4.4.3 Apparent strain of CF mesh in AP/C-FRCM

Fig. 4.10 shows the effect of anodic polarization on the apparent strain of CF mesh in the carbon-FRCM composites. Different anodic polarization caused the reduction of the apparent strain of CF mesh at the same average strain of carbon-FRCM. Considering the prediction model proposed in section 2.4.3 of chapter 2, the fitting results of α, β, and γ are presented in Table 4.5. Compared to S-T-L2, the fitting parameter β is comparable, while the fitting parameters α and γ are smaller in AP/C-FRCM, and both parameters decreased as the charge densities increased in the electrochemical process. The relation of both fitting parameters α and γ with regards to the accumulated charge densities is shown in Fig. 4.11. Therefore, the apparent strain of CF mesh in the AP/C-FRCM can be predicted in Eqs. (4.8) – (4.10). With regarding the tensile strength of dry carbon fiber bundles, the utilization efficiency of fibers decreased from 76% in the S-T-L2 to 61% in the S-T-AP-i125, 41% in the S-T-AP-i375 and 35% in the S-T-AP-i500.

Table 4.5 Fitting parameters between the apparent strain of CF mesh and measured global strain of AP/C-FRCM.

Specimens	α	β	γ
S-T-L2	0.158	0.011	0.728
S-T-AP-i125	0.142	0.007	0.658
S-T-AP-i375	0.089	0.004	0.443
S-T-AP-i500	0.083	0.007	0.387

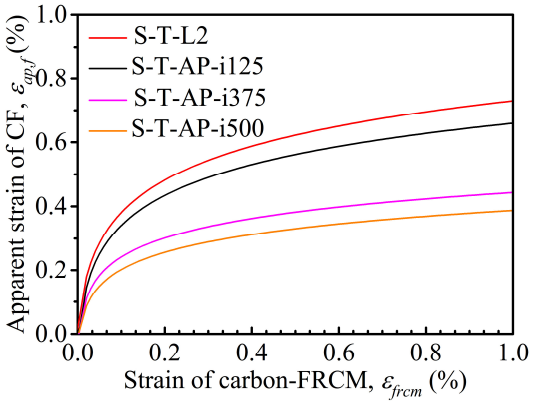

Fig. 4.10 Comparison of apparent strain of CF mesh in AP/C-FRCM composites.

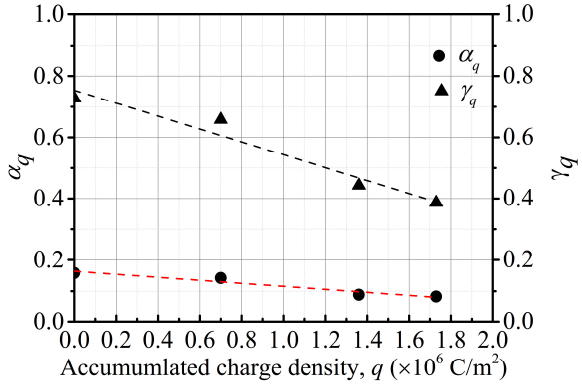

Fig. 4.11 Fitting parameters α and γ with regards to accumulated charge densities.

$$\varepsilon_{ap,f} = \alpha_q \ln\left(\varepsilon_{frcm} + \beta\right) + \gamma_q \quad \text{.....(4.8)}$$

$$\alpha_q = -0.048q + 0.163 \quad \text{.....(4.9)}$$

$$\gamma_q = -0.211q + 0.754 \quad \text{.....(4.10)}$$

Where: α_q and γ_q = fitting parameters account for the accumulated charge densities in the electrochemical process; $\beta = 0.007$, which is an average value.

4.5 Bending test results and discussion

4.5.1 Failure modes of beams with externally bonded AP/C-FRCM

The two-layer carbon-FRCM was bonded to the soffit of the beam after the carbon-FRCM was suffering from the pre-determined anodic polarization in the AC-EC tests. Fig. 4.12 presents the failure modes of beams with externally bonded AP/C-FRCM. Compared with the S-B-L2 beam, the similar failure mode was observed for S-B-AP-i125 and S-B-AP-i375 beams that were the fabric slippage within the mortar matrix followed by the concrete crushing at the extreme compression

zone (FS+CC). The fabric slippage was also observed in the S-B-AP-i500 beam, and the ultimate load-carrying capacity was recorded at the failure of FS instead of concrete crushing. The phenomenon of fabric slippage in the carbon-FRCM was observed since the concrete cracked until final failure, where the rupture of carbon fabric did not occur. The major crack gradually propagated towards the top side of the beam as increasing the applied load in a static loading way. No delamination of carbon-FRCM was observed, except for the S-B-AP-i750 beam. In Fig. 4.12(d), the debonding at the mortar matrix and concrete interface plane was observed in the S-B-AP-i750. The debonding occurred at the cut-off ends of the carbon-FRCM that were nearby the two supports of the simply supported beam. The fabric slippage within the mortar matrix was also observed in the middle pure bending zone, and the debonding of carbon-FRCM was observed after cracking of concrete. The debonding reduced the bond length of carbon-FRCM for strengthening. Finally, the concrete crushing at the extreme compression zone resulted in the final failure of the beam. No debonding of carbon fabric was observed at the fabric-mortar interface plane for all beams with externally bonded AP/C-FRCM. The characterization of bonding between carbon fabric and mortar was not susceptible to the anodic polarization when it was used for strengthening even though a distinct degradation of AP/C-FRCM was observed in the tensile tests.

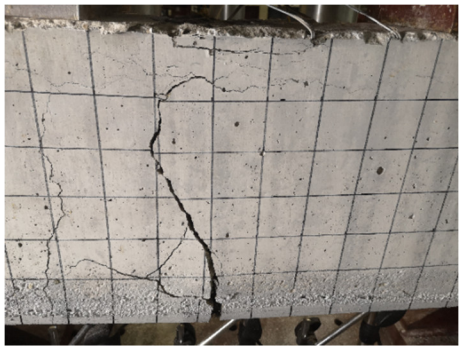

(a) S-B-AP-i125 (FS+CC)

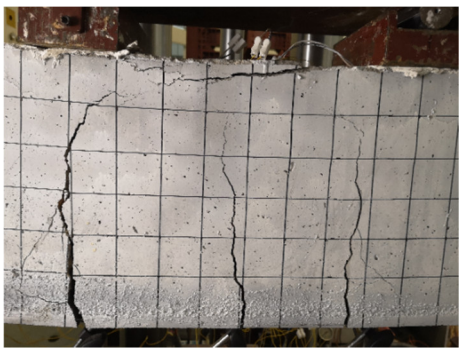

(b) S-B-AP-i375 (FS+CC)

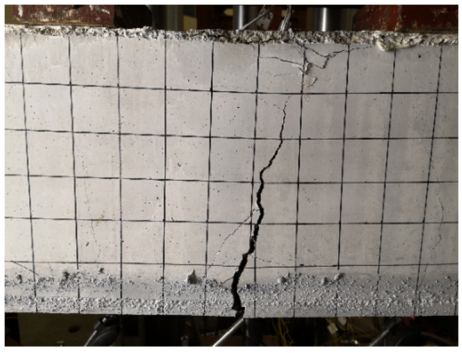

(c) S-B-AP-i500 (FS)

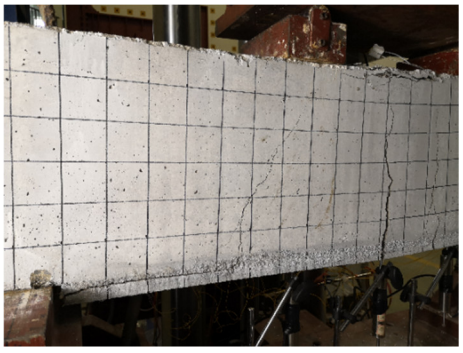

(d) S-B-AP-i750 (FS+D)

Fig. 4.12 Failure modes of beams with externally bonded AP/C-FRCM.

4.5.2 Characterizations of load-deflection curves

The load-deflection curves of beams with externally bonded AP/C-FRCM are indicated in Fig. 4.13(a). The referenced un-strengthened S-B-L0 beam is also included in Fig. 4.13(a) to assess the effectiveness of AP/C-FRCM in strengthening. Besides, for evaluating the influence of anodic polarization on the carbon-FRCM in strengthening, the S-B-L2 beam is compared as well since the AP/C-FRCM composites were the two-layer carbon-FRCM in this chapter. Besides, since one layer

of CF mesh was suffering from anodic polarization in the AC-EC tests, the load-deflection curve of the S-B-L1 beam is added in Fig. 4.13(b)-(d) for a further understanding of the influence of AP/C-FRCM at different current densities on the strengthening behavior of beams.

In Fig. 4.13(a), it was evident that the flexural behavior of beams with externally bonded AP/C-FRCM did not change before the yielding of steel. The load-carrying capacity of the beam at the cracking of concrete and yielding of steel rebars remained unchanged when the beams were strengthened with non-polarized carbon-FRCM and anodically polarized carbon-FRCM. Moreover, the stiffness of the strengthened beams also remained unaltered at the stage of the pre-cracking of concrete and pre-yielding of steel rebars.

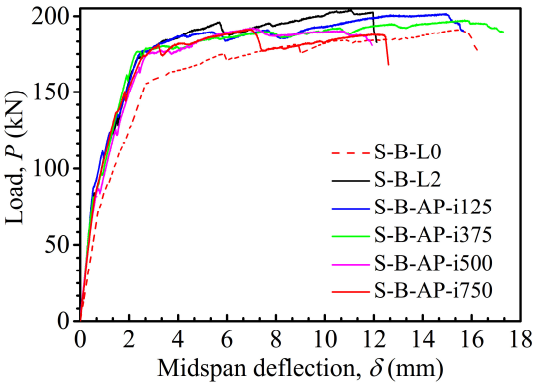

(a) Beams with externally bonded AP/C-FRCM

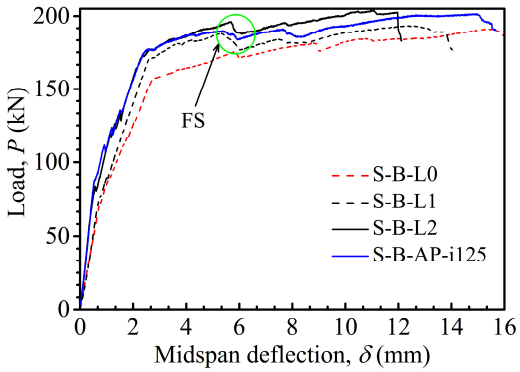

(b) S-B-AP-i125

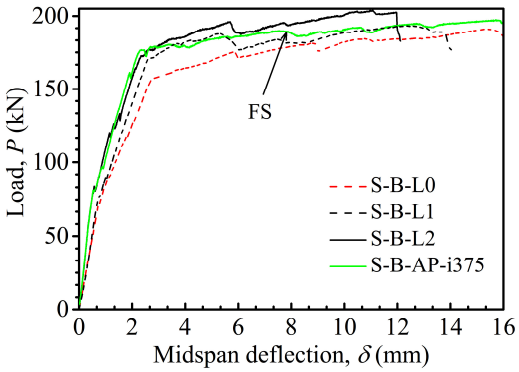

(c) S-B-AP-i375

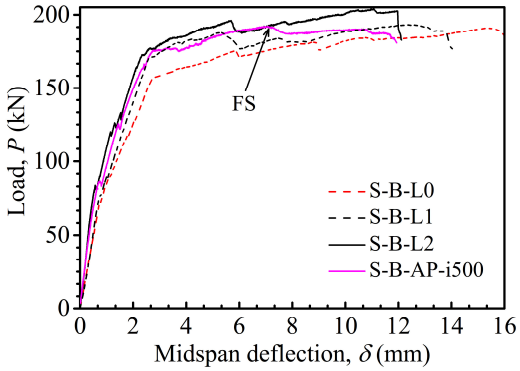

(d) S-B-AP-i500

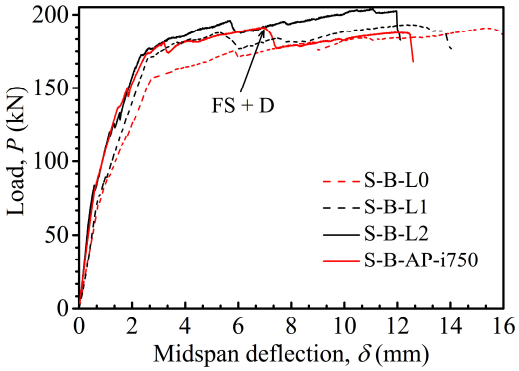

(e) S-B-AP-i750

Fig. 4.13 Influence of anodic polarization on load-deflection curves of RC beams with externally bonded AP/C-FRCM.

However, the flexural behavior of beams changed to some extend at the stage of the post-yielding of steels. The changes were relative to the applied current density on the carbon-FRCM in the AC-EC tests. In Fig. 4.13(b), the stiffness of the S-B-AP-i125 beam at the post-yielding stage was almost identical to the S-B-L2 beam until the FRCM failure due to extensive fabric slippage. The load-carrying capacity of S-B-AP-i125 was 189.75 kN at the failure of AP/C-FRCM that reduced by 3.25% comparing to that of S-B-L2. Then, the load-deflection curve of S-B-AP-i125 behaved between the S-B-L1 and S-B-L2 beam until the load-carrying capacity reached at 201.57 kN at the failure of concrete crushing. In Fig. 4.13(c), the stiffness of the S-B-AP-i375 beam at the post-yielding stage was smaller than that of S-B-L2. It behaved as the S-B-L1 beam that the load-carrying capacity was 189.96 kN at the failure of AP/C-FRCM, and it continued to increase to 197.46 kN at the failure of concrete crushing. The ultimate load-carrying capacity of the S-B-AP-i375 beam was slightly higher than the ultimate load-carrying capacity of the S-B-L1 beam. This is possible mainly due to more residual bond strength between carbon fabric and mortar matrix in the two-layer carbon-FRCM, although one of two layers of CF mesh degraded caused by anodic polarization. The flexural behavior of S-B-AP-i500 was almost identical to the S-B-L1 beam with the ultimate load-carrying capacity of 194.22 kN. Besides, the flexural behavior of the S-B-AP-i750 beam was comparable to the S-B-L0 beam after the failure of fabric slippage and debonding at the matrix-concrete interface plane. The ultimate load-carrying capacity of S-B-AP-i750 was slightly higher than that of the S-B-L0 beam, but the ductility of S-B-AP-i750 reduced.

Table 4.6 summaries the results of all beams (except for S-B-L4) tested in a static loading way. The load-carrying capacity and corresponding deflections at different loading stages are presented in Table 4.6. The gain in the yielding load and ultimate load-carrying capacity against the S-B-L0 beam and the loss in the ultimate load-carrying capacity against the S-B-L2 are calculated and presented in Table 4.6. The gain in the yielding load was more than 10% regardless of the influence of anodic polarization on the carbon-FRCM. However, in Fig. 4.14, it was evident that the ultimate load-carrying capacity of beams with externally bonded AP/C-FRCM decreased as the increase of charge densities. The gain in the ultimate load-carrying capacity of S-B-L2 was 6.73%, and it reduced to 5.45% in the S-B-AP-i125 beam and 3.30% in the S-B-AP-i375 beam. When increasing the charge density, it is a very slight gain in the ultimate load-carrying capacity; even the two-layer carbon-FRCM composite was used. Therefore, it is essential to control the total charge density on the carbon-FRCM composite when it is used as a dual-functional material in the application of the ICCP-SS system.

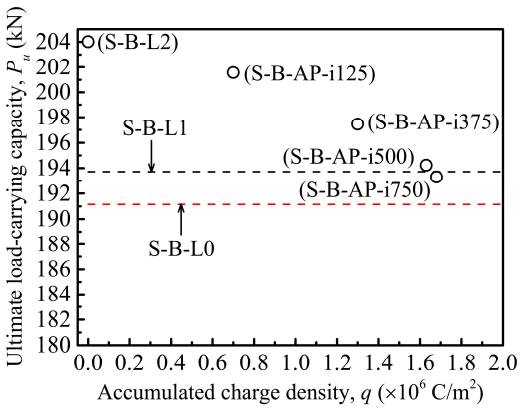

Fig. 4.14 Reduction of ultimate load-carrying capacity of beams with externally bonded AP/C-FRCM.

Table 4.6 Summary of static bending test results of beams with externally bonded M/C-FRCM and AP/C-FRCM.

Beams	P_y (kN)	P_{fs} (kN)	P_u (kN)	δ_y (mm)	δ_{fs} (mm)	δ_u (mm)	Gain in P_y (vs. S-B-L0, %)	Gain in P_u (vs. S-B-L0, %)	Loss in P_u (vs. S-B-L2, %)	FRCM failure mode	Ultimate failure mode
S-B-L0	156.31	/	191.15	2.82	/	15.45	/	/	/	/	CC
S-B-L1	170.19	188.38	193.72	2.62	5.27	12.53	8.88	1.34	/	FS	FS+CC
S-B-L2	172.12	196.12	204.02	2.33	5.69	11.07	10.11	6.73	/	FS	FS+CC
S-B-AP-i125	173.80	189.75	201.57	2.36	5.35	14.95	11.19	5.45	1.20	FS	FS+CC
S-B-AP-i375	175.54	189.96	197.46	2.34	7.56	15.71	12.30	3.30	3.21	FS	FS+CC
S-B-AP-i500	175.64	194.22	194.22	2.99	7.31	7.31	12.37	1.61	4.80	FS	FS
S-B-AP-i750	173.55	193.30	193.30	2.63	6.87	6.87	11.03	1.12	5.25	FS+D	FS+D

Note: P_y and δ_y = load capacity and mid-span deflection at the yielding of steel rebars in tension; P_{fs} and δ_{fs} = load capacity and mid-span deflection at the fabric slippage leading to the sudden drop of the load; P_u and δ_u = load capacity and mid-span deflection at the ultimate state; Gain in P_y = $((P_y)_{str} - (P_y)_{unstr}) / (P_y)_{unstr}$; Gain in P_u (vs. S-B-L0)= $((P_u)_{str} - (P_u)_{unstr}) / (P_u)_{unstr}$; Loss in P_u (vs. S-B-L2)= $((P_u)_{str\_L2} - (P_u)_{str\_AP}) / (P_u)_{str\_L2}$; CC = concrete crush at the compression zone; FS = fabric slippage within mortar matrix; D = FRCM debonding at the matrix-concrete interface.

4.5.3 Comparison between experimental and analytical load-deflection curves

The prediction formulas in flexure for beams with externally bonded carbon-FRCM composites are proposed in chapter 2. The actual apparent tensile stress or strain of CF mesh ($\varepsilon_{ap,f}$) within the mortar matrix is adopted to calculate the contribution of external carbon-FRCM reinforcement to strengthening in flexure. The $\varepsilon_{ap,f}$ is assessed by the regression model based on the global tensile strain of carbon-FRCM specimens (ε_{frcm}). In the plane cross-sectional analysis, the ε_{frcm} is calculated based on the compatibility of strains. The regression model of M/C-FRCM was proposed in chapter 2. Considering the influence of anodic polarization on the mechanical properties of carbon-FRCM that is going to be used as a dual-functional material in the application of the ICCP-SS system, the new regression model of AP/C-FRCM was proposed as Eq. (4.8)-(4.10) in section 4.4.3 of this chapter. The regression model of AP/C-FRCM replaced the model of M/C-FRCM when the apparent strain of AP/C-FRCM was assessed for strengthening beams in flexure.

Fig. 4.15 compares the experimental and analytical load-deflection results for the beams with externally bonded AP/C-FRCM. The results that were obtained according to the prediction formulas in the ACI 549.4R (2013) are also shown in Fig. 4.15. Table 4.7 and Table 4.8 present the experimental and analytical values of both the load-carrying capacity and deflections of the beams with externally bonded AP/C-FRCM. Results show that it is always underestimation for predicting the load-carrying capacity of the beams by using the prediction formulas in the ACI 549.4R (2013). The results based on the proposed prediction formulas fit well with the experimental results. It should be noted that the predictions of the deflection of beams at the yielding of steels are acceptable when the present approach was adopted. Still, it is underestimated for predicting the deflection of beams at the failure of AP/C-FRCM.

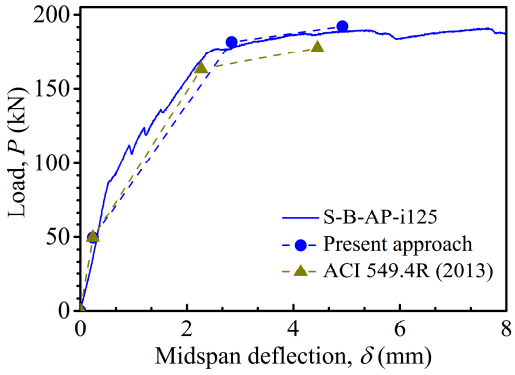

(a) S-B-AP-i125 beam

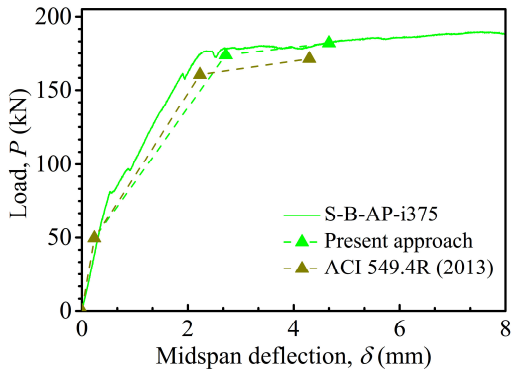

(b) S-B-AP-i375 beam

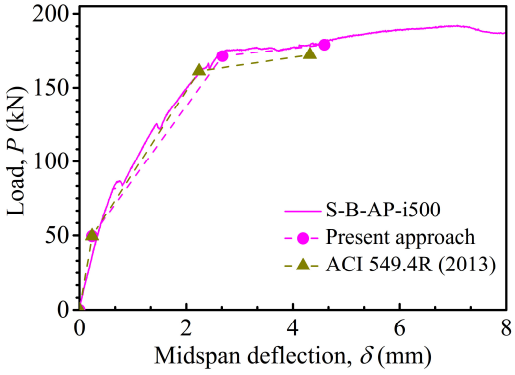

(c) S-B-AP-i500 beam

Fig. 4.15 Comparison of load-deflection relation between experimental and analytical results of beams with externally bonded AP/C-FRCM.

Table 4.7 Comparison of the deflection of beams with externally bonded AP/C-FRCM between experimental and analytical results.

Beam	Deflection at steel yielding (mm)			Deflection at the failure of carbon-FRCM (mm)		
	Experimental	Present approach	ACI 549.4R	Experimental	Present approach	ACI 549.4R
S-B-AP-i125	2.36	2.84	2.27	5.35	4.92	4.45
S-B-AP-i375	2.34	2.72	2.23	7.56	4.67	4.29
S-B-AP-i500	2.99	2.68	2.24	7.31	4.59	4.32

Table 4.8 Comparison of the load-carrying capacity of beams with externally bonded AP/C-FRCM between experimental and analytical results

Beam	Load-carrying capacity of the beam at steel yielding (kN)			Load-carrying capacity of the beam at the failure of carbon-FRCM (kN)		
	Experimental	Present approach	ACI 549.4R	Experimental	Present approach	ACI 549.4R
S-B-AP-i125	173.80	181.60	163.15	189.75	192.13	177.53
S-B-AP-i375	176.54	173.78	160.43	189.96	182.19	171.28
S-B-AP-i500	175.64	171.35	161.18	194.22	179.16	172.21

4.6 Conclusions of this chapter

In this chapter, the accelerated electrochemical (AC-EC) tests were performed on the carbon-FRCM composites. Subsequently, the influence of anodic polarization on the tensile behavior of AP/C-FRCM was evaluated through the static tensile tests. Besides, the influence of anodic polarization on the effectiveness of AP/C-FRCM in strengthening beams was also assessed through the static bending tests. Based on the experimental results and discussion, the following conclusions can be obtained:

(1) According to the results of feeding voltages and electrode potentials in the process of AC-EC tests, it was feasible to adopt the carbon-FRCM as an anode material for preventing steel rebars from corrosion based on the application of ICCP system. The degradation of carbon-FRCM as an anode material in the application of ICCP can be characterized by the acidification that occurred at the interface between carbon fiber bundles and mortar matrix that results in the increasing of feeding voltages.

(2) By considering the principle of the equal cumulative quantity of charge in the ICCP system, the utilization period of carbon-FRCM as an anode material can be evaluated. In the context of the experiments that were performed in this chapter, not only the utilization period of carbon-FRCM as

an anode material can be survived for more than 20 years, but also the effectiveness of carbon-FRCM as reinforcement material in strengthening beams can be maintained. Besides, the utilization period can be extended for a long time by adopting an optimal strategy of the ICCP system.

(3) The reduction of the tensile strength of carbon-FRCM suffering from anodic polarization was detected. The more accumulated charge density in the process of ICCP is, the more reduction of tensile strength is. The influence of charge density on the decrease in tensile strength was found in a linear relationship. Besides, the tensile strain of carbon-FRCM suffering from anodic polarization decreased by around 40% comparing with non-polarized carbon-FRCM.

(4) Based on the experimental data, the model of apparent strain of CF mesh with regarding the global strain of carbon-FRCM composites in tension was modified by considering the influence of anodic polarization. With regarding the tensile strength of dry carbon fiber bundles, the utilization efficiency of fibers in the carbon-FRCM composites decreased as increasing the charge densities in the process of ICCP.

(5) Results of static bending tests of beams with externally bonded AP/C-FRCM indicated that the effectiveness of carbon-FRCM suffering from anodic polarization in strengthening did not change before the yielding of steel and weaken slightly as the charge density increased. The failure modes of beams with externally bonded AP/C-FRCM did not alter that was still the fabric slippage followed by concrete crushing.

(6) The modified model of apparent strain of CF mesh in the AP/C-FRCM was adopted in the proposed prediction formulas to assess the contribution of AP/C-FRCM in strengthening. By comparing the experimental and analytical results of load-deflection behavior of beams with externally bonded AP/C-FRCM, the acceptable agreement was found in predicting the load-carrying capacity at the yielding of steel rebars and extensive fabric slippage failure of AP/C-FRCM.

List of Figures

List of Tables

References

AC434, 2016. Masonry and Concrete Strengthening Using Fabric-reinforced Cementitious Matrix (FRCM) and Steel Reinforced Grout (SRG)Composite Systems. ICC Evaluation Service.

ACI 549.4R, 2013. Guide to design and construction of externally bonded fabric-reinforced cementitious matrix (FRCM) systems for repair and strengthening concrete and masonry structures. American Concrete Institute, U.S.A.

Anwar, M.S., Sujitha, B. and Vedalakshmi, R., 2014. Light-weight cementitious conductive anode for impressed current cathodic protection of steel reinforced concrete application. Construction and Building Materials, 71:167-80.

Bertolini, L., Bolzoni, F., Pedeferri, P., Lazzari, L. and Pastore, T., 1998. Cathodic protection and cathodic preventionin concrete: principles and applications. Journal of Applied Electrochemistry, 28(12):1321-31.

Bertolini, L., Bolzoni, F., Pastore, T. and Pedeferri, P., 2004. Effectiveness of a conductive cementitious mortar anode for cathodic protection of steel in concrete. Cement and Concrete Research, 34(4):681-94.

BS EN 12696, 2016. Cathodic protection of steel in concrete. British Standards Institution.

Byrne, A., Holmes, N. and Norton, B., 2016. State-of-the-art review of cathodic protection for reinforced concrete structures. Magazine of Concrete Research, 68(13):664-77.

Chang, J.J., Yeih, W. and Huang, R., 1999. Degradation of the bond strength between rebar and concrete due to the impressed cathodic current. Journal of Marine Science and Technology, 7(2):89-93.

Christodoulou, C., Glass, G., Webb, J., Austin, S. and Goodier, C., 2010. Assessing the long term benefits of Impressed Current Cathodic Protection. Corrosion Science, 52(8):2671-9.

Cramer, S.D., Bullard, S.J., Covino, B.S., Holcomb, G.R., Russell, J.H., Cryer, C.B. and Laylor, H.M., 2002a. Carbon Paint Anode for Reinforced Concrete Bridges in Coastal Environments. CORROSION 2002, NACE International.

Cramer, S.D., Covino, Jr B.S., Bullard, S.J., Holcomb, G.R., Russell, J.H., Nelson, F.J., Laylor, H.M. and Soltesz, S.M., 2002b. Corrosion prevention and remediation strategies for reinforced concrete coastal bridges. Cement and Concrete Composites, 24(1):101-17.

Donnini, J., y Basalo, F. D. C., Corinaldesi, V., Lancioni, G. and Nanni, A., 2017. Fabric-reinforced cementitious matrix behavior at high-temperature: Experimental and numerical results. Composites Part B: Engineering, 108, 108-121.

Donnini, J., 2019. Durability of glass FRCM systems: Effects of different environments on mechanical properties. Composites Part B: Engineering, 107047.

Glass, G.K., Hassanein, A.M. and Buenfeld, N.R., 2001. Cathodic protection afforded by an intermittent current applied to reinforced concrete. Corrosion Science, 43(6):1111-31.

NACE SP0169, 2007. Standard Practice Control of External Corrosion on Underground or Submerged Metallic Piping Systems. NACE International, Houston, TX, USA.

NACE SP0290, 2007. Impressed Current Cathodic Protection of Reinforcing Steel in Atmospherically Exposed Concrete Structures. NACE International, Houston, TX, USA.

Nobili, A., 2016. Durability assessment of impregnated Glass Fabric Reinforced Cementitious Matrix (GFRCM) composites in the alkaline and saline environments. Construction and Building Materials, 105:465-71.

Pedeferri, P., 1996. Cathodic protection and cathodic prevention. Construction and Building Materials, 10(5):391-402.

Pekmezci, B.Y., Arabaci, E. and Ustundag, C., 2019. Freeze-Thaw Durability of Lime Based FRCM Systems for Strengthening Historical Masonry. Key Engineering Materials, 817:174-181.

Su, M.N., Wei, L.L., Zeng, Z.W., Ueda, T., Xing, F. and Zhu, J.H., 2019. A solution for sea-sand reinforced concrete beams. Construction and Building Materials, 204:586-96.

Su, M.N., Zeng, C., Li, W.Q., Zhu, J.H., Lin, W.H., Ueda, T. and Xing, F., 2020. Flexural performance of corroded continuous RC beams rehabilitated by ICCP-SS. Composite Structures, 232:111556.

Tettamanti, M., 1997. Cathodic prevention and protection of concrete elements at the Sydney Opera House. Materials Performance, 36(9):21-5.

Zhang, E.Q., Tang, L. and Zack, T., 2016. Carbon fiber as anode material for cathodic prevention in cementitious materials. 5th International Conference on the Durability of Concrete Structures, Shenzhen University, Shenzhen, Guangdong, P.R.China. 300-08.

Zhang, E.Q., Tang, L., Bernin, D. and Jansson, H., 2018. Effect of the paste–anode interface under impressed current cathodic protection in concrete structures. Materials and Corrosion, 69(8):1104-16.

CHAPTER 5

FATIGUE PERFORMANCE OF RC BEAMS WITH EXTERNALLY BONDED CARBON-FRCM SUFFERING FROM ANODIC POLARIZATION

5.1 Introduction

The influence of anodic polarization in the process of ICCP on the mechanical behavior of carbon-FRCM was studied in chapter 4. Results showed that the ultimate tensile strength and tensile strain of carbon-FRCM reduced after suffering from the anodic polarization. The degradation model for predicting the apparent strain of CF in the carbon-FRCM suffering anodic polarization was proposed in chapter 4. Furthermore, the flexural behavior of RC beams with externally bonded carbon-FRCM suffering anodic polarization under static loading was also investigated in chapter 4. Results indicated that the negligible influence of anodic polarization on the flexural behavior of FRCM-strengthened beams before the yielding of steel rebars was observed, and only a slight reduction of the load-carrying capacity at the failure of fabric slippage occurred. However, vehicular traffic imposes cycles of loading and unloading on the RC beams strengthened with carbon-FRCM suffering anodic polarization that can lead to fatigue failure. Still, the fatigue characteristics of carbon-FRCM suffering anodic polarization are yet to be understood, although the fatigue performance of non-polarized carbon-FRCM was studied in chapter 3. Moreover, the fatigue life of beams with externally bonded AP/C-FRCM is also yet to be investigated.

In this chapter, firstly, the AC-EC tests of two-layer carbon-FRCM acting as anode material were performed like the description in section 4.2.1 of chapter 4. The tensile tests of anodically polarized carbon-FRCM were then carried out under cyclic loading at different tensile load force levels. The combined effects of anodic polarization and cyclic loading on the fatigue characteristics of carbon-FRCM were analyzed. The endurance limit stress range of AP/C-FRCM was offered by the analysis of S-N curves. Secondly, the four-point bending tests of RC beams with externally bonded AP/C-FRCM was conducted under cyclic loading to investigate the influence of anodic polarization on the fatigue performance of RC beams intervened by the ICCP-SS system. The cyclic tensile tests of AP/C-FRCM and cyclic bending tests of RC beams with externally bonded AP/C-FRCM were the same as presented in section 3.2.1 and section 3.2.2 of chapter 3. Here, the number of specimens involved in this chapter is introduced.

5.2 Experimental program

5.2.1 Cyclic tensile tests program of AP/C-FRCM

Table 5.1 presents the AP/C-FRCM specimens investigated in the cyclic tensile tests. A total of 9 carbon-FRCM specimens were prepared. The labeling of carbon-FRCM specimens was termed starting with C-T (cyclic tensile loading), followed by AP (anodic polarization) and the applied anodic current densities (i.e., i125, i375, and i500) as well as the load force levels (i.e., F40, F50, F60) in the percentage of the relevant ultimate tensile capacity of the control specimens that were tested statically until failure occurred.

Table 5.1 AP/C-FRCM specimens in the cyclic tensile tests.

Carbon-FRCM specimens	Layer of CF mesh	Load force level, L_t (%)	Maximum load force, F_{max_t} (kN)	Minimum load force, F_{min_t} (kN)	Current density, i_a (mA/m^2)
C-T-AP-i125-F40		40	4.51	0.45	
C-T-AP-i125-F50	2	50	5.64	0.56	125
C-T-AP-i125-F60		60	6.77	0.68	
C-T-AP-i375-F40		40	3.02	0.30	
C-T-AP-i375-F50	2	50	3.77	0.38	375
C-T-AP-i375-F60		60	4.52	0.45	
C-T-AP-i500-F40		40	2.39	0.24	
C-T-AP-i500-F50	2	50	2.98	0.30	500
C-T-AP-i500-F60		60	3.58	0.36	

5.2.2 Cyclic bending tests program of RC beams with externally bonded AP/C-FRCM

Table 5.2 presents the beams studied in the cyclic four-point bending tests. A total of 12 beams were prepared. The labeling of beams was termed starting with C-B (cyclic bending loads), followed by AP (anodic polarization) and the applied anodic current densities (i.e., i125, i375, i500, and i750) as well as the applied load levels (i.e., F55, F60, F70) in the percentage of the yielding load capacity of the control beam (i.e., S-B-L0 beam) that were tested statically.

Table 5.2 RC beams with externally bonded AP/C-FRCM in the cyclic bending tests.

Beams	Layer of CF mesh	Applied load level, L_b (%)	Applied minimum limit load, P_{min_b} (kN)	Applied maximum limit load, P_{max_b} (kN)	Current density, i_a (mA/m^2)
C-B-AP-i125-F55		55	31.3	86.0	125
C-B-AP-i125-F60	2	60	31.3	93.8	125
C-B-AP-i125-F70		70	31.3	109.4	125
C-B-AP-i375-F55		55	31.3	86.0	375
C-B-AP-i375-F60	2	60	31.3	93.8	375
C-B-AP-i375-F70		70	31.3	109.4	375
C-B-AP-i500-F55		55	31.3	86.0	500
C-B-AP-i500-F60	2	60	31.3	93.8	500
C-B-AP-i500-F70		70	31.3	109.4	500
C-B-AP-i750-F55		60	31.3	86.0	750
C-B-AP-i750-F60	2	70	31.3	93.8	750
C-B-AP-i750-F70		80	31.3	109.4	750

5.3 Fatigue tensile test results and discussion

The fatigue tensile failure mode of AP/C-FRCM was identical to that of M/C-FRCM, which was the fiber breakage in the primary direction combined with extensive slippage of fibers in the middle of the crack. More details about the description and comparison of failure modes can refer to the section 3.3.1 of chapter 3. Thus, the results of fatigue damage characterizations and fatigue

life performance of AP/C-FRCM are presented and discussed in this chapter.

5.3.1 Fatigue degradation characteristics of AP/C-FRCM

The initial static tensile test of AP/C-FRCM specimens was performed until the first crack occurred before conducting the cyclic loading. The applied tensile load and deformation of AP/C-FRCM specimens were recorded in each pre-determined static loading after a certain number of cycles. Thus, the tensile stress-strain curve of AP/C-FRCM can be obtained. Fig. 5.1 presents the tensile stress versus strain hysteresis curves for AP/C-FRCM at the fatigue force level of 50%. It can be found that the residual strain and the maximum strain increased as increasing cycles. This is attributed to the slippage of fibers that was one of the fatigue mechanisms of carbon-FRCM composites. This phenomenon was also observed in the M/C-FRCM specimens that were described in section 3.3.2 of chapter 3. The difference of the fatigue degradation characterization of AP/C-FRCM was that the area under the uploading-unloading curves increased gradually, and the reduction rate of the stiffness of AP/C-FRCM decreased substantially as increasing the number of cycles. This is possible mainly due to the fiber rupture and decohesion of fibers within the mortar matrix caused by the attack of the acidification in the AC-EC tests (Zhang et al., 2018; Asgharzadeh et al., 2019). Although the fatigue failure mode of AP/C-FRCM was the same as M/C-FRCM, the exposure length of the fabric was longer at the crack in the AP/C-FRCM specimens (see Fig. 5.2). The combined damage effect of the anodic polarization and cyclic loading resulted in the high possibility of fiber rupture and decohesion of fibers with the mortar matrix.

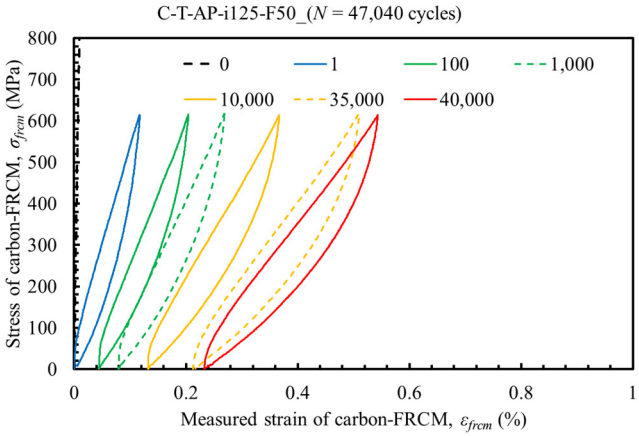

(a) C-T-AP-i125-F50 specimen

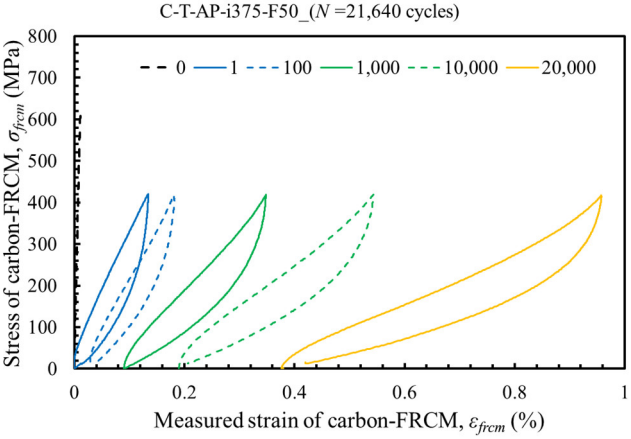

(b) C-T-AP-i375-F50 specimen

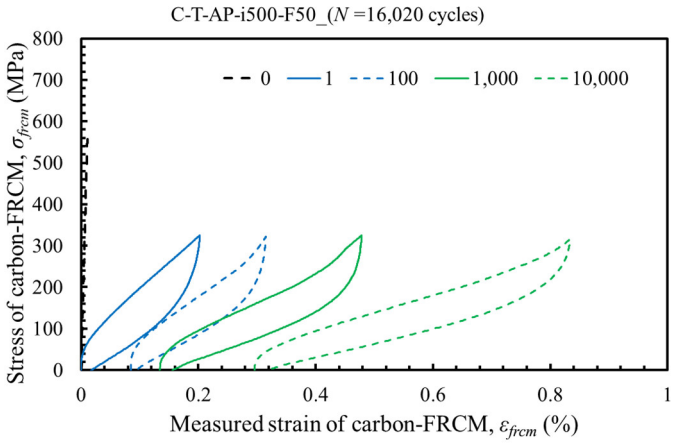

(c) C-T-AP-i500-F50 specimen

Fig. 5.1 Tensile stress versus strain hysteresis curves of AP/C-FRCM specimens at the fatigue force level of 50%.

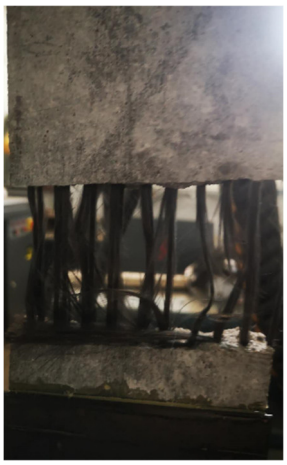

Fig. 5.2 Typical failure mode of AP/C-FRCM under cyclic tensile loading.

The fatigue damage characterization of stiffness of AP/C-FRCM is presented in Fig. 5.3. As a comparison, the results of non-polarized M/C-FRCM specimens are also included in Fig. 5.3. The initial stiffness of AP/C-FRCM at the first cycle was lower than that of M/C-FRCM and decreased as the applied current density increased. The degradation behavior of C-T-AP-i125 specimens was identical to the M/C-FRCM. The stiffness of C-T-AP-i125 specimens decreased to around 0.4 times of the modulus of dry carbon fabric (E_{cf}). Moreover, the stiffness of C-T-AP-i375 and C-T-AP-i500 decreased significantly as increasing the applied current density (i.e., as same as increasing the charge density). The corresponding linear regression of stiffness reduction of AP/C-FRCM at different applied current densities was performed, and the models are presented in Eqs. (5.1) - (5.3). This phenomenon is due to the primary degradation of bond behavior caused by anodic polarization. Thus, the slippage of fibers was the dominant failure in the AP/C-FRCM under cyclic tensile loading. It was verified by the observed fatigue failure mode, as shown in Fig. 5.2.

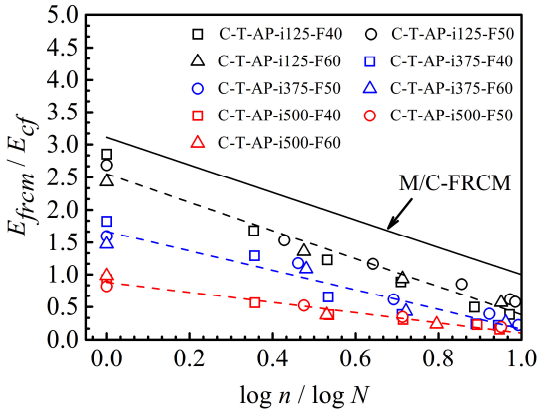

Fig. 5.3 Fatigue degradation characterization of stiffness of AP/C-FRCM.

$$\frac{E_{frcm}}{E_{cf}} = -2.17 \times \frac{\log n}{\log N} + 2.55 \quad \text{.....(5.1)}$$

$$\frac{E_{frcm}}{E_{cf}} = -1.51 \times \frac{\log n}{\log N} + 1.67 \quad \text{.....(5.2)}$$

$$\frac{E_{frcm}}{E_{cf}} = -0.78 \times \frac{\log n}{\log N} + 0.88 \quad \text{.....(5.3)}$$

The stiffness reduction of AP/C-FRCM specimens is based on mathematical relationships between the normalized stiffness (E_{frcm}/E_{cf}) and normalized number of cycles (log n/log N) that follow the format as Eq. (5.4). The quantity of the charge density (q) in the AP/C-FRCM influenced the reduction rate of stiffness and initial stiffness of carbon-FRCM in the first cycle. Therefore, the factor α_q and β_q are adopted to characterize such behavior caused by the charge density. The regression results of these two factors are shown in Eq. (5.5) and (5.6).

$$\frac{E_{frcm}}{E_{cf}} = \alpha_q \times \frac{\log n}{\log N} + \beta_q \quad \text{.....(5.4)}$$

$$\alpha_q = 1.31q - 3.14 \quad \text{.....(5.5)}$$

$$\beta_q = -1.26q + 3.25 \quad \text{.....(5.6)}$$

5.3.2 Fatigue life performance of AP/C-FRCM

Table 5.3 displays the fatigue life results of AP/C-FRCM specimens. As expected, the fatigue life decreased as increasing the applied load force levels. Besides, for the same applied load force level, a slight decrease of fatigue life was found to increase the charge densities in the process of anodic polarization. To understand the characteristic of fatigue life of AP/C-FRCM, the fatigue life performance of non-polarized two-layer carbon-FRCM (i.e., C-T-L2) and the conventional steel are used to perform a comparison.

Table 5.3 Fatigue life results of AP/C-FRCM specimens.

Carbon-FRCM specimens	Current density, i_a (mA/m^2)	Load force level, L_t (%)	Load force ratio, R_t (%)	Number of cycles (× 10^3)
C-T-AP-i125-F40	125	40	10	435.5
C-T-AP-i125-F50	125	50	10	47.0
C-T-AP-i125-F60	125	60	10	16.1
C-T-AP-i375-F40	375	40	10	412.7
C-T-AP-i375-F50	375	50	10	21.6
C-T-AP-i375-F60	375	60	10	14.4
C-T-AP-i500-F40	500	40	10	395.4
C-T-AP-i500-F50	500	50	10	16.0
C-T-AP-i500-F60	500	60	10	5.9

Fig. 5.4 presents the comparison of fatigue life performance among the AP/C-FRCM, non-polarized carbon-FRCM, and steel. As expected, fatigue life increased as the stress range decreased. Based on the mathematical regression, a linear relationship between the stress range and fatigue life in the logarithmical scale can be obtained, as shown in Eqs. (5.7) - (5.9), which the influence of anodic polarization was considered implicitly. The fatigue life performance of AP/C-FRCM was inferior to the non-polarized carbon-FRCM. This is reasonable that the combination of fatigue loading, and anodic polarization accelerated the damage of carbon-FRCM. Regarding the low-cycle scenario, the C-T-AP-i375 and C-T-AP-i500 specimens are inferior to the fatigue life performance of steel. However, the endurance limit stress of AP/C-FRCM is still superior to steel. The endurance limit is defined as the stress range limit for the case of fatigue cycles over two million (ACI 215, 1974). The endurance limit stress range of AP/C-FRCM is extrapolated to be 335 MPa at the current density of 125 mA/m^2, 233 MPa at that of 375 mA/m^2 and 187 MPa at that of 500 mA/m^2 based on the Eqs. (5.7) - (5.9). The endurance limit stress range of steels is 183 MPa according to the fatigue life mode in fib model code (2010). Besides, this value is 138 MPa in the ACI 215 (1974) and 162 MPa in the AASHTO (2017). By such comparison, it is believed that AP/C-FRCM still has an excellent fatigue life performance that can be good composite material in the application of the ICCP-SS system.

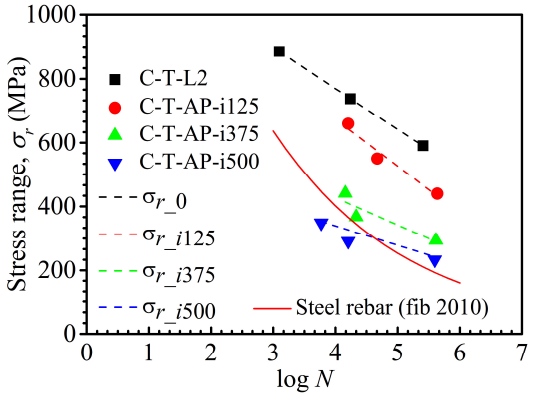

Fig. 5.4 Comparison of fatigue life performance among M/C-FRCM, AP/C-FRCM, and steel rebar.

$$\sigma_{r\_i125} = 1263.9 - 147.5 \log N \quad \text{……..……(5.7)}$$

$$\sigma_{r\_i375} = 765.6 - 84.6 \log N \quad \text{……..(5.8)}$$

$$\sigma_{r\_i500} = 555.0 - 58.4 \log N \quad \text{……..(5.9)}$$

By analyzing the influence of accumulated charge density on the endurance limit stress range, Fig. 5.5 presents the regression results between the accumulated charge density and endurance limit stress range for AP/C-FRCM composites. The prediction model of endurance limit stress range for carbon-FRCM considering the anodic polarization is shown in Eq. (5.10). The correlation coefficient (R^2) is 0.987. The predictive stress range for non-polarized carbon-FRCM is 477 MPa that was close to the value obtained from the fatigue tensile tests of M/C-FRCM (i.e., 490 MPa) in chapter 3. It is believed that Eq. (5.10) is useful for the ICCP-SS system that has a dual-functional carbon-FRCM composite considering the fatigue design application.

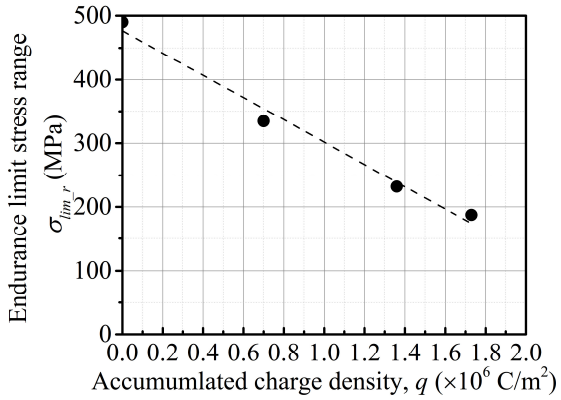

Fig. 5.5 Influence of charge density on endurance limit stress range of AP/C-FRCM.

$$\sigma_{lim\_r} = -175q + 477 \quad \text{……..……..(5.10)}$$

5.4 Fatigue bending test results and discussion

5.4.1 Fatigue degradation characteristics of beams with externally bonded AP/C-FRCM

The load and deflection at the midspan of beams with externally bonded AP/C-FRCM composites were recorded at the static loading after the predetermined number of cycles. The flexural behavior of beams in-service condition was analyzed since the maximum limit load level of 70% did not make steel yielding. All beams with externally bonded AP/C-FRCM failed by the fracture of steel rebars in concrete. Fig. 5.6 shows the load-deflection hysteresis curves for beams with externally bonded AP/C-FRCM at the applied load level of 55%. Other similar curves can be found in Appendix C.1 in this chapter. As expected, the residual plastic deflection was observed at the first cycle due to the cracking of concrete at the bottom of the beam (Papakonstantinou et al., 2002). The cracking of the mortar matrix in the AP/C-FRCM composite was also attributed to the residual deflection of the beam. As increasing the number of cycles, the beam almost followed the

same behavior with no significant reduction of stiffness. Still, the maximum deflection of the beam increased gradually due to the accumulation of residual deflections caused by the cyclic loading. From the results of the beams under static loading, the deflection of the beam was around 2.5 mm at the yielding of steel. The deflection of the beam with externally bonded AP/C-FRCM increased from about 0.5 mm at the first cycles to around 1.5 mm before the fatigue failure when the applied fatigue load levels were lower (i.e., 55% and 60%). Increasing the fatigue load level to 70%, the maximum deflection of the beams got close to be 2.5 mm before the fatigue failure. The measured strain of steels also verified that the steel rebars tended to be yielding before failure at the high fatigue load level.

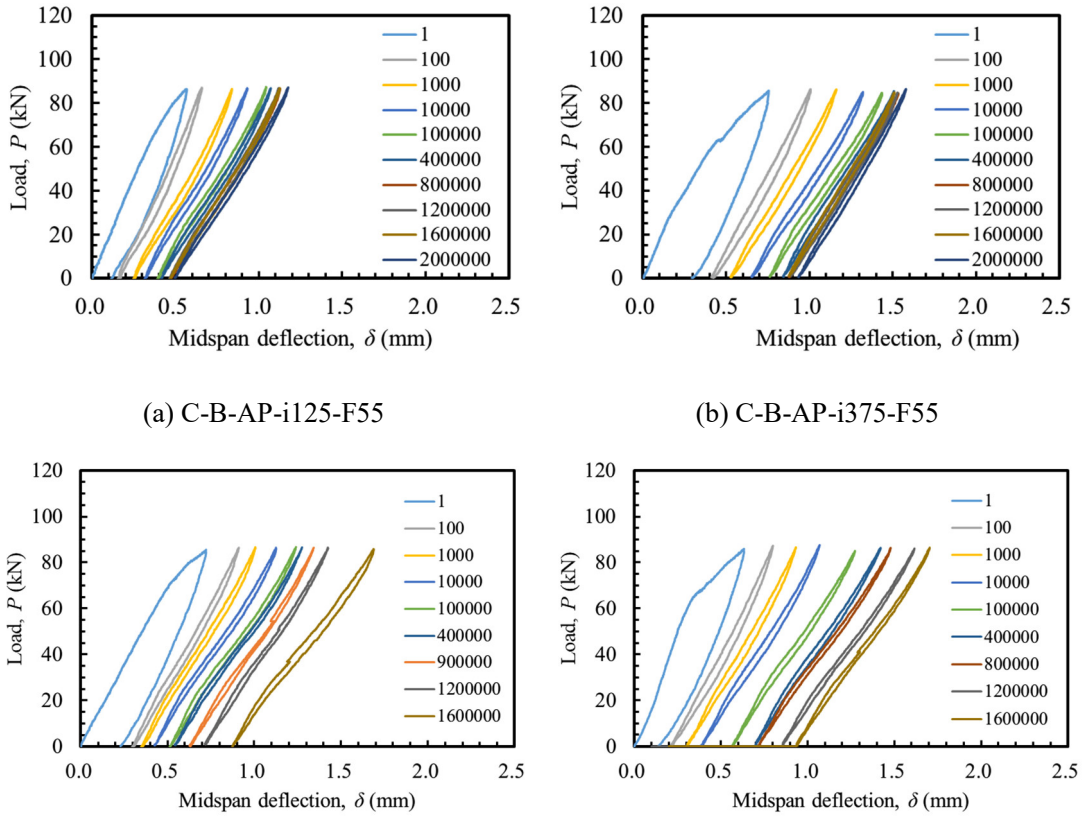

(a) C-B-AP-i125-F55

(b) C-B-AP-i375-F55

(c) C-B-AP-i500-F55

(d) C-B-AP-i750-F55

Fig. 5.6 Load versus deflection hysteresis curves of beams with externally bonded AP/C-FRCM at the applied load level of 55%.

Among the beams with externally bonded AP/C-FRCM, the C-B-AP-i125-F55 and C-B-AP-i375-F55 beams survived over two million cycles. These two specimens were unloaded and tested under static loading to determine their residual strength. The test setup and procedure were the same as that of the statically tested beam specimens. As shown in Fig. 5.7, the residual strength of C-B-AP-i125-F55 and C-B-AP-i375-F55 beams are compared to the S-B-L0 beam and the beam with externally bonded AP/C-FRCM at the same anodic polarization. Compared to the S-B-L0 beam, an increase of load-carrying capacity was also observed in the C-B-AP-i125-F55 and C-B-AP-i375-F55 beams having been subjected to two million cycles. The flexural behavior of those two beams performed nearly identical to their corresponding beams under static loading. This result was also reported by Akbari et al. (2018).

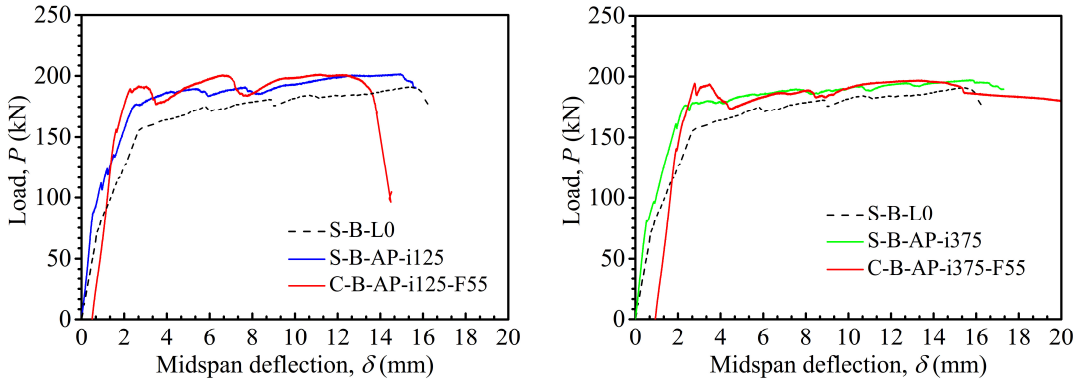

(a) C-B-AP-i125-F55 (b) C-B-AP-i375-F55

Fig. 5.7 Residual capacity of beams survived over two million cycles.

5.4.2 Influence of anodic polarization on the fatigue life of beams

Fig. 5.8 compares the fatigue life performance of beams with externally bonded AP/C-FRCM and non-polarized carbon-FRCM (i.e., C-B-L2 beam) as well as non-strengthened beam (i.e., C-B-L0 beam). Table 5.4 presents the results of the fatigue life of beams with externally bonded AP/C-FRCM, M/C-FRCM, and non-strengthened beams. The results of C-B-L2 beams are compared due to the AP/C-FRCM composites for strengthening beams were also two-layer carbon-FRCM. The fatigue life decreased as increasing the fatigue load levels for all beams. Compared to the C-B-L0 beam, the influence of anodic polarization on increasing fatigue life was impressible at the high fatigue load level. The extension of fatigue life was still significant for the beams with externally bonded AP/C-FRCM. The negative effect of anodic polarization of carbon-FRCM for strengthening was negligible in extending the fatigue life of beams at the fatigue load level of 55%. This is probably due to the contribution of carbon-FRCM in flexure is limited before the yielding of steels, especially in the lower service load scenario. The C-B-AP-i125-F55 and C-B-AP-i375-F55 beams endured two million cycles of load repetition. On the contrary, when the fatigue load level increased to 70% of the yielding load capacity, the fatigue life of beams with externally bonded AP/C-FRCM decreased as increasing the current density or charge density due to the application of ICCP.

Compared to the C-B-L2 beam under cyclic loading, a slight reduction of cycles was observed due to the influence of anodic polarization on the mechanical behavior of carbon-FRCM for strengthening. In Table 5.4, the stress range of steels increased as the charge density increased in the ICCP when the same fatigue load level was applied. For instance, at the fatigue load level of 60%, the stress range of steel was 167.9 MPa in the C-B-L2-F60 beam, it increased to 170.2 MPa in the C-B-AP-i125-F60 beam and up to 182.3 MPa in the C-B-AP-i500-F60 beam. It is believed that the increasing stress range of steel shortens the fatigue life of the beam. It should be noted that no significant rupture of carbon fibers and extensive slippage of fibers in the AP/C-FRCM composites were observed before the fracture of steels. It resulted that steel rebars in concrete are the controlling factor regarding the fatigue failure of the beam. This is also verified by comparing the prediction of fatigue life of AP/C-FRCM. The stress range of AP/C-FRCM composites and the predicted fatigue life of AP/C-FRCM based on the proposed prediction model in section 5.3.2 are presented in Table 5.4. The predicted fatigue life of AP/C-FRCM was always longer than the number of cycles at fatigue failure caused by fracture of steels.

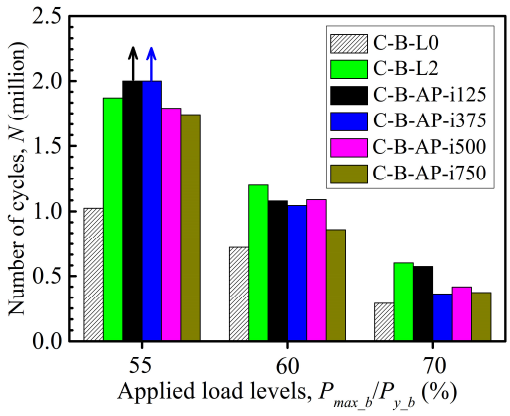

Fig. 5.8 Influence of anodic polarization on fatigue life of beams with externally bonded AP/C-FRCM.

Table 5.4 Fatigue response of beams with externally bonded AP/C-FRCM, M/C-FRCM and non-strengthened beams.

Beam	P_{min_b} (kN)	P_{max_b} (kN)	$\sigma_{s,min}$ (MPa)	$\sigma_{s,max}$ (MPa)	σ_{s_r} (MPa)	Φ_s (%)	$\sigma_{cf,min}$ (MPa)	$\sigma_{cf,max}$ (MPa)	σ_{cf_r} (MPa)	N_{frcm} (million)	N (million)	Φ_n (%)	Φ_{n_i} (%)
C-B-L0-F55	31.3	86.0	98.3	271.2	172.9	/	/	/	/		1.024	/	/
C-B-L0-F60	31.3	93.8	98.3	296.0	197.7	/	/	/	/		0.723	/	/
C-B-L0-F70	31.3	109.4	98.3	345.7	247.4	/	/	/	/		0.290	/	/
C-B-L2-F55	31.3	86.0	58.6	204.1	145.5	15.8	491.4	822.6	331.2		1.870	83	/
C-B-L2-F60	31.3	93.8	58.6	226.5	167.9	15.1	491.4	852.4	361	> 2.000	1.200	66	/
C-B-L2-F70	31.3	109.4	58.6	271.7	213.1	13.9	491.4	905.2	413.8		0.603	208	/
C-B-AP-i125-F55	31.3	86.0	62.6	210.4	147.7	14.6	440.2	746.3	306.1	3.116	2.000	95	/
C-B-AP-i125-F60	31.3	93.8	62.6	232.8	170.2	13.9	440.2	773.2	333	2.047	1.080	49	10
C-B-AP-i125-F70	31.3	109.4	62.6	278.4	215.8	12.8	440.2	821.1	380.9	0.969	0.574	98	5
C-B-AP-i375-F55	31.3	86.0	70.5	227.5	157.0	9.2	342.8	537.0	194.2	5.677	2.000	95	/
C-B-AP-i375-F60	31.3	93.8	70.5	250.7	180.2	8.9	342.8	553.6	210.8	3.613	1.044	44	13
C-B-AP-i375-F70	31.3	109.4	70.5	297.9	227.4	8.1	342.8	583.1	240.3	1.619	0.361	24	40
C-B-AP-i500-F55	31.3	86.0	75.1	233.9	158.8	8.2	286.6	457.0	170.4	3.851	1.790	75	4
C-B-AP-i500-F60	31.3	93.8	75.1	257.4	182.3	7.8	286.6	471.9	185.3	2.140	1.090	51	9
C-B-AP-i500-F70	31.3	109.4	75.1	304.8	229.7	7.2	286.6	498.5	211.9	0.750	0.416	43	31
C-B-AP-i750-F55	31.3	86.0	75.1	233.9	158.8	8.2	286.6	457.0	170.4	3.851	1.742	70	7
C-B-AP-i750-F60	31.3	93.8	75.1	257.4	182.3	7.8	286.6	471.9	185.3	2.140	0.860	19	28
C-B-AP-i750-F70	31.3	109.4	75.1	304.8	229.7	7.2	286.6	498.5	211.9	0.750	0.372	28	38

5.4.3 S-N curves

In this study on the characterizations of RC beams with externally bonded carbon-FRCM, twenty-four beams have been prepared for the fatigue investigation in which three beams were non-strengthened beams, nine beams were externally bonded with M/C-FRCM, and twelve beams were externally bonded with AP/C-FRCM. For predicting the fatigue life of beams with externally bonded carbon-FRCM composites, the fatigue life model was proposed based on the total fatigue test results. Since overall fatigue failure of strengthened and un-strengthened beams was due to fatigue fracture in the reinforcing steel rebars, and either M/C-FRCM or AP/C-FRCM did not suffer from fatigue failure before rupture of steels, the stress range of steels was adopted to characterize the fatigue life performance of beams. Fig. 5.9 shows the S-N curves based on the regression analysis of beam results under cyclic loading. The fatigue life model for beams with externally bonded carbon-FRCM is presented in Eq. (5.11). It is believed that it is useful for the fatigue design application in strengthening concrete structures by carbon-FRCM composites and further consideration in the implementation of the ICCP-SS system.

$$\log N = 7.583 - 0.0086\sigma_r \qquad \text{.....(5.11)}$$

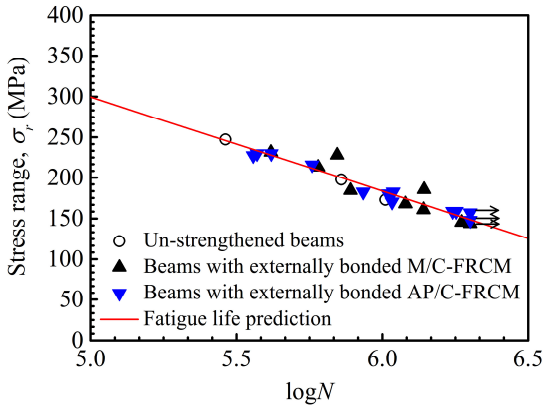

Fig. 5.9 S-N curves of beams with externally bonded carbon-FRCM composites.

5.5 Conclusions of this chapter

In this chapter, the cyclic tensile tests of AP/C-FRCM and cyclic bending tests of beams with externally bonded AP/C-FRCM were conducted. The influence of anodic polarization on the fatigue life performance of carbon-FRCM was discussed. Besides, the fatigue life performance of beams with externally bonded carbon-FRCM suffering from anodic polarization was also compared. The following conclusions can be reached:

(1) The fatigue failure mode of AP/C-FRCM was identical to that of M/C-FRCM, which is a combination of fiber breakage and extensive slippage of fibers. The combined damage effect of the anodic polarization in the process of ICCP and cyclic loading caused an acceleration of the reduction of stiffness and decrease of fatigue life of carbon-FRCM.

(2) The fatigue life model of carbon-FRCM was proposed by considering the influence of

anodic polarization. By the extrapolation of the fatigue life model of AP/C-FRCM, the predicted endurance limit stress range of AP/C-FRCM decreased as the charge densities increased. In the context of the experiments in this chapter, the fatigue life performance of AP/C-FRCM is still superior to the steel rebars.

(3) The enhancement of fatigue life of beams with externally bonded AP/C-FRCM was even detected comparing to the un-strengthened beams. The influence of carbon-FRCM suffering from anodic polarization on the fatigue life performance of strengthened beams was negligible at the lower fatigue load levels, and a slight reduction was observed as increasing the fatigue load levels.

(4) Combined the results of the total twenty-four beams in this study, including three un-strengthened beams, nine beams with externally bonded M/C-RCM, and twelve beams with externally bonded AP/C-FRCM, the S-N curve for beams with externally bonded fabric reinforcement by inorganic matrix was proposed.

APPENDIX C.1. Load versus deflection hysteresis curves of beams with externally bonded AP/C-FRCM

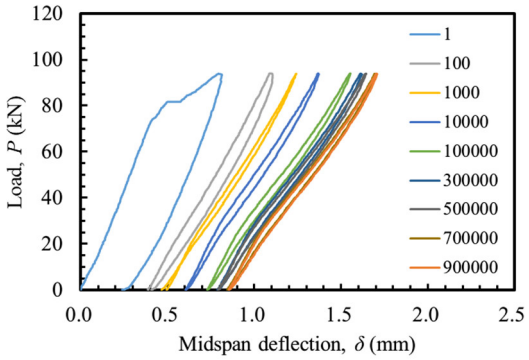

(a) C-B-AP-i125-F60

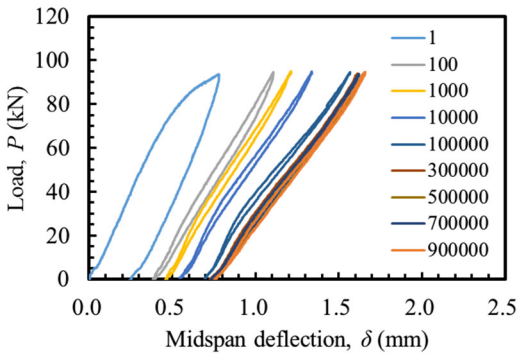

(b) C-B-AP-i375-F60

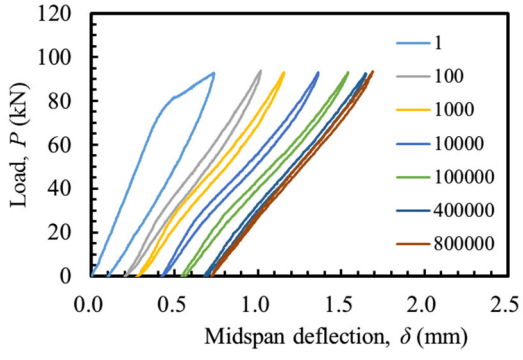

(c) C-B-AP-i500-F60

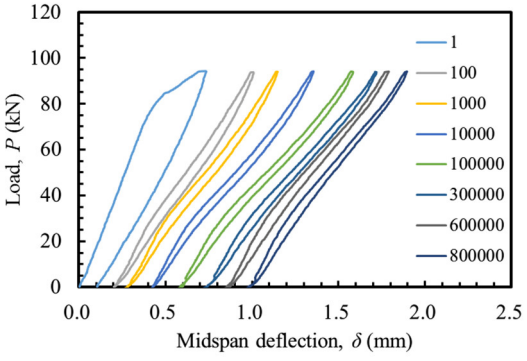

(d) C-B-AP-i750-F60

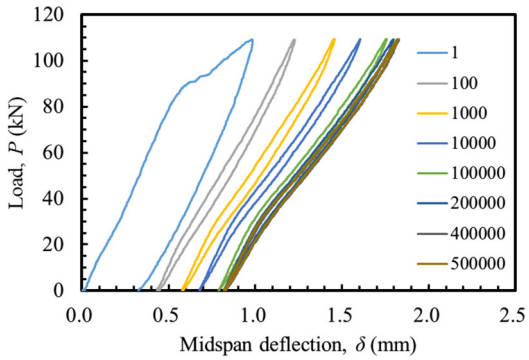

(e) C-B-AP-i125-F70

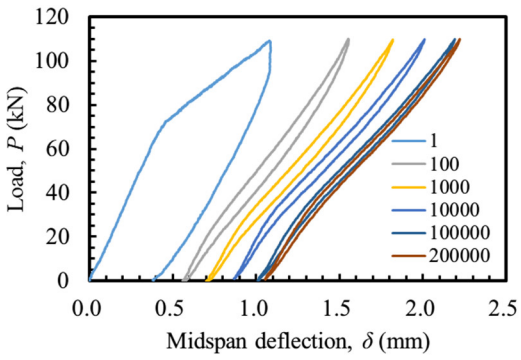

(f) C-B-AP-i375-F70

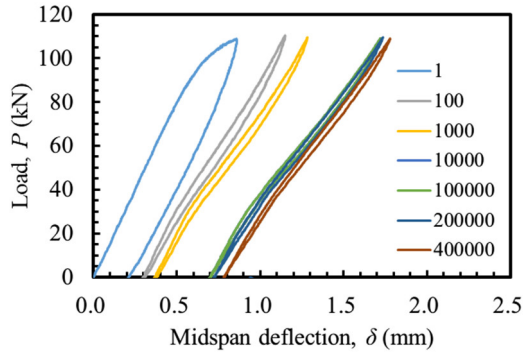

(g) C-B-AP-i500-F70

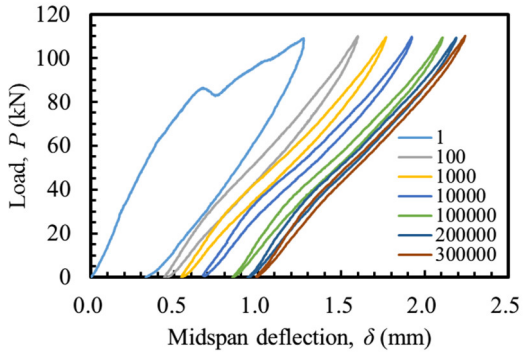

(h) C-B-AP-i750-F70

Fig. C.1.1 Load versus deflection hysteresis curves of beams with externally bonded AP/C-FRCM at the applied load levels of 60% and 70%.

List of Figures

List of Tables

References

AASHTO, 2017. AASHTO LRFD bridge design specifications, 8th edition. Washington (DC), USA. American Association of State Highway and Transportation Officials.

ACI 215R, 1974. Considerations for design of concrete structures subjected to fatigue loading. ACI 215R-74 (reapproved 1997). Farmington Hills, Mich., USA: ACI.

Akbari Hadad, H., Nanni, A., Ebead, U. A.and El Refai, A., 2018. Static and fatigue performance of FRCM-strengthened concrete beams. Journal of Composites for Construction, 22(5), 04018033.

Asgharzadeh, A. and Raupach, M., 2019. Durability behavior of polymer impregnated carbon textiles in alkaline solution as CP anode. Materials and Corrosion, 70(2), 345-356.

CEB-FIP, fib 2010. Fib model code for concrete structures. International Federation for Structural Concrete, Switzerland.

Papakonstantinou, C.G., Balaguru, P.N. and Petrou, M.F., 2002. Analysis of reinforced concrete beams strengthened with composites subjected to fatigue loading. ACI Special Publications, 206, 41-60.

Zhang, E.Q., Tang, L., Bernin, D. and Jansson, H., 2018. Effect of the paste–anode interface under impressed current cathodic protection in concrete structures. Materials and Corrosion. 69(8):1104-16.

CHAPTER 6

CONCLUSIONS AND FUTURE RESEARCH

6.1 Conclusions

The characterizations of RC beams with externally bonded carbon-FRCM were studied under static and cyclic loading in this dissertation. The mechanical behavior of multilayer carbon-FRCM (M/C-FRCM) and anodically polarized carbon-FRCM (AP/C-FRCM) for strengthening beams were considered. The main conclusions of this dissertation are summarized as below:

(1) The constitutive behavior of M/C-FRCM and the mechanical degradation of AP/C-FRCM composites were studied through the static tensile tests. The bi-linear behavior was detected for both M/C-FRCM and AP/C-FRCM composites. With regarding M/C-FRCM, the number of layers of CF mesh has a slight influence on the constitutive behavior of carbon-FRCM. Still, the two-layer carbon-FRCM is an optimized selection in the design of multilayer carbon-FRCM due to the higher tensile strength, Young modulus, and tensile strain. For the carbon-FRCM as an anode material suffering from anodic polarization in the process of ICCP, the tensile strength and strain of AP/C-FRCM reduced as increasing the intensity of anodic polarization that was characterized by the quantity of accumulated charge density. The typical failure mode of all statically tested carbon-FRCM specimens was fabric slippage at the crack of the mortar matrix. To characterize the fabric slippage behavior in the carbon-FRCM, the concept of apparent strain of CF was defined as the true strain of CF mesh within carbon-FRCM specimens in the tensile loading. The apparent strain of CF was represented as a function of the global strain of carbon-FRCM. By using the model of apparent strain of CF, it was revealed that the utilization efficiency of carbon fibers in the M/C-FRCM was around 70% of the tensile strength of dry carbon fabric. The utilization efficiency of carbon fibers in the AP/C-FRCM reduced as increasing the intensity of anodic polarization.

(2) The fatigue characterizations of both M/C-FRCM and AP/C-FRCM were studied through the cyclic tensile tests. The typical failure mode of all cyclically tested carbon-FRCM specimens was fiber breakage combined with extensive slippage of fibers at the crack of the mortar matrix. The fiber breakage and decohesion of fibers within the mortar matrix resulted in the increase of fabric slippage and reduction of stiffness of carbon-FRCM suffering from cyclic loading. Moreover, for the AP/C-FRCM composites, the combined effect of the anodic polarization in the process of ICCP and cyclic loading caused an acceleration of fatigue degradation and a decrease of fatigue life of carbon-FRCM. The fatigue life model and the fatigue strength model of carbon-FRCM were proposed based on the experimental data. The fatigue life performance of carbon-FRCM was superior to that of steels and inferior to that of CFRP composite materials. The endurance limit stress range of M/C-FRCM was up to be 490 MPa, and it reduced as increasing the intensity of anodic polarization. Besides, the fatigue stress limit of M/C-FRCM is recommended to 35% of the ultimate tensile strength. This value is lower than the recommendation of the fatigue stress limit of carbon-FRCM in the ACI 549.4R.

(3) The effectiveness of M/C-FRCM and AP/C-FRCM in strengthening RC beams was

assessed through the static four-point bending tests. The load-carrying capacity of beams with externally bonded M/C-FRCM improved that was largely dependent on the number of layers of CF mesh. The effectiveness of carbon-FRCM suffering from anodic polarization in strengthening did not change before the yielding of steel and weaken slightly as the charge density increased. The fabric slippage failure was typical at a lower amount of CF mesh scenarios, and the failure changed to debonding of FRCM composite and peeling-off of concrete cover at a higher amount of CF mesh scenarios. The utilization efficiency of CF mesh in the M/C-FRCM was around 61% in strengthening beams. Based on the model of apparent strain of CF mesh, the prediction formulas in flexure for RC beams with externally bonded carbon-FRCM was proposed in this study. According to the comparison, analytical results agreed well with the experimental results for load-deflection behavior.

(4) The fatigue performance of RC beams with externally bonded M/C-FRCM and AP/C-FRCM was experimentally examined. Carbon-FRCM composites significantly improve the fatigue performance of RC beams comparing with un-strengthened beams. On the one hand, the more fabric reinforcement ratio is, the more improvement of fatigue life is. On the other hand, the influence of carbon-FRCM suffering from anodic polarization on the fatigue life performance of strengthened beams was negligible at the lower fatigue load levels and slight reduction at increasing the fatigue load levels. The fatigue degradation characteristics of beams with externally bonded either M/C-FRCM and AP/C-FRCM were the increase of deflection and decrease of stiffness at the early fatigue followed by a long period of stable development and finally beams failed at a detectable sudden change of the deflection and stiffness. Overall fatigue failure of un-strengthened beams and beams with externally bonded M/C-FRCM and AP/C-FRCM was due to fatigue fracture in the steel rebars, and the carbon-FRCM composites did not suffer from fatigue failure before fracture of steel. Combined with the results of the total twenty-four beams in this study, the S-N curve for beams with externally bonded fabric reinforcement by inorganic matrix was proposed.

6.2 Considerations for future studies

The following tasks will be taken into consideration in future studies:

(a) In chapter 2, from the static tensile tests of carbon-FRCM, the utilization efficiency of carbon fibers was only around 70% of the tensile strength of dry carbon fabric. From the bending tests of beams with externally bonded carbon-FRCM, the utilization efficiency of CF mesh was only 61% in strengthening beams due to the extensive slippage of fabric. It is necessary to improve the bond behavior between fibers and the mortar matrix. For example, adding some mixtures to improve the impregnation of mortar matrix into fibers, or making treatment on the surface of carbon fabric mesh to improve the bond interphase and anchorage ability of the fabric with mortar matrix.

(b) The tensile tests of dry carbon fabric mesh and tensile tests of carbon-FRCM composites were considered in the proposed prediction formulas in the flexure of beams with externally bonded carbon-FRCM. However, the bond behavior of FRCM-concrete substrate is important to clarify the mechanical behavior of FRCM in strengthening as well

as in fatigue. Therefore, it is useful to study the bond behavior of FRCM experimentally and numerically to improve the design approach in future studies.

(c) In chapter 4, the mechanical degradation of carbon-FRCM suffering from anodic polarization was evaluated at the macro-scale. It is necessary to detect the degradation mechanism of carbon-FRCM at the micro- and mesoscale caused by the anodic polarization in the process of ICCP. The interfacial transition zone (ITZ) between the fibers and mortar matrix is probably to be critical to determine the mechanical degradation of the carbon-FRCM composite. Therefore, to clarify the damage in ITZ will be helpful in understanding the mechanical degradation of carbon-FRCM.

(d) In chapters 3 and 5, the fatigue life performance of carbon-FRCM composites and beams with externally bonded carbon-FRCM were assessed. However, an overall fatigue prediction model should account for both fatigue life and fatigue behavior such as deflection and strain. Therefore, for predicting the fatigue properties of beams with externally bonded carbon-FRCM, the proposal of analytical models will be developed in future studies.